Structural and functional studies of the Apical Sodium Dependent Bile Acid Transporter

Yusuke Sekiguchi

Division of molecular biosciences

Imperial College London

Thesis submitted for the degree of Doctor of Philosophy

2014

Abstract

The apical sodium dependent transporter (ASBT) is responsible for the uptake of bile acids from the apical membrane of the ileum cell. Loss of function mutations of ASBT relate to several diseases, such as Crohn's disease and Primary Bile Acid Malabsorption (PBAM). It is also a target for drugs aimed at lowering cholesterol. The X-ray crystal structure of a bacterial homologue of ASBT, $ASBT_{NM}$, was previously solved at 2.2Å. In order to understand mechanism of ASBT transport in more detail, further structural and functional information are required. In this thesis, a proteoliposome transport assay was performed for various mutations of residues in the sodium and substrate binding sites. $ASBT_{NM}$ has two sodium binding sites and the residues involved in the sites are functionally important. Both E260A and Q77A showed significantly lower transport activities compared to wild type at 40% and 60% respectively. E260 binds to one sodium ion and Q77 the other. The X-ray crystal structures of these two $ASBT_{NM}$ mutants were solved at 2.9 Å and 3.2 Å respectively. These mutant structures revealed that no large scale conformational changes from the wild type were observed though the mutations clearly affected sodium ion binding. These structural and functional data suggest that both two sodium ions are important for the transport activity of $ASBT_{NM}$. However even without sodium ions in the binding sites, the protein can take the same conformation as the wild type structure. The data presented in this thesis, together with a comparison with the results from another bile acid transporter that was recently solved, and a homology model of human ASBT, provide insight into the transport mechanism of ASBT.

Declaration

I declare that the work in this thesis has not been accepted for any previous application for a higher degree, and otherwise stated, carried out by myself. All sources of information within this thesis have been acknowledged.

The copyright of this thesis rests with the author and is made available under a Creative Commons Attribution Non-Commercial No Derivatives licence. Researchers are free to copy, distribute or transmit the thesis on the condition that they attribute it, that they do not use it for commercial purposes and that they do not alter, transform or build upon it. For any reuse or redistribution, researchers must make clear to others the licence terms of this work.

Table of contents

ABSTRACT 2

DECLARATION 3

TABLE OF CONTENTS 4

FIGURE LIST 7

TABLE LIST ERROR! BOOKMARK NOT DEFINED.

ABBREVIATIONS 10

ACKNOWLEDGMENTS 12

CHAPTER 1 INTRODUCTION 13

1.1. Membrane transport mechanism 14

1.2. Secondary Active membrane transport 16

1.3. Alternating access model 17

1.4. Bile acids and the Enterohepatic circulation 22

1.5. Transporters in Enterohepatic circulation 27

1.5.1. Hepatocyte cell 27

1.5.2. Ileum cell 29

1.6. SLC10 family 30

1.7. Aim of this study 32

CHAPTER 2 BIOCHEMICAL AND BIOPHYSICAL METHODS 40

2.1. Membrane protein crystallography 41

2.1.1. Crystallography 42

2.1.2. Crystallization in detergent 44

2.1.2. Lipidic cubic phase method of crystallisation 45

2.2. Isothermal Titration Calorimetry (ITC) 47

2.3. Microscale Thermophoresis (MST) 48

2.4. Circular Dichroism (CD) 49

2.5. Transport assays 50

CHAPTER 3 METHODS 52

3.1. Expression and Purification 53

3.1.1. Mutants preparation 53

3.1.2. Preparation of competent cells 56

3.1.3. Transformation 56

3.1.4. Small scale expression screening of $ASBT_{NM}$ mutants 57

3.1.5. Fluorescence Size Exclusion Chromatography 58

3.1.6. Large Scale Expression and Membrane Preparation 59

3.1.7. Solubilisation and Purification 60

3.2. Biochemical methods 61

3.2.1. Whole Cell Assay (Radio labeled substrate) 61

3.2.2. Proteoliposome transport assay(Radio labelled substrate) 62
3.2.3. Whole Cell Assay (Fluorescence substrate) 65
3.3. Crystallization and structure determination **66**
3.3.1. $ASBT_{NM}$ E260A 66
3.3.1.1. Crystallization 66
3.3.1.2. Data collection and analysis 67
3.3.2. $ASBT_{NM}$ Q77A 68
3.3.2.1. Crystallization 68
3.3.2.2. Data collection and analysis 70
3.3.3. Wild type $ASBT_{NM}$ 71
3.3.3.1 Crystallization 71
3.3.3.2. Data collection and analysis 72
3.3.4. Homology modeling of human ASBT 73
3.4. Biophysical methods **74**
3.4.1. Circular Dichroism (CD) spectroscopy 74
3.4.2. Isothermal Titration Calorimetry (ITC) 76
3.4.3. Microscale Thermophoresis (MST) 78
CHAPTER 4 RESULTS **80**
4.1. Expression and Purification **81**
4.1.1. Expression 81
4.1.2. FSEC 85
4.1.3. Purification 88
4.2. Biochemical methods **89**
4.2.1. Whole cell assay (Radio labelled substrate) 89
4.2.2. Proteoliposome transport assay 90
4.2.3. Whole cell assay (Fluorescence substrate) 96
4.3. Crystallization and structure determination **101**
4.3.1. E260A 102
4.3.1.1. Crystallization 102
4.3.1.2. Data Collection and Analysis 103
4.3.2. Q77A 113
4.3.2.1. Crystallization 113
4.3.2.2. Data Collection and Analysis 115
4.2.3. WT in complex with rhodamine 125
4.2.3.1. Crystallization 125
4.3.3.2. Data Collection and Analysis 126
4.3.4. Homology modeling of human ASBT 129
4.4. Biophysical methods **132**
4.4.1. Circular dichroism (CD) 133
4.4.2. Isothermal Titration Calorimetry (ITC) 137
4.4.3. Microscale Thermophoresis (MST) 141

CHAPTER 5 DISCUSSION **143**

5.1. Relationship between the structures and the function of $ASBT_{NM}$ **144**

5.2. X-ray crystal structure of ASBT from *Yersinia frederiksenii*. **153**

5.3. Human ASBT homology model **165**

CHAPTER 6 SUMMARY **167**

BIBLIOGRAPHY **170**

APPENDIX **182**

Figure list

Figures	Description	Page
Fig. 1.1.	Schematic diagram of alternating access model of secondary active transporter.	17
Fig. 1.2.	**Schematic diagram of LeuT.**	19
Fig. 1.3.	**Schematic illustration of the Mhp1.**	21
Fig. 1.4.	Enterohepatic circulation of bile acids.	23
Fig. 1.5.	Bile acid synthesis from cholesterol, conjugation and dehydroxylation process in human body.	26
Fig. 1.6.	Sequence alinment of $ASBT_{NM}$ to human ASBT and human NTCP.	33
Fig. 1.7.	Schematic diagram of the $ASBT_{NM}$ topology.	35
Fig. 1.8.	Ribbon style representation of $ASBT_{NM}$ structure.	36
Fig. 1.9.	The inward facing pocket of $ASBT_{NM}$ (3ZUY)	37
Fig. 4.1.	Expression screening of $ASBT_{NM}$ WT and mutants	84
Fig. 4.2.	FSEC analysis of $ASBT_{NM}$ WT and mutants.	86
Fig. 4.3.	SDS-PAGE analysis of $ASBT_{NM}$ WT and mutants.	88
Fig. 4.4.	Proteoliposome transport assay results.	92
Fig. 4.5.	$ASBT_{NM}$ hourbouring *E.coli* whole cell and rhodamine assay.	97
Fig. 4.6.	Time course fluorescence based assay of $ASBT_{NM}$ in *E.coli* cells.	99
Fig. 4.7.	Crystal of $ASBT_{NM}$ E260A.	102
Fig. 4.8.	$ASBT_{NM}$ E260A X-ray diffraction image.	104
Fig. 4.9.	$ASBT_{NM}$ E260A X-ray structure and electron densities.	106
Fig. 4.10.	The Na1 binding site of $ASBT_{NM}$ WT X-ray structure and electron densities.	108
Fig. 4.11.	The Na1 binding site of $ASBT_{NM}$ E260A X-ray structure and electron densities.	109
Fig. 4.12.	Fo-Fo maps showing the differences between the WT and E260A structures.	110
Fig. 4.13.	Superposition of WT (3ZUY) and E260A structures.	111
Fig. 4.14.	Crystal of $ASBT_{NM}$ Q77A.	114
Fig. 4.15.	Crystal of $ASBT_{NM}$ Q77A in a loop	115
Fig. 4.16.	$ASBT_{NM}$ Q77A X-ray diffraction image.	116

Fig.	4.17.	Electron density map of $ASBT_{NM}$ Q77A structure.	119
Fig.	4.18.	The Na1 and Na2 binding sites of $ASBT_{NM}$ WT X-ray structure and electron densities.	120
Fig.	4.19.	Superposition of $ASBT_{NM}$ WT (3ZUY) and Q77A structure.	123
Fig.	4.20.	Superposition of WT (3ZUY) and Q77A structures at TM1, TM6 and TM7.	124
Fig.	4.21.	Crystal of $ASBT_{NM}$ WT in the presence of rhodamine.	125
Fig.	4.22.	$ASBT_{NM}$ WT in the presence of rhodamine X-ray diffraction	126
Fig.	4.23.	Overview of $ASBT_{NM}$ WT structure and electron density map.	128
Fig.	4.24.	Superposed structures of human ASBT homology model and $ASBT_{NM}$ at taurocholic acid binding pocket.	130
Fig.	4.25.	Superposed structures of human ASBT homology model and $ASBT_{NM}$ at taurocholic acid binding pocket.	131
Fig.	4.26.	CD spectroscopy result in the far UV region.	135
Fig.	4.27.	Result of ITC dataset of the baseline.	138
Fig.	4.28.	Result of ITC dataset.	139
Fig.	4.29.	Result of MST data	142
Fig.	5.1.	Na1 and Na2 binding sites of $ASBT_{NM}$	146
Fig.	5.2.	Superposed Na2 binding site of $ASBT_{NM}$ to NhaA.	148
Fig.	5.3.	Inward facing pocket in $ASBT_{NM}$ (3ZUY)	151
Fig.	5.4.	The inward facing pocket of $ASBT_{NM}$ (3ZUY) for proteoliposome transport assay	152
Fig.	5.5.	Schematic diagram of the topology $ASBT_{Yf}$.	154
Fig.	5.6.	X-ray crystal structures of $ASBT_{Yf}$.	155
Fig.	5.7.	Sequence alignment of $ASBT_{Yf}$ to $ASBT_{NM}$, human ASBT and human NTCP.	157
Fig.	5.8.	Superposed inward facing conformations of $ASBT_{NM}$ and $ASBT_{Yf}$	159
Fig.	5.9.	Conformational change between inward and outward facing structures of $ASBT_{Yf}$.	161
Fig.	5.10.	Superposed structures of $ASBT_{NM}$ and $ASBT_{Yf}$ at the core domain.	162
Fig.	5.11.	Superposed structures of $ASBT_{NM}$ and $ASBT_{Yf}$ at the taurocholic acid binding site.	164
Fig.	5.12.	Superposed structures of human ASBT homology model and $ASBT_{NM}$.	166

Table list

Tables		Description	Page
Table.	1.1.	SLC10 family	31
Table.	3.1.	Designed primers for mutants	55
Table.	4.1.	$ASBT_{NM}$ mutants	82
Table.	4.2.	Expression screening of $ASBT_{NM}$ WT and mutants	83
Table.	4.3.	Proteoliposome transport assay result result (2^{nd} experiment)	93
Table.	4.4.	$ASBT_{NM}$ E260A data collection and refinement statistics	105
Table.	4.5.	$ASBT_{NM}$ Q77A data collection and refinement statistics	117
Table.	4.6.	$ASBT_{NM}$ WT data collection and refinement statistics	127

Abbreviations

Å	Angstrom
aa	Amino acids
ADP	Adenosine diphosphate
ASBT	Apical sodium dependent transporter
ATP	Adenosine triphosphate
BetP	Sodium glycine betaine symporter
bp	Base pair
BSEP	Bile salt export protein
CC	Correlation coefficient
CCD	Charge coupled device
CD	Circular dichroism
CMC	Clitical micellar concentration
CV	Column volume
Cymal5	5-Cyclohexylpentyl β-D-maltoside
Cymal6	6-Cyclohexylhexyl β-D-maltoside
Da	Dalton
ddH_2O	Deionized destilled H_2O
DDM	n-Dodecyl-β-D-maltopyranoside
DM	n-Decyl-β-D-maltopyranoside
DNA	Deoxy ribonucleic acid
EDTA	Ethylene diamine tetraacetic acid
EHC	Enterohepatic circulation
FSEC	Fluorescence size exclusion chromatography
GFP	Green Fluorecence Protein
GPCR	G-protein coupled receptor
IPTG	Isopropyl β-D-1-thiogalactopyranoside
IR	Infrared laser
ITC	Isothermal titration calorimetry
KD	Dissociation constant
KeV	Kilo electron volt
LB	Lysogeny broth
LCP	Lipidic cubic phase
LDAO	n-Dodecyl-N,N-dimthylamine-N-oxide

LeuT	Leucine transporter
Mhp1	Benzyl hydantoin transporter
MLV	Multilamellar vesicle
MRP2	Multidrug resistance associated protein
MST	Microscale thermophoresis
Mw	Molecular weight
NG	n-Nonyl-β-D-glucopyranoside
Ni-NTA	Nickel nitrilotriacetic acid
NM	n-Nonyl-β-D- maltopyranoside
NTCP	Sodium taurocholate co-transporting peptide
O.D.	Optical density
OATP	Organic anion transporting peptide
OG	n-Octyl-β-D-glucopyranoside
OST	Organic solute transporter
PBAM	Primary bile acid malabsorption
PBS	Phosphate buffered saline
PCR	Polymerase chain reaction
PDB	Protein data bank
PEG	Poly ethylene glycol
PGE2	prostaglandin E2
psi	pound per square inch
RMSD	Root mean square deviation
rpm	Revolutions per minute
SB	Soy bean
SDS PAGE	Sodium dodecyl sulfate polyacrylamide gel electrophoresis
SEC	Size exclusion chromatography
SGLT1	Sodium glucose symporter
SLC	Solute carrier
SPA	Scintillation proximity assay
SUV	Single lamellar vesicle
TB	Terrific broth
TEV	Tabacco etch virus
TLS	Translation libration screw
TM	Trans membrane
UV	Ultra vioret
WT	Wild type
wt/wt	Weight per weight

Acknowledgments

First of all, I would like to express my appreciation to my supervisor Alexander Cameron for his help and allowing me to grow as a research scientist. I would like to express my sincere gratitude to my supervisor David Drew and thank So Iwata for giving me this opportunity as a Ph.D student. In addition, thank you to Nien-jen Hu who taught and supported me. And special thanks to all the members at RCaH, DLS and MPL for their help and support.

For CD experiment, I would like to thank to Giuliano Siligardi and Rohanah Hussain for their help and suggestions. For ITC experiment, I would like to thank to Daivd Staunton for his technical support.

CHAPTER 1

INTRODUCTION

1.1. Membrane transport mechanism

Cell membranes are essential for life as the compartmentalization between the inside and outside of the cell or organelle. They also have important roles that include maintaining the electrical potential, the organization and regulation of enzyme activity and signal transduction. Cell membranes are composed of a lipid bilayer. The polar head group of the lipid faces the surface on both sides of the membrane and the hydrophobic tail points into the interior. Membrane proteins, embedded in cell membranes, constitute one third of human proteins and have a wide range of important roles as cellular machinery systems (Wallin and von Heijne 1998). From the way they interact with the cell membrane, membrane proteins can be classified into several categories, peripheral membrane proteins that associate at the surface of the cell membrane, lipid anchored proteins that bind covalently to the fatty acid or lipids of the cell membrane and integral membrane proteins. Most membrane proteins are categorized as integral proteins that have at least one trans-membrane (TM) segment formed by α-helices (helical bundles) or, less frequently, by β-barrel components.

Cell membranes prevent permeation of various polar molecules, such as ions, sugars, amino acids, nucleotides and drugs. Membrane transporters, forming the second largest family of membrane proteins, are essential for cells as transporting gates between the outside and inside of cells for various materials. Transporters help to maintain homeostasis of ion/solute gradients across cell membranes and regulate signal transfer through calcium ions or neurotransmitters. To move small water-soluble molecules across membranes, cell membranes contain a wide variety of transporters. Each transporter has a specific role by recognizing a particular ion/solute in the kidney, intestine, brain or other cell type. They are categorised into two classes

by the type of source energy for its transport mechanism, passive and active transporter.

The passive transporters that are involved in facilitated diffusion across cell membrane, such as channels and pores, consume only thermal energy as a driving force for their transport. They normally transport solute depending on the direction of the solute concentration from the higher side to the lower side. The transfer of specific ions by channels occurs as an electron-diffusion through a water filled pore, in which remarkably rapid flux as high as 10^8 ions per second. (Alberts 2010) The pores of these channels are usually strictly regulated and allow their substrate to pass through only when they are temporarily opened as a response to the signal from the cell environment including a change in the membrane potential.

1.2. Secondary Active membrane transport

On the contrary, active transporters require other sources of energy to transport their substrate against the electrochemical gradient. Primary transporters use adenosine triphosphate (ATP) or other energy forms, such as light, to drive transport. The Na^+-K^+ pump exports sodium ions and imports potassium ions across the membrane by consuming the energy from the hydrolysis of ATP to adenosine diphosphate (ADP). The Na^+-K^+ pump keeps the sodium ion concentration to be 145 mM outside and 5 to 15 mM inside. The membrane potential is maintained under normal physiological condition. The electric charge in the cell is kept negative against the outside of the cell, in which positively charged ions in the out side of the cell move into the negatively charged cell.

Secondary active transporters use the large electrochemical energy stored in the ion gradient, such as Na^+ or H^+, across the membrane. (Mitchell 1957) For many transporters the electrochemical gradient of Na^+, set up by the Na^+-K^+ pump, combined with the membrane potential drives the transport of a second molecule. Secondary active transporters are categorised into symporters, also called cotransporters, and antiporters that transport a second molecule in the same direction or in the opposite direction, respectively. For example, the sodium glucose symporter (SGLT1) expressed in the small intestine and kidney proximal tubules, transports sodium ion and glucose into the cell with the stoichiometry of two sodium ions and one glucose (Hediger *et al.* 1987; Loo *et al.* 2006).

1.3. Alternating access model

The proposed mechanism of secondary active transporter is called the alternating access model (Jardetzky 1966; Tanford 1982; Forrest *et al.* 2011). According to this model transporters have multiple conformations and transport their substrate with reversible conformational changes. (Fig. 1.1) First, the substrate binding pocket of the transporter is open to one side of the membrane to recognise their substrates. Second, followed by the binding of substrate and co-transported ions in coupled transporters, the transporter closes the pocket to form the occluded state in which the substrates are not accessible to either side of the membrane. Then the transporter releases the captured substrate by opening the pocket to the other side of the membrane.

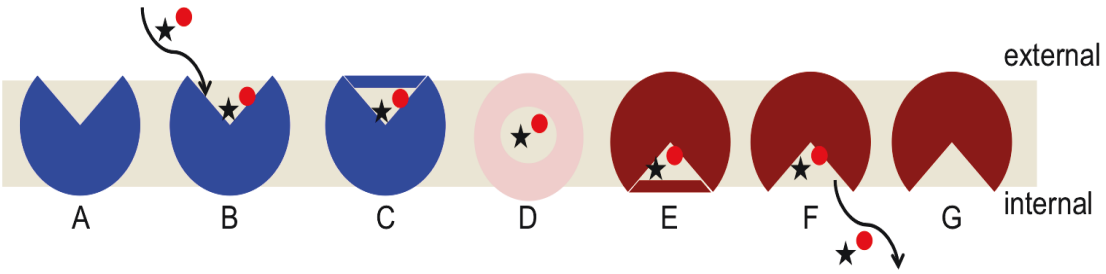


Fig. 1.1. Schematic diagram of alternating access model of secondary active transporter.

Proposed alternating access model. A series of different conformational states during coupled transport. (A) Substrate and ion (black star and red sphere) free outward facing conformation. (B) Substrate and ion bound outward open conformation. (C) Occluded outward facing substrate and ion bound state. (D) Occluded substrate and ion bound intermediate state. (E) Occluded inward facing substrate ion bound state. (F) Substrate and ion bound inward open state. (G) Substrate ion free inward open conformation. Adapted from (Forrest *et al.* 2011)

This transport model has been supported by various X-ray crystal structures of transporters in different conformations. For example the LeuT fold proteins, LeuT (Yamashita *et al.* 2005; Krishnamurthy and Gouaux 2012; Kazmier *et al.* 2014), Mhp1 (Suzuki and Henderson 2006; Weyand *et al.* 2008; Shimamura *et al.* 2010) and BetP (Perez *et al.* 2011; Perez *et al.* 2012; Perez *et al.* 2014). Although these transporters belong to different families and their sequences are not similar each other, they are structurally homologous. The LeuT fold motif is composed of an inverted repeat of two sets of five transmembrane helices. (Fig. 1.2.) The repeated domains are related by a 2-fold symmetry axis. The ion and substrate binding sites are located at the centre of the membrane where two transmembrane helices are unwound.

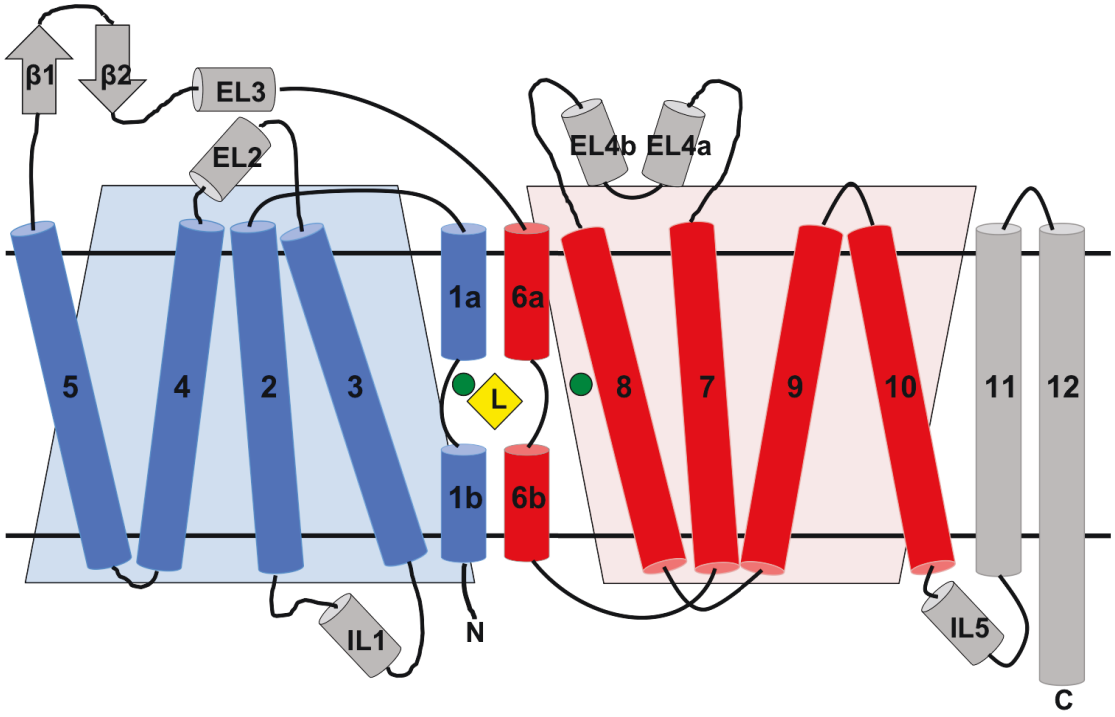


Fig. 1.2. Schematic diagram of LeuT.

Cartoon representation of LeuT oriented with the periplasm on top. The helices are coloured to depict TMs 1 to 12 and grouped by domain. Pink and light blue trapezoids indicate inverted repeat motifs. TM1 to 5 and TM6 to10 are pseudo-symmetry related to each other.

The sodium benzyl hydantoin transporter (Mhp1) from *Microbacterium liquefaciens* is the secondary active transporter belonged to nucleobase cation symport family and transports 5-aryl-substituted hydantoins into the bacterial cells sodium dependently (Suzuki and Henderson 2006; Weyand *et al.* 2008). X-ray crystal structures of Mhp1 were solved with different conformations, the outward facing, the occluded states and the inward facing conformation (Weyand *et al.* 2008; Shimamura *et al.* 2010). These structures, and molecular dynamics simulations, elucidated the transport cycles of Mhp1. Mhp1 is composed of twelve transmembrane helices (TMs) with the N-terminal five TMs and the second five TMs forming inverted motifs. Each domain is related by a pseudo 2-fold axis perpendicular to the middle of the membrane. These TMs are further categorized into three parts, bundle motif (TM1, TM2, TM6 and TM7), flexible helices (TM3, TM5, TM8 and TM10) and hash motif (TM3, TM4, TM8 and TM9) (Fig. 1.3.). The conformational change from the outward facing to inward facing could be explained by the rigid body movement of the hash motif in which relative rotation around the bundle motif could be observed. As the other secondary transporters also has a similar fold, this transporting mechanism would be applied for them as well. However, detailed structural information such as substrate recognition and intermediate conformations are necessary to understand respective transporter's function precisely. Due to the difficulty of X-ray crystallography of experimentally unstable membrane transporter, it is difficult to obtain the structures in different conformation.

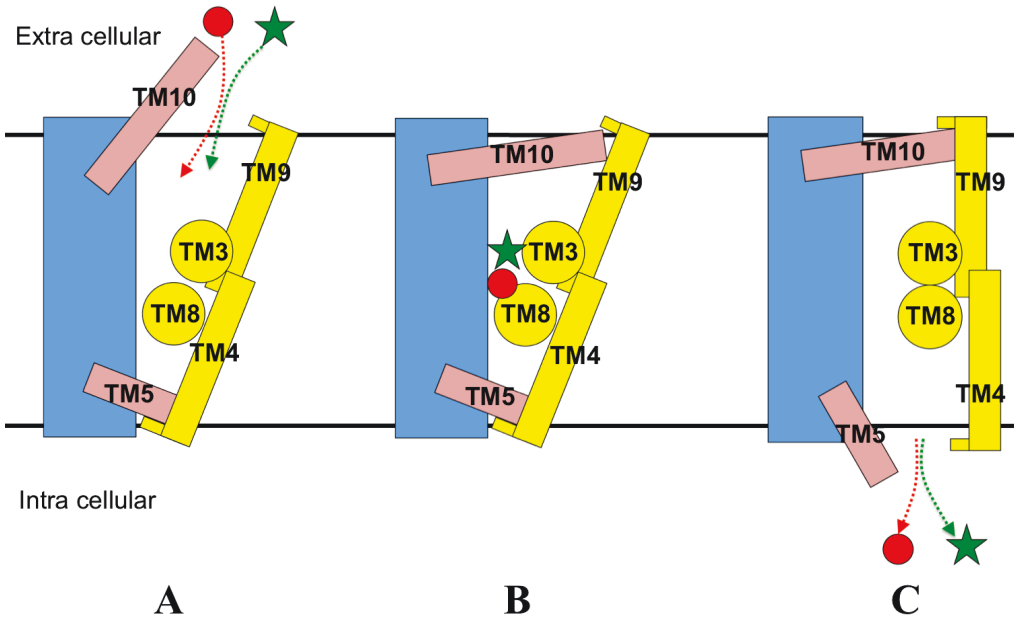


Fig. 1.3. Schematic illustration of the Mhp1.

Cartoon representation of Mhp1 oriented with the periplasm on top. The blue rectangle represents the bundle composed of TM1, TM2, TM6 and TM7. The pink and yellow represent the thin gate and hash motif respectively. Sodium ion and benzyl hydantoin are shown as red sphere and green star. A). Outward facing conformation. B). Occluded conformation. C). Inward facing conformation.

1.4. Bile acids and the Enterohepatic circulation

Bile acids are synthesized from cholesterol in the liver. After they have been synthesised, bile acids are stored in the gallbladder and, after a meal, transferred to the ileum through the duodenum and the jejunum. In the small intestine bile acids help the processing of fat-soluble organic compounds including dietary fat, fat-soluble vitamins (vitamin A, D, E and K) and lipids by emulsifying them and forming micelles (Hofmann 1962). Most of the bile acids secreted into the small intestine are reabsorbed by active transport in the ileum cell and transported back to the liver or gallbladder *via* the portal blood stream. This system, called enterohepatic circulation (EHC), is highly effective and about 95% of bile acids are recycled. (Fig. 1.2) The rest of the bile acids are removed with faeces and replaced by newly synthesised bile acid from cholesterol in the liver. Approximately 500 mg of cholesterol are consumed to produce new bile acids every day in the human body. (Carey 1982).

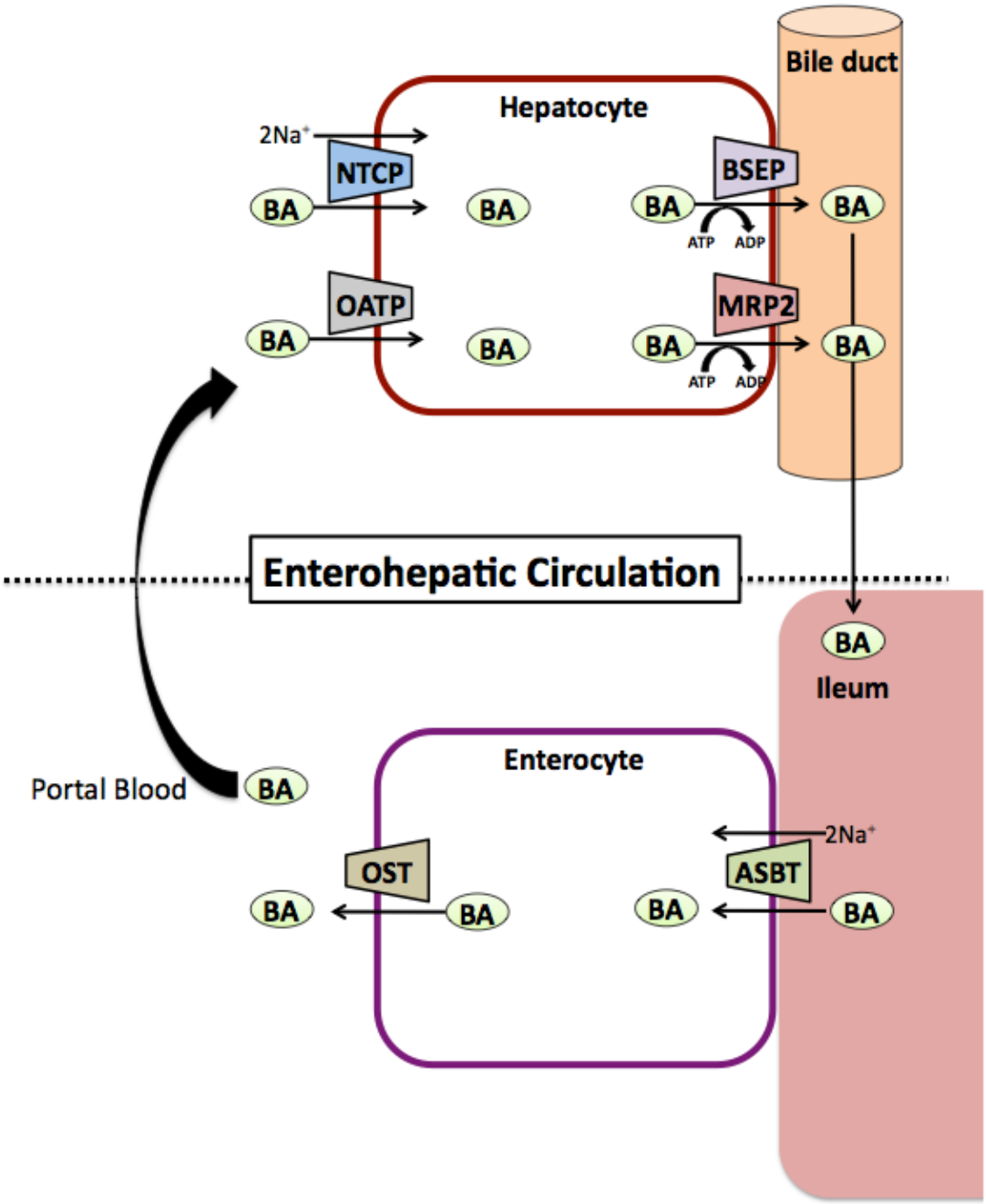


Fig. 1.2. Enterohepatic circulation of bile acids.

Bile acids are synthesized in the liver and exported to bile duct through BSEP and/or MRP2 by consuming ATP as an energy source. Bile acids are secreted into the intestine and reabsorbed in the ileum cell by ASBT in a sodium dependent manner. Reabsorbed bile acids are transported by OST from the ileum to the portal blood then returned to the hepatocyte through NTCP and/or OATP.

Bile acids are amphipathic molecules composed of a hydrophobic steroid structure and hydrophilic carbon side chains terminating in a carboxylic acid. With this amphipathic character, bile acids can work as detergents and form micelles in the intestine to help digestion of insoluble materials. Bile acids are categorised into primary and secondary bile acids. (Fig. 1.3) Cholesterol is converted to primary bile acids through microsomal cytochrome P450 mediated synthesis steps including synthesis of sterol precursors, modifications to the ring structures and oxidation and shortening of the side chain (Jelinek *et al.* 1990; Russell 2003). Various enzymes correspond to these processes as described below. 7α-hydroxylases catalyse hydroxylation of cholesterol at different positions. (Javitt 2000) Then, C_{27} 3β-HSD catalyses the modification of the ring structure (Wikvall 1981; Furster *et al.* 1996; Schwarz *et al.* 2000) followed by side chain oxidation and shortening by sterol 27-hydroxylase (Andersson *et al.* 1989; Dahlback and Holmberg 1990; Pikuleva *et al.* 1998). These primary bile acids include cholic acid and chenodeoxycholic acid. In humans, cholic acid is the primary bile acid constituting about 80% of bile acids. Since cholic acids are poorly soluble at physiological pH in the small intestine, they are usually conjugated with taurine or glycine molecules to give taurocholic acid and glycocholic acid respectively (Falany *et al.* 1994; Solaas *et al.* 2000). These conjugated bile acids are called secondary bile acids. The conjugation reaction is catalysed by the bile acid coenzyme A, amino acid N-acyltransferease enzyme. Additionally, primary bile acids are metabolized into secondary bile acids by the anaerobic bacteria in the gut, where cholic acid and chenodeoxycholic acid are converted to deoxycholic acid and lithocholic acid respectively (Hylemon and Harder 1998). At physiological pH these conjugated states are more soluble than unconjugated states and by preventing passive re-absorption from the small intestine

can maintain enough high concentrations for emulsifying fat or lipids. Furthermore, conjugated states of bile acids are more ionized than unconjugated states at an intestinal pH value, which could emulsify fats more efficiently (Hofmann 1999).

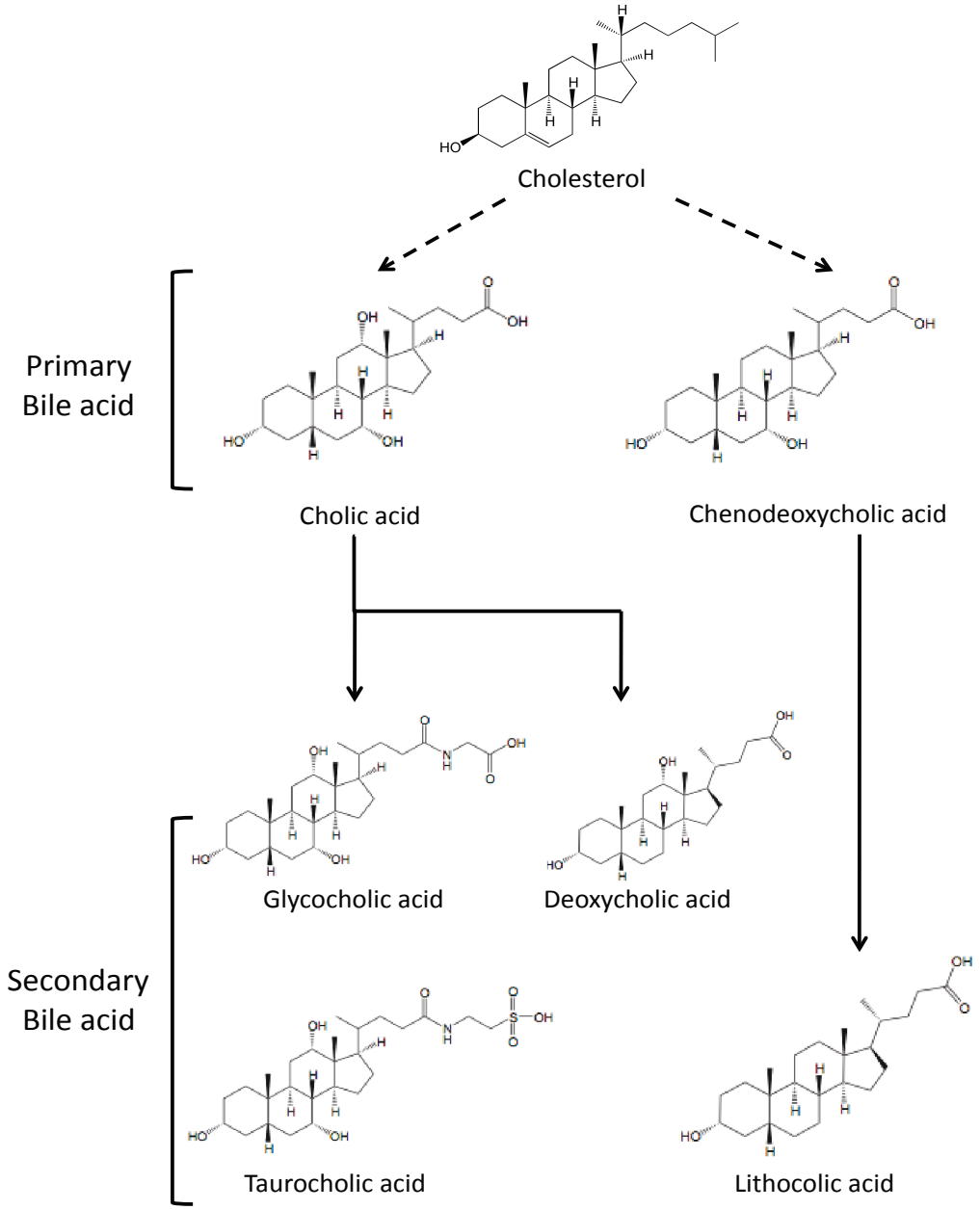


Fig. 1.3. Bile acid synthesis from cholesterol, conjugation and dehydroxylation process in human body.

Cholesterol is converted into cholic acid or chenodeoxycholic acid, primary bile acids, mediated by cytochrome P450 synthesis steps. Cholic acids are catalysed by coenzyme A and conjugated with taurine or glycine to taurocholic acid and glycocholic acid respectively. Cholic acids and chenodeoxycholic acid are metabolized by bacteria in gut to deoxycholic acid and lithocholic acid respectively. Glycocholic acid, deoxycholic acid, taurocholic acid and lithocholic acid are called as secondary bile acid.

1.5. Transporters in Enterohepatic circulation

Many transporters work together to maintain enterohepatic circulation as uptake or efflux gates in the liver hepatocyte cells and/or in the intestine ilium cells (Alrefai and Gill 2007). As conjugated states of bile acids, for example taurocholic acid, are soluble at physiological pH, they cannot pass through cell membranes by diffusion. Thus, membrane transporters are indispensable for bile acid flow between the liver and the small intestine.

1.5.1. Hepatocyte cell

Uptake transporters

Bile acids are transported from the portal blood to the liver by the transporters on the sinusoidal membrane of the hepatocyte (Meier 1995), mainly by OATPs and NTCP (Hagenbuch and Meier 1994; Kullak-Ublick *et al.* 1995).

Sodium Taurocholate Co-transporting Peptide (NTCP: SLC10A1) is expressed in the basolateral membranes of the hepatocytes and allows the sodium dependent uptake of bile acids from the portal blood into the hepatocyte (Shiao *et al.* 2000; Geyer *et al.* 2006). NTCP transports both conjugated and unconjugated bile acids in a sodium symport manner with a stoichiometry of one bile acid and two sodium ions (Schroeder *et al.* 1998).

Organic Anion Transporting Peptide (OATP) also transports bile acids but does not require the sodium gradient as a driving force (Trauner and Boyer 2003). OATPs have several orthologs including OATP1A2, OATP1B1 and OATP1B3 (Tamai *et al.* 2000; Wang *et al.* 2012). OATP1A2 and OATP1B3 are expressed in the brain and liver with better expression in the brain (Kullak-Ublick *et al.* 1995).

OATP1B1 is only expressed in the basolateral membrane of the hepatocytes (Konig *et al.* 2000; Hagenbuch and Meier 2004). OATPs transport amphipathic organic compounds including unconjugated states of bile acids (Meier 1995).

Export transporter

Both recycled and newly synthesised bile acids are exported from the hepatocyte to the bile duct across the canalicular membrane against a steep concentration gradient. MRP2 and BSEP are the major transporters responsible for bile acid uptake across the canalicular membrane (Buchler *et al.* 1996; Gerloff *et al.* 1998). They use the energy involved in the hydrolysis of ATP to transport bile acids with distinct specificities; MRP2 transports divalent bile acids (sulphated taurocholic acid and glycolithocholic acid) and BSEP transports monovalent (taurocholic acid and glycocholic acid).

Multidrug Resistance associated Protein (MRP2) is expressed in the canalicular membrane and has a wide variety of substrate specificity including divalent bile acids such as sulfated taurocholic acid and glycolithocholic acid but does not transport monovalent bile acids; taurocholic acids (Ito *et al.* 2001; Trauner and Boyer 2003).

Bile Salt Export Protein (BSEP) is also expressed in the canalicular membrane and transports conjugated monovalent bile acids, such as taurochenodeoxycholic acids and taurocholic acids (Byrne *et al.* 2002; Noe *et al.* 2002).

1.5.2. Ileum cell

After the secretion from the liver, bile acids function in the intestine to help process fat-soluble compounds. Most bile acids, both conjugated and unconjugated, are reabsorbed in the intestinal lumen and are transported back to the liver via the portal blood. Two membrane transporters are involved as described below.

Apical Sodium Dependent Transporter (ASBT: SLC10A2) is responsible for the uptake of bile acids from the apical membrane of the ileum cell. ASBT requires only the sodium ion gradient and the negative intracellular potential for its function (Weinman *et al.* 1998). Two sodium ions are transported for every bile acid. Both conjugated and unconjugated states of bile acids are transported by ASBT; cholic acid, deoxycholic acid and chenodeoxycholic acid as unconjugated bile acids and taurine and glycine conjugated states of those bile acids (Craddock *et al.* 1998).

Organic Solute Transporter (OSTα-OSTβ) is localized in the basolateral membrane of the ileal enterocyte and transports bile acids into the portal blood independently of the sodium ion gradient. Two different subunits of OSTα and OSTβ are co-expressed and functional as a complex (Dawson *et al.* 2005; Li *et al.* 2007). They transport not only bile acids but also other compounds including estrone-3-sulfate, digoxin and prostaglandin E2 (PGE2) (Ballatori *et al.* 2005). The detailed transport mechanism of OSTα-OSTβ has not yet been revealed.

Although these bile acid transporters have critical roles in the enterohepatic circulation, their precise characters are not yet well studied including substrate recognition and mechanism of transport. Further studies are required to accumulate more information about how the lipids and cholesterol homeostasis are maintained in the human body.

1.6. SLC10 family

Among these transporters, NTCP and ASBT belong to the SLC10 family. The solute carrier (SLC) families comprise 51 families and a total of 378 human transporter genes have been identified (White *et al.* 1997) (Table. 1.1.), including passive transporters, ion-coupled symporters and antiporters. The solute carrier family 10 (SLC10), called sodium/bile salt co-transport family, contains 7 transporters, Na^+/ taurocholate co-transporting polypeptide (NTCP; SLC10A1), apical sodium-dependent bile acid transporter (ASBT; SLC10A2), SLC10A3, SLC10A4 (Geyer *et al.* 2008; Burger *et al.* 2011; Abe *et al.* 2013), SLC10A5 (Fernandes *et al.* 2007), sodium-dependent organic anion transporter (SOAT; SLC10A6) (Geyer *et al.* 2007) and SLC10A7 (Godoy *et al.* 2007). The substrates of only three of these transporters NTCP, ASBT and SOAT are currently known. The other member of SLC10 family are not well characterised. Among these members, NTCP and ASBT play pivotal roles in hepatic and intestinal bile acid uptake respectively as described above (Weinman 1997; Weinman *et al.* 1998). Although, these transporters show high identities to each other from 18% to 60% and possess highly conserved functionally important residues, their substrate specificities vary (Geter *et al.* 2006). Thus, investigations of each transporter are essential to distinguish their detailed transport mechanisms and would help design specific inhibitors.

Table. 1.1. SLC10 family

Human gene name	Protein name	Substrate	Transport coupling ions	Localization
SLC10A1	NTCP	Bile acid	C / Na^+	Liver, Panceas
SLC10A2	ASBT	Bile acid	C / Na^+	Ilium, Kidney, Biliary tract
SLC10A3	P3		O	Ubiquitous
SLC10A4	P4		O	Brain, Placenta, Liver
SLC10A5	P5		O	Liver, Kidney
SLC10A6	SOAT	Sulfate	C / Na^+	Testis, Placenta, Pancreas
SLC10A7	P7		O	Liver, Testis

Adapted from HUGO Nomenclature Committee (White *et al.* 1997). C: Cotransporter; O: Orphan transporter

1.7. Aim of this study

The aim of my research was to determine the X-ray crystal structures of membrane transporters involved in the transport of bile acids to investigate their mechanisms. I wanted to examine the Apical Sodium-dependent Bile acid Transporter (ASBT). As the crystallisation of human membrane proteins is extremely difficult I used a homologue of ASBT to understand the human protein. The structure of this protein was previously solved in our lab (Hu *et al.* 2011). In this thesis I investigate the mechanism further with structures of mutants coupled with characterisation using biochemical and biophysical assays.

ASBT transports bile acids through the apical membrane of the ileum into the portal blood as discussed above. Loss of functional mutation of ASBT has been reported to related to several diseases. Single point mutation from a proline to serine at position 290 resulted in loss of transport activity of taurocholic acid and this substitution was identified in a patient with Crohn's disease (Wong *et al.* 1995). L243P and T262M mutations lead to Primary Bile Acid Malabsorption (PBAM) (Heubi *et al.* 1982; Oelkers *et al.* 1997). It is also a pharmaceutical target for drugs aimed at lowering cholesterol and several ASBT inhibitors have been developed which can significantly lower plasma levels of cholesterol in animal models (Kurata *et al.* 2004; Chen *et al.* 2012; Liu *et al.* 2013). The rationale for this is that if the transporter is blocked with specific inhibitors, the concentration of bile acids returning to the liver decreases. To keep the homeostasis of bile acids concentration in the body, more bile acids are synthesizd from cholesterol resulting in lowering the cholesterol level in the body (West *et al.* 2002; Braun *et al.* 2008).

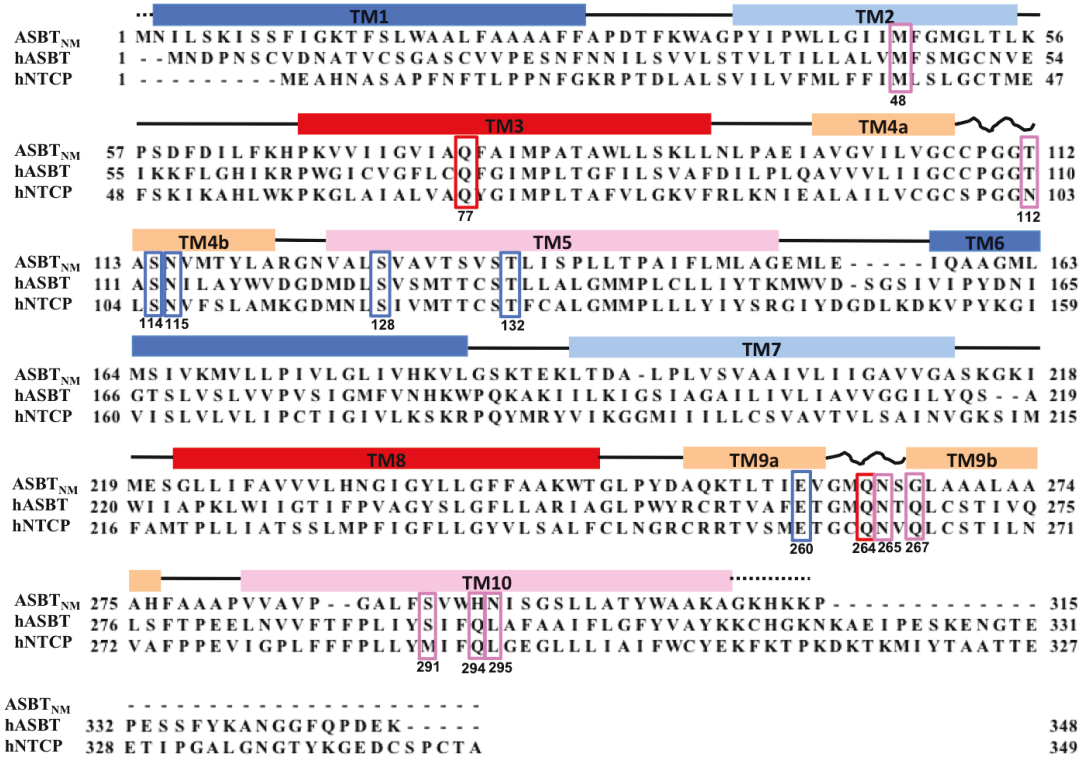


Fig. 1.4. Sequence alignment of $ASBT_{NM}$ to human ASBT and human NTCP.

Sequence alinement of $ASBT_{NM}$ (UniPort ID: Q9K0A9) to the human ASBT (UniPort ID: Q12908) and human NTCP (UniPort ID: Q14973) using ClustalW2 (www.ebi.ac.uk/Tools/msa/clustalw2/) and figure preparation in JalView (Waterhouse *et al.* 2009). The sequence identity of $ASBT_{NM}$ to human ASBT and human NTCP is 26% and 23% respectively as calculated using pairwise alignment in JalView. The coloured bars depict the location of the transmembrane α-helices in $ASBT_{NM}$. Residues forming Na1 and Na2 binding sites are highlighted as blue and red boxes and inward facing open pocket as pink.

The X-ray crystal structure of a bacterial homologue of ASBT was solved in our lab at 2.2Å. (Hu *et al.* 2011) This transporter was from *Neisseria meningitides* and has 26% sequence identity to human ASBT. (Fig. 1.4) Functionally important residues in mammalian ASBT are conserved in this ASBT homologue. Though physiologically the transporter is unlikely to transport bile acids, it may transport a similar molecule. The transport activity of taurocholic acid has been measured and gives a similar Km value to that of human ASBT (Around 50 μM). Thus, this protein is a good model for which to study mammalian bile acid transporters. $ASBT_{NM}$ has ten transmembrane helices and is composed of two inverted structural repeat of five transmembrane helices in a similar fashion to LeuT though there is no structural similarity (Fig. 1.5.) The protein contains two domains, the core and the panel domain made up by intertwining of the repeat motif. The Core domain of six helices has two highly conserved sodium ion binding sites. Taurocholic acid is bound in the inward facing open pocket between core domain and panel domain of four helices. (Fig. 1.6.)

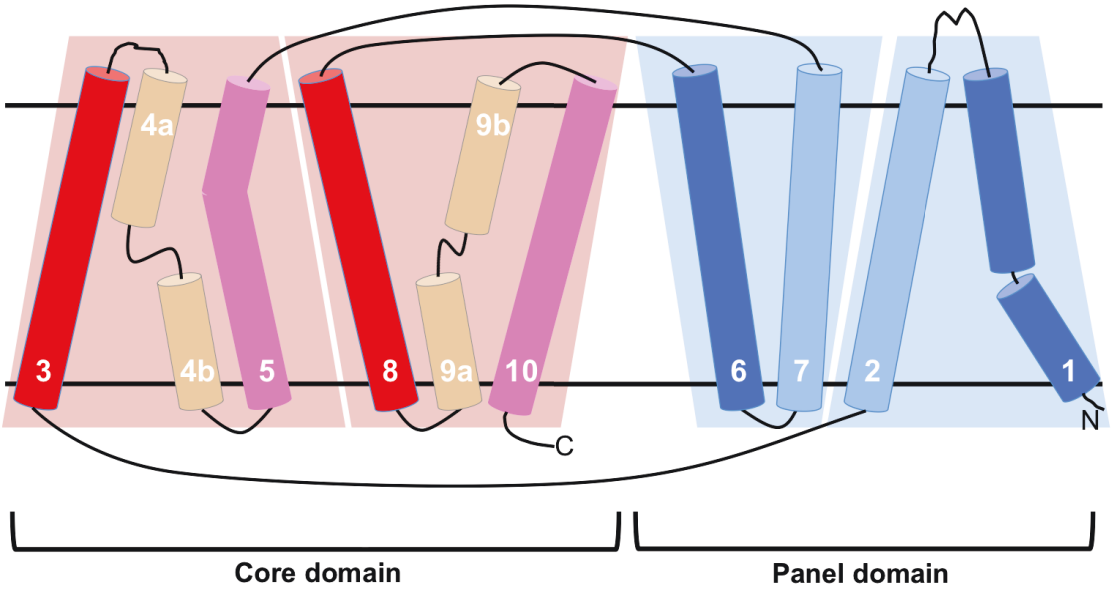


Fig. 1.5. Schematic diagram of the $ASBT_{NM}$ topology.

Cartoon representation of $ASBT_{NM}$ oriented with the periplasm on top. The helices are coloured to depict TMs 1 to 10 (same as Fig. 1.4.) and grouped by domain. Pink and light blue trapezoids indicate inverted repeat motifs, TM1 to 5 and TM6 to10 are psudo-symmetry related each other. Respective pink and light blue motifs form core domain and panel domain.

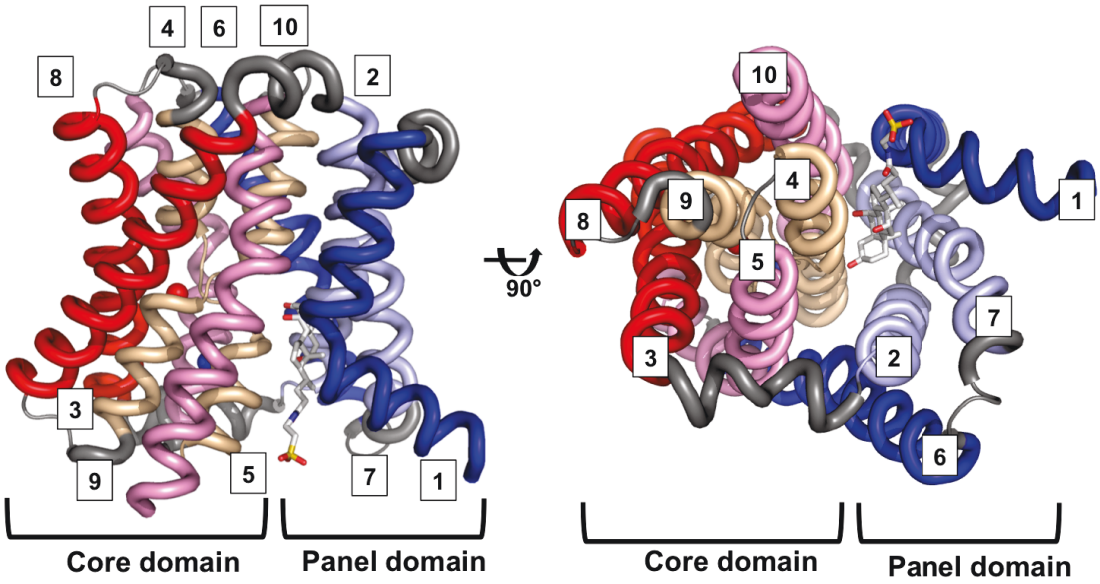


Fig. 1.6. Ribbon style representation of $ASBT_{NM}$ structure.

$ASBT_{NM}$ structure (3ZUY) is represented as ribbon style using PyMOL (Schrödinger, LLC). The colours of helices are the same as Fig. 1.4. and Fig. 1.5. Left: Viewed in the plane of the membrane. TM2 to 6 and TM8 to 10 form the core domain and TM1 to 2 and TM6 to 7 form the panel domain. The red sphere indicates Na2 and blue sphere indicates Na1. Taurocholic acid is represented as a stick model. Right: $ASBT_{NM}$ viewed from the intracellular side.

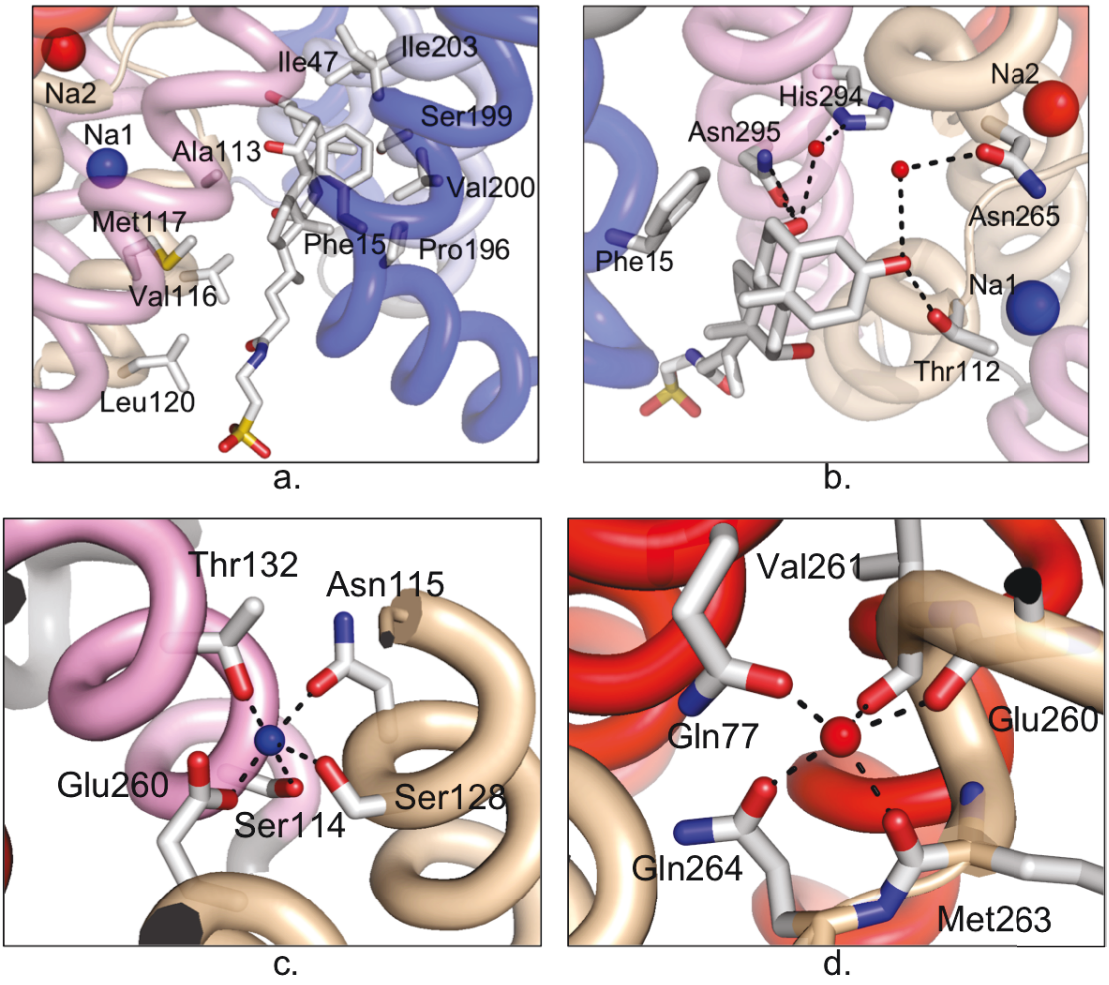


Fig. 1.7. The inward facing pocket of $ASBT_{NM}$ (3ZUY)

a. Inward facing open pocket. The inward facing pocket consists of hydrophobic residues, Phe15, Leu47 Ala113, Val116, Met117, Leu120, Pro196, Ser199, Val200 and Ile203. b. Taurocholic acid binding residues in $ASBT_{NM}$ inward facing open pocket. Thr112 and Asn295 form hydrogen bonding with taurocholic acid. Both Asn265 and His294 interact with taurocholic acid via water molecules. c. Na1 binding site in $ASBT_{NM}$. The side chains of Ser114, Asn115, Ser128, Thr132 and E260 interact with Na1. The backbone of Ser128 interacts with Na1. d. Na2 binding site in $ASBT_{NM}$. The side chains of Gln77 and Gln264 interact with Na2. The backbones of Val261 and Met263 interact with Na2.

From the WT $ASBT_{NM}$ structure in complex with taurocholic acid some key residues were identified as being involved in substrate recognition (taurocholic acid in this structure) and sodium (Na1 and Na2) binding. (Fig. 1.7) T112, N265, H294 and N295 interact with substrate surrounded by hydrophobic residues, F15, I47, A113, M117, L120, P196, S119 and V200. S114, N115, S128, T132 and E260 interact with Na1 and Q77, Q264 and backbone of E260 and M263 interact with Na2. However, the detailed transport mechanism is not clear yet. According to the alternating access model, $ASBT_{NM}$ would change the conformation from outward to inward facing conformation by the rigid body movement of the panel domain and the core domain. In this structure, $ASBT_{NM}$ would represent the intermediate state of just before releasing the substrate and/or sodium ion. This structure was obtained under the crystallization condition that is not the same as cell environment including excess amount of taurocholic acid and the lack of the sodium gradient and the membrane potential. There was no structure of an outward facing conformation and the recognition of the substrate or the roles of the two sodium ions in the transport pathway were not evident. There are a number of ways that this can be investigated. One way is through site-directed mutagenesis approaches, preferably combining this with crystallography. Another way is to determine the structure in complex with other compounds that may bind to $ASBT_{NM}$ and trap the protein in different conformations. As sodium ions could hold $ASBT_{NM}$ in a particular conformation, removing sodium ions from $ASBT_{NM}$ could change the conformation of the protein. However, removing sodium ions from the system is practically difficult as they are included in the cell culture media and purification buffers to keep $ASBT_{NM}$ stable. Instead of removing sodium ions from the system, mutation of sodium binding residues is introduced to exclude functionally important ions. A similar approach was used for LeuT. The

structure of LeuT, a bacterial homolog of the neurotransmitter sodium symporters (NSSs), has been solved in different conformations, outward and inward facing (Kazmier *et al.* 2014). Firstly, outward facing occluded conformation was solved in complex with its substrate and two sodium ions (Yamashita *et al.* 2005). Secondly, outward facing open conformation was solved in complex with the competitive inhibitor and two sodium ions. Lastly, inward facing open conformation was solved in which sodium binding residues were mutated (Krishnamurthy and Gouaux 2012). Thus, the mutagenesis approaches targeting sodium ion binding site would be an appropriate strategy to obtain the different conformation of the secondary active transporters.

CHAPTER 2

Biochemical and Biophysical methods

2.1. Membrane protein crystallography

In order to express membrane proteins abundantly, it is necessary to examine a large variety of conditions including homologues of the protein in different species, constructs of amino acids sequence and suitable detergents. The GFP-fusion system (Drew *et al.* 2006; Kawate and Gouaux 2006) enables many constructs to be screened within quite a short time. The method works by adding green fluorescence protein (GFP), to the C-terminus of the target membrane protein construct. Then, if the membrane protein expresses and is correctly introduced into the cellular membrane, GFP will also be expressed. As the amount of GFP expressed can be determined by measuring the fluorescence counts this provides a direct readout of the amount of target protein. The expression level of the membrane protein can be estimated by counting the fluorescence level of GFP from cell culture solution without harvesting or solubilising the cells. Furthermore, this fluorescence can be used to analyze the monodispersity and stability of the target membrane proteins in complex with a series of detergents using size exclusion chromatography, named Fluorescence Size Exclusion Chromatography (FSEC). Traditional experimental methods usually need a lot of time and effort to screen expression levels and detergent selection compared to this rapid and efficient method. Consequently, this is a successful method (Jasti *et al.* 2007; Kawate *et al.* 2009; Shaffer *et al.* 2009; Sobolevsky *et al.* 2009; Tao *et al.* 2009; Feng *et al.* 2010; Tang *et al.* 2010). Although some difficulties have been overcome with developments of techniques like this GFP-fusion system, structural determination of membrane proteins is still difficult and we need to make more effort and dedication to solve them.

2.1.1. Crystallography

X-ray crystallography gives the most detailed information about the protein structure at the resolution of individual atoms. The protein molecule is composed of a chain of amino acids residues in which length of bonded atoms are less than around 1.5 Å. Whereas this range of length is too short for the visible light, wavelengths of 400 – 700 nm, to observe the object, X-rays are capable to be diffracted from the individual atoms, 1 pm – 10 nm. When X-rays pass through the protein, X-rays diffracted as a result of the interaction with the electrons of the atoms. Since the signal from a single molecule is too weak to be detected, protein crystals are required that contains many ordered molecules where each signal from one protein is reinforced by the signal from the others. The X-ray diffraction pattern from the crystal can be recorded on a detector as discrete reflections. The atomic information of the protein is related to the diffraction pattern in a mathematical manner termed the Fourier transform. As X-rays cannot be focussed sufficiently to recombine the diffracted X-rays, to obtain the atomic structure an inverse Fourier transform is performed by computer using the directions and intensities of diffracted X-rays.

The X-ray crystal structure gives powerful information with its precise descriptions of the protein structure at an atomic level. In spite of its importance for living cells, structural information of membrane proteins is limited with less than 495 unique membrane proteins submitted among over 102,720 proteins in the Protein Data Bank at Aug2014. (http://www.rcsb.org/, http://blanco.biomol.uci.edu/mpstruc/) The reason for the low amount of structures solved is due to the extreme difficulty in handling the protein experimentally. Since membrane proteins are surrounded by hydrophobic tails of phospholipids in the membrane, the surface of their transmembrane domains are also composed of hydrophobic residues and so the

proteins are poorly soluble and unstable in water when removed from the membrane. This insoluble character makes it difficult for the experimental procedures of X-ray crystallography, purification and crystallization. To solve this problem the membrane proteins are usually solubilized with detergents. The hydrophobic tails of the detergent surround the protein so that it is stabilized and can be treated as a general soluble protein during the purification and crystallization steps by keeping the required concentration of detergents. However, selecting the ideal detergent for a target protein from various kinds of detergents often requires researchers to spend a lot of time and energy. For these reasons, membrane proteins are still regarded as some of the most difficult targets in the field of X-ray crystallography.

2.1.2. Crystallization in detergent

Membrane proteins composed of large hydrophobic surface require detergent molecule to be stabilized in solution. However, these detergent molecules and their formation of micelles occupy a large amount of the surface region of the membrane protein preventing sufficient protein-protein contacts for forming protein crystals. Furthermore, the choice of the detergents used for the crystallization is important. DDM is the most popular detergent for solubilization, purification and even crystallization. Although crystallization with DDM often gives membrane protein crystals, the crystals obtained generally do not diffract well due to its large micelle size (Sonoda *et al.* 2011). Use of detergents with a smaller micelle size than DDM can give better diffracting crystals (Sonoda *et al.* 2011). For example, LDAO was used for solving the $ASBT_{NM}$ structure at the resolution of 2.2 Å. In spite of the benefit from small detergents, they are too harsh for many membrane proteins and destabilize them. Thus, the membrane protein should be stable enough so that crystal can be obtained under the harsh small detergent.

The most popular technique for crystallization is the vapour diffusion method, in which two variations are usually used, sitting drop and hanging drop. The small amount of concentrated protein is aliquot to the glass or plastic well and mixed with reservoir solution to a final ratio of 1:1. Then crystallization drop is sealed in a closed well which contains an excess amount of the reservoir solution and incubated at 4 °C or 20 °C. The concentration of the precipitant solution in the crystallization drop is about half of the original condition. In the closed system, the crystallization drop starts evaporating by the solute concentration gradient against the reservoir. During the evaporation, concentrations of the protein increase leading to the formation of the protein crystal nuclei if the condition is ideal for the protein.

2.1.2. Lipidic cubic phase method of crystallisation

The lipidic cubic phase crystallization is a unique method for membrane protein that has been developed relatively recently compared to the vapour diffusion method (Cheng *et al.* 1998; Cherezov *et al.* 2002; Caffrey and Cherezov 2009; Aherne *et al.* 2012). Examples of successful crystallisation have been reported from various membrane proteins such as β-barrel membrane proteins (Cherezov *et al.* 2006; Cherezov *et al.* 2008), α-helical membrane proteins (Schobert *et al.* 2002; Cherezov *et al.* 2006; Gmelin *et al.* 2007; Wohri *et al.* 2009; Tiefenbrunn *et al.* 2011) and, especially GPCRs (Granier *et al.* 2012; Kruse *et al.* 2012; Liu *et al.* 2012; Manglik *et al.* 2012; Wu *et al.* 2012; Zhang *et al.* 2012; Hollenstein *et al.* 2013; Tan *et al.* 2013; Wang *et al.* 2013; Dore *et al.* 2014). At a distinct temperature and lipid to water ratio, the lipid forms a cubic phase that is composed of a lipid bilayer. Monoolein is the most popular lipid for LCP and well studied so far. The cubic mesophase is formed at 20 °C at a water monoolein composition of around 40% (wt/wt) water. When purified membrane proteins are mixed with this LCP, they reconstitute into a curved lipid bilayer forming a viscous and sticky LCP. This could eliminate detergent molecules and micelle from around the membrane protein. The mixture of LCP and membrane protein is then dispensed onto the glass plate and the crystallization precipitant is added onto the LCP and sandwiched by a thin glass cover. Components of the precipitants could diffuse into the LCP by passing through water pores, destabilize the cubic phase and lead to phase transitions and separations, which could cause nucleation of a protein crystal and further crystal growthing. Owing to the tight packing, the diffraction data is also of higher quality. Although the LCP method is a powerful technique for membrane protein crystallization, some difficulties still exist as described below.

Size of crystal

Except for some examples, LCP crystals are generally tiny around 1 to 50 μm size. Together with the viscous and half transparent character of LCP, this size of crystal is difficult to observe under the microscope without a cross polarizer lens. Because of the small size of crystals microfocus beamlines are essential to collect data, otherwise normal beam size is too big to shoot tiny crystal. Additionally, small crystals do not survive long enough to collect a full data set using a high energy synchrotron beam. Thus, multiple data sets from LCP crystals must be merged to give a complete data set. It is also necessary to perform grid scanning diffraction image collection, to find out where the LCP crystal is located in the non-transparent LCP droplet on the loop. Grids of 10 to 300 images are used to cover the loop. To achieve these purposes fast speed image reading detector is desirable, for example the PILATUS (Broennimann *et al.* 2006) detector is useful for collecting data quickly.

Fishing the crystal

The LCP crystallization plate is a sandwich glass plate composed of a base glass and a cover glass. When fishing the crystal from the well, the cover glass has to be cut by manually using glass cuter. Experience is required to open the cover glass without damaging the crystal. It is also often observed that once the cover glass has been opened the cubic phase starts to change its phase and dissolve in the reservoir. Thus, crystals should be fished as soon as possible after opening the cover glass.

In the absence of the structure there are other biophysical techniques that can be used.

2.2. Isothermal Titration Calorimetry (ITC)

Isothermal Titration Calorimetry (ITC) can detect heat changes when a ligand binds to a protein and is the one of the most precise technique for characterization of molecular interactions in solution (Freyer and Lewis). This technique has been used not only for soluble proteins but also for membrane proteins (Lockless *et al.* 2007; Maes *et al.* 2012; Picollo *et al.* 2012; Striegel *et al.* 2012; Rajarathnam and Rosgen 2014). The binding enthalpy is determined as the change of heat for reversible interactions. Furthermore, the equilibrium binding constant (K_D) and the stoichiometry of the interaction can be calculated from the titration curve. Then, the entropy change (ΔS) and the Gibbs free energy (ΔG) are calculated from the K_D value and the enthalpy change (ΔH). The reaction is measured in solution without any labelling of either the protein or the ligand. That information can be used to characterise the substrate and the inhibitor and help to design more potent inhibitors (Freire 2008; Ladbury *et al.* 2010).

$$\Delta G = - RT \ln K_D$$

$$\Delta G = \Delta H - T\Delta S$$

R: Gas constant, K: Absolute temperature,

2.3. Microscale Thermophoresis (MST)

Microscale Thermophoresis (MST) is a relatively new technique compared to other biochemical and biophysical techniques (Stumpfe *et al.* 2010; Wienken *et al.* 2010; Jerabek-Willemsen *et al.* 2011; Seidel *et al.* 2012). The principle of this method is unique in that it measures the molecular interaction from the change of the hydration shell of molecules as described below. Protein solutions are mixed with serial concentrations of a ligand in capillaries. Either the protein or the ligand is tagged by a fluorescent label. Each sample is heated by a focused infrared laser (IR) and the fluorescence of the sample is monitored. The molecules in the system are displaced by the temperature gradient (Duhr and Braun 2006). This motion is related to the solvation entropy and the hydration shell of the protein that is changed by binding the ligand. The binding affinity of the ligand can be determined by measuring the difference in fluorescence in each of the ligand concentrations. This technique has been applied for membrane protein characterization as well (Parker and Newstead 2014; Srinivasan *et al.* 2014).

2.4. Circular Dichroism (CD)

Circular dichroism (CD) is the differential absorption of left-handed and right handed circularly polarized light. It occurs when a chiral material, such as a protein molecule, absorbs circularly polarized light. CD spectroscopy is used to investigate secondary and tertiary structures of proteins. Synchrotron radiation circular dichroism (SRCD) is much brighter than that obtained with a bench-top CD instrument. This enables data with a high signal to noise to be collected with reasonably little amount of protein samples (Javorfi *et al.* 2010). The near UV (250-330nm) region is sensitive to the tertiary structure of aromatic residues of the protein, phenylalanine, tyrosine and tryptophan. In far UV region (170-260nm), the secondary structure of the protein, alpha helices and beta sheets, can be determined. As disruption of the secondary structure reflects unfolding of the protein, it gives information about the stability of the protein from thermal denaturation and/or UV denaturation (Clarke and Jones 2004; Wien *et al.* 2005).

2.5. Transport assays

Several approaches to measure the binding affinity of ligand are described above, in which detailed quantitative parameters of binding reaction can be obtained. These assays do not give information about transport. In addition to the binding affinity, the transport activity is also indispensible. Specifically for membrane transporters, transport activity should be evaluated carefully, since it is different from the binding affinity of the substrates. The assays described above are carried out under solution, thus transporter are required to be solubilised in detergent buffer. While these techniques give highly valuable information, they differ from actual transport situation such as lipidic environment around the protein and sodium and electrochemical potential gradients across the membrane. Transport assays can be carried out either in cells or in proteoliposomes.

In this thesis the cell-based assay uses *E.coli* cells harbouring $ASBT_{NM}$. This is a reasonably rapid system as there is no need for purification and *E.coli* expression takes only a few days. However, cells contains various factors, which cannot be controlled, including a wide variety of membrane proteins and some of them might be capable to uptake/export bile acid across the membrane. On the other hand, transport assay by using proteoliposome demands purification of the protein and preparation of the proteoliposome, in which more accurate controls of molecular ratio of the protein and reproducible results are available. When the lipid is dissolved in the water, owing to their extremely low critical micelle concentrations and water solubility, lipids self-assemble into bimolecular lipid leaflets exposing hydrophilic head group to aqueous phase and facing hydrophobic tail group each other in the core of the bilayer by hydrophobic effect (Gregoriadis 2007). Then, lipid bilayers form large and multilamellar vesicles (MLV) to reduce contact between water phase and

hydrophobic core of the bilyer at the edge (Gregoriadis 2007). Formed MLV are converted to single unilamellar vesicles (SUV) by sonication. Generally disruption of MLV is achieved by sonication with diameters in the range of 15-50 nm (Weissig 2010). One disadvantage of the proteoliposme method is that it is difficult to control the orientation of the protein in the liposome and this can lead to artifacts.

CHAPTER 3

Methods

3.1. Expression and Purification

3.1.1. Preparation of mutants

$ASBT_{NM}$ mutants were cloned as GFP-His_8 fusions into the pET28 (a) derivative vector pWaldoGFPe (Drew *et al.* 2006). $ASBT_{NM}$ mutants were overexpressed in *Escherichia coli* cells (C43 and Lemo21). (Schlegel *et al.* 2012) The plasmid encodes the $ASBT_{NM}$ sequence, a cleavage site for TEV, GFP and a His_8 tag. If the membrane protein expresses and is correctly introduced into the cellular membrane, GFP will give fluorescence. The expression levels of $ASBT_{NM}$ mutants were estimated by measuring the fluorescence of GFP (emission at 512 nm and excitation at 485 nm) from cell culture solution. GFP and His_8 tag can be removed by TEV protease cleavage at the recognition site, (ENLYFQGQ), inserted between the C-terminus of $ASBT_{NM}$ and the N-terminus of GFP.

$ASBT_{NM}$ amino acid sequence; 329 aas, 33,875 Da

MNILSKISSFIGKTFSLWAALFAAAAFFAPDTFKWAGPYIPWLLGIIMFGMGLT
LKPSDFDILFKHPKVVIIGVIAQFAIMPATAWLLSKLLNLPAEIAVGVILVGCCP
GGTASNVMTYLARGNVALSVAVTSVSTLISPLLTPAIFLMLAGEMLEIQAAG
MLMSIVKMVLLPIVLGLIVHKVLGSKTEKLTDALPLVSVAAIVLIIGAVVGAS
KGKIMESGLLIFAVVVLHNGIGYLLGFFAAKWTGLPYDAQKTLTIEVGMQNS
GLAAALAAAHFAAAPVVAVPGALFSVWHNISGSLLATYWAAKAGKHKKPG
SENLYFQ

Primers were designed for each mutant. Mutants of $ASBT_{NM}$ were prepared by using the QuickChange Lightning Site-Directed Mutagenesis Kit (Stratagene) as below. (Table. 3.1) The PCR reaction was carried out in 0.5 mL PCR tubes in a thermal cycler. 1.2 µl of designed forward and reverse primers (10 µM) were mixed with 100 ng of WT $ASBT_{NM}$ plasmid DNA, 5 µl of 10x reaction buffer, 1 µl of dNTP mix and ddH_2O was added to a final volume of 50 µl. 1 µl of *PfuTurbo* DNA polymerase (2.5 U/µl) was then added and the solution gently mixed. The PCR reaction was started with 1 cycle at 95 °C for 2 min, 18 cycles at 95 °C for 20 seconds, 58 °C for 10 seconds and 68 °C for 3.5 min and 1 cycle at 68 °C for 5 min followed by a cooling step at 4 °C. The amplified plasmid was then supplemented with 1 µl of *Dpn I* restriction enzyme (10 U/µl) at 37 °C for 1 hour to digest the parental plasmid.

Table. 3.1. Designed primers for mutants.

Target	Primer sequence
Q77A	Forward: 5' CATCGGCGTAATCGCAAAATTCGCCATTATGC 3' Reverse: 5' GCATAATGGCGAATTTTGCGATTACGCCGATG 3'
T112V	Forward: 5' CTGCTGCCCGGGCGGTGTAGCTTCCAATGTGATG 3' Reverse: 5' CATCACATTGGAAGCTACACCGCCCGGGCAGCAG 3'
S114A	Forward: 5' CCGGGCGGTACGGCTGCAAATGTGATGACCTATC 3' Reverse: 5' GATAGGTCATCACATTTGCAGCCGTACCGCCCGG 3'
N115A	Forward: 5' CGGTACGGCTTCCGCTGTGATGACCTATC 3' Reverse: 5' GATAGGTCATCACAGCGGAAGCCGTACCG 3'
S128A	Forward: 5' CAATGTGGCTTTGGCGGTTGCCGTTAC 3' Reverse: 5' GTAACGGCAACCGCCAAAGCCACATTG 3'
T132A	Forward: 5' GTCGGTTGCCGTTGCGTCTGTTTCCAC 3' Reverse: 5' GTGGAAACAGACGCAACGGCAACCGAC 3'
I146C	Forward: 5' CATTGCTGACTCCCGCCTGCTTCCTGATGCTTGCC 3' Reverse: 5' GGCAAGCATCAGGAAGCAGGCGGGAGTCAGCAATG 3'
G267Q	Forward: 5' GGTATGCAAAACTCGCAGCTGGCCGCCGCGCTTG 3' Reverse: 5' CAAGCGCGGCGGCCAGCTGCGAGTTTTGCATACC 3'
A269C	Forward: 5' CAAAACTCGGGCCTGTGCGCCGCGCTTGCCG 3' Reverse: 5' CGGCAAGCGCGGCGCACAGGCCCGAGTTTTG 3'
H294Q	Forward: 5' CAAAACTCGGGCCTGTGCGCCGCGCTTGCCG 3' Reverse: 5' CGGCAAGCGCGGCGCACAGGCCCGAGTTTTG 3'
N295A	Forward: 5' CAGCGTGTGGCAGAATATCTCCGGC 3' Reverse: 5' GCCGGAGATATTCTGCCACACGCTG 3'

Red indicates mutated bases

3.1.2. Preparation of competent cells

Lemo21 competent cells were prepared as described below. A fresh colony of Lemo21 was selected from an LB agar plate to inoculate 100 ml of LB medium and the culture incubated at 37 °C with shaking at 220 rpm. Cells were grown until the $O.D._{600}$ reached around 0.5. Cells were transferred into two 50 ml falcon tubes and cooled on ice for 10 min. Cells were collected by centrifugation at 2,600 g at 4 °C for 10min and gently resuspended with 10 ml of ice cold 0.1 M $CaCl_2$ followed by a further 10 min incubation on ice. Cells were centrifuged again and the pellet was gently resuspended with 2 ml of ice cold 0.1 M $CaCl_2$ and 20% glycerol. After incubation on ice for 10 min, cells were aliquoted into 50 µl samples and snap froze in liquid nitrogen. Frozen competent cells were stored at -80 °C.

3.1.3. Transformation

50 µl of Lemo21 competent cells were thawed on ice for 10 min before mixing with the plasmid. 1 µl of plasmid (200 ng/µl) was added to the competent cells and the mixture incubated on ice for 30 min followed by a heat shock at 40 °C for 1 min and then on ice for 2 min. 900 µl of LB media were added to the cells and the mixture incubated at 37 °C for 60 min while shaking at 900 rpm. 200 µl of incubated cell culture were then plated onto an LB agar plate supplemented with kanamycin (50 µg/ml).

3.1.4.

Small scale expression screening of $ASBT_{NM}$ mutants

Colonies of transformed C43 cells or Lemo21 cells were picked from LB agar plates and inoculated into 10 ml of LB media supplemented with kanamycin (50 μg/ml) in 50 ml falcon tubes. The cultures were incubated overnight at 37 °C with shaking at 220 rpm. 100 μl of this pre-culture were inoculated into 10 ml of each media, LB, TB and PASM5052 (Studier 2005), supplemented with kanamycin (50 μg/ml) in 50 ml falcon tubes. For PASM5052 media different concentrations of rhamnose, 0 mM, 0.1 mM, 0.25 mM, 0.5 mM, 0.75 mM and 1.0 mM, were added. Cell cultures were incubated at 37 °C and 220 rpm until the $O.D._{600}$ reached 0.5 and induced by the addition of a final concentration of 0.2 mM or 0.4 mM IPTG. Induced cell cultures were incubated overnight at 25 °C or 30 °C and 220 rpm. 1 ml of the cells were transferred into 1.5 ml eppendorf tubes and centrifuged at 15,000 g for 1 min and the supernatants were discarded. The cell pellets were resuspended with 100 μl of 1 x PBS and transferred to 96 wells plate (black Nunc) and the fluorescence emission was measured using a SpectaMax plate reader (Molecular devices) with emission at 512 nm and excitation at 488 nm. Measured fluorescent counts were converted to the concentration of $ASBT_{NM}$ calculated from the fluorescent of pure GFP standard value as described in the formula below.

$$\frac{\text{Fluorescence count of sample}}{\text{Fluorescence count of purified GFP (0.03 mg/ml)}} \times 0.03\ \text{mg/ml} = \text{Concentration of GFP (mg/ml)}$$

$$\frac{33{,}875\ (\text{Molecular weight of } ASBT_{NM})}{26{,}866\ (\text{Molecular weight of GFP})} \times \text{Concentration of GFP (mg/ml)} = \text{Concentration of } ASBT_{NM}\ \text{(mg/ml)}$$

3.1.5.
Fluorescence Size Exclusion Chromatography

The monodispersity of expressed fusion proteins was screened in crude dodecyl- β-D-maltopyranoside (DDM), decyl-β-D-maltopyranoside (DM), nonyl-β-D- maltopyranoside (NM) or n-dodecyl-N,N-dimthylamine-N-oxide (LDAO) solubilised membranes by fluorescence size exclusion chromatography (FSEC) as described below. Crude membranes from 1 ml of *E. coli* cells cultures expressing $ASBT_{NM}$ mutants were centrifuged at 15,000 g for 1 min and the supernatants were discarded. Cell pellets were resuspended in buffer containing 20 mM Tris HCl pH 7.5 and 150 mM NaCl and 1% or 2% of each detergents and incubated for 1 hour at 4°C to solubilise cell membranes. Solubilized membranes were collected by ultra centrifugation at 100,000 g for 45 min. The fluorescence of each supernatant was measured and adjusted to 3,000 with the resuspension buffer. The prepared supernatants were then directly applied to a size exclusion chromatography column equilibrated in a buffer containing detergent and the monodispersity of each mutant was measured with emission at 512 nm and excitation at 488 nm.

3.1.6.
Large Scale Expression and Membrane Preparation

Large scale expression of $ASBT_{NM}$ mutants

Colonies of transformed C43 cells or Lemo21 cells were picked from LB agar plates and inoculated into 10 ml LB media supplemented with kanamycine (50 μg/ml) in 50 ml falcon tubes. The cultures were incubated overnight at 37 °C and 220 rpm. 20 ml of pre-culture were inoculated into 1 l of PASM5052 media (2% inoculation rate) supplemented with kanamycine (50 μg/ml) and 0.75 mM rhamnose. The cells were grown at 37 °C and 220 rpm until the $O.D._{600}$ reached 0.5 and induced by addition of 0.4 mM of IPTG. Induced cell cultures were incubated at 25 °C for 18 hours and 220 rpm. The cells were harvested by centrifugation at 6,000 g for 10 min. Harvested cells were resuspended with 1 x PBS containing protease inhibitor cocktail and stored at -80°C or subjected to cell breakage immediately.

Membrane preparation

The cells were diluted to 360 ml with 1 x PBS containing 1 mM of $MgCl_2$ and 1 mg of DNase. The cells were lysed at incremental pressures of 25 kpsi twice using a cell disruptor (Constant Systems) at 4 °C. Cell debris was removed by centrifugation at 10,000 rpm for 10 min at 4 °C and the supernatant was transferred to ultracentrifugation tubes. Membrane fractions were collected by ultracentrifugation at 41,000 rpm for 1 hour at 4 °C. The supernatant was discarded and the membrane pellet was resuspended in 1 x PBS containing protease inhibitor cocktail using a glass homogenizer. The membrane suspension was flash frozen in liquid nitrogen and stored at -80°C or immediately purified.

3.1.7. Solubilisation and Purification

Following purification steps were performed at 4°C and following the previously established protocol (Hu, 2011). Prepared membranes were solubilised in a buffer containing 1 x PBS, 150 mM NaCl, 10 mM imidazole and 1% DDM and stirred for 1 hour at 4°C. The suspension was cleared by ultracentrifugation at 120,000 x g for 1 hour and unsolubilised membranes were removed. The solubilised membranes were mixed with 1 ml of Ni-NTA Superflow resin (Qiagen) (equilibrated with buffer containing 1 x PBS, 100 mM NaCl, 10% glycerol, 10 mM imidazole and 0.1 % DDM) per 1 mg of GFP-His_8 and incubated with stirring for 1 hour at 4°C. The slurry was loaded onto a glass Econo-Column (Bio-Rad) and washed with 10 column volumes (CVs) of buffer containing 1 x PBS, 150 mM NaCl, 20 mM imidazole and 0.03% DDM. Bound material was washed for a further 10 CVs of buffer containing 30 mM imidazole. The $ASBT_{NM}$-GFP-His_8 fusion protein was eluted in 2 CVs of the same buffer containing 250 mM imidazole. The eluted proteins were mixed with stoichiometric amounts of His_8 tagged Tobacco Etch Virus (TEV) protease to separate $ASBT_{NM}$ mutants and GFP-His_8. Samples were loaded into 30 kDa cut off dialysis membrane bag and incubated with stirring overnight in 3 l of buffer containing 20 mM Tris-HCl pH 7.5, 150 mM NaCl and 0.03% DDM. Dialyzed samples were filtered using a 0.22 μm filter unit and passed through a 5 ml His-Trap column (GE Healthcare) pre-equilibrated with buffer containing 20 mM Tris HCl pH 7.5, 150 mM NaCl and 0.03% DDM. The following purification procedures were varied depending on whether the protein was to be used for a functional assay or for crystallization.

3.2. Biochemical methods

3.2.1. Whole Cell Assay (Radio labeled substrate)

E. coli C43 cells harbouring $ASBT_{NM}$-GFP-His_8 mutants were resuspended in uptake buffer consisting of 1 mM of $CaCl_2$, 1 mM $MgCl_2$, 10 mM Tris-HCl pH 7.5 and 137 mM NaCl. Cells were incubated at 37 °C with uptake buffer containing 1-4 mM taurocholic acid supplemented with 0.16 mM [3H]-taurocholate (PerkinElmer) for 5 min. Transport was terminated by the addition of ice-cold buffer containing 1 mM $CaCl_2$, 1 mM $MgCl_2$, 10 mM Tris- HCl, pH 7.5, 137 mM NaCl and 1 mM taurocholate, and was followed immediately by centrifugation at 20,500 g for 120 seconds. Cell pellets were washed two times in an equal volume of termination buffer and resuspended in 200 µl of the same buffer. The radioactivity corresponding to the internalized substrate was measured by scintillation counting.

Sodium dependent uptake assay

E. coli C43 cells harbouring $ASBT_{NM}$–GFP–His_8 mutants were incubated with 1 µM taurocholic acid supplemented with 0.16 µM [3H]-taurocholic acid for 5 min in different NaCl concentrations 0, 100, 200 and 300 mM.

3.2.2. Proteoliposome transport assay (Radio labelled substrate)

Sample preparation

Purified WT $ASBT_{NM}$ and mutants were concentrated using a 50 kDa cutoff centrifugal concentrator (Millipore) to around 1 to 2 mg/ml, measured at absorbance of 280 nm using NanoDrop (Thermo Scientific), and flash frozen in liquid nitrogen in a 500 µl ependorf tube.

Liposome preparation

L-α-Phosphatidylcholine (from soybean/Sigma), SB lipids, was dissolved in the reconstitution buffer (10 mM MOPS pH 7.0, 5 mM $MgCl_2$, 100 mM KCl) to a final concentration of 20 mg/ml and vortexed for 20 min at room temperature. Under these conditions the resuspended SB lipids form large and multilamellar vesicles (MLV). 1 ml of MLV were transferred to 1.5 ml eppendorf tubes and put on ice. Sonication was carried out with a titanium-tipped probe for 30 seconds at 40 % output (SONICS/*Vibra cell*) followed by 30 seconds rest and then repeated. During this treatment the liquid suspension turned into a slightly hazy transparent solution from a cloudy yellow color that indicated the formation of the single unilamellar vesicles (SUV). The titanium particles released from the tip were removed by centrifugation.

Reconstitution of protein into the liposomes

1 ml of prepared SUV were mixed with 90 µl of 20 % sodium cholate at a final concentration of 40 mM. Cholate was used to reconstitute the membrane protein into liposomes by its solubilization ability with a low critical micellar concentration at 9 – 15 mM. Then, 40 µl of 2 mg/ml purified $ASBT_{NM}$ were added to the destabilized liposome and sodium cholate mixture and this was incubated for 1 hour at room temperature. Reconstitution of $ASBT_{NM}$ into liposomes was accomplished by separating the sodium cholate from the liposome and $ASBT_{NM}$ mixture causing an exchange of sodium cholate from the surface of the ASBT transmembrane domain into the lipid bilayer of the liposomes. Since, the micellar molecular weight of sodium cholate (900 Da), is reasonably smaller than $ASBT_{NM}$ and liposomes, separation can be carried out by using PD-10 column (GE healthcare). 1 mL of incubated solution was applied onto a PD-10 column equilibrated with reconstitution buffer and the solution run though by gravity flow. 1.7 ml of reconstitution buffer was then added and the flowthrough discarded. 2.3 ml of reconstitution buffer were then added and the flowthrough collected in 15 ml falcon tubes. This contains separated $ASBT_{NM}$ reconstituted liposomes. Prepared proteoliposomes were stored at 4 °C and could be kept for 2 days without any appreciable change in transport activity.

Transport assay

Proteolipomes were then used for the taurocholic acid uptake assay. Radiolabeled taurocholic acid was used to monitor uptake ratio. To keep an electrostatic gradient across the lipid membrane, valinomycin, which is a potassium ion selective ionophore, was added to the proteoliposomes,. 150 µl of liposomes were transferred to 1.5 ml eppendorf tube and 5.2 µl of 4 M NaCl and 1 µl of 100 µM valinomycin were added to final concentration of 137 mM and 666 nM respectively. The reaction mixture was pre incubated at 37°C for 5 min before starting the uptake assay. The assay was started by the addition of 4 µM taurocholic acid supplemented with 0.666 µM [3H]-taurocholic acid (PerkinElmer), and incubated at 37°C for 5 min and 900 rpm. Transport was terminated by the addition of 150 µl ice-cold stop buffer containing 10 mM MOPS pH 7.0, 5 mM $MgCl_2$, 100 mM KCl, 137 mM NaCl and 1 mM taurocholic acid, and was followed immediately by application to a PD MiniTrap G-25 column (GE healthcare) to separate proteoliposomes from the taurocholic acid that had not been taken up. A further 700 µl of stop buffer was loaded and the flowthrough collected in a scintillation counting vial containing 2.5 ml of scintillation enhancing liquid (Scintillation plus / Packard biosciences). The radioactivity corresponding to the internalized substrate was measured by scintillation counting. The amount of taurocholic acid transported into the proteoliposomes were measured by the scintillation counter and values for each samples were subtracted from those of NapA as a blank control. NapA, Na^+/H^+ antiporter from *Thermus thermophilus*, was selected as a negative control for the assay. The reason for using NapA instead of the empty proteoliposome was to see the effect of another structurally homologous membrane transporter on the taurocholic acid uptake assay. Uptake ratios were taken as a percentage of WT $ASBT_{NM}$, which was assigned to 100%.

3.2.3. Whole Cell Assay (Fluorescence substrate)

The uptake of rhodamine was measured in *E. coli* C43 whole cells after the expression of WT $ASBT_{NM}$-GFP-His_8, Q77K, T112V, N295A, N295L, S114A+S128A, N115A+T132A, N115A+Q260A, Q260A+Q264A, Q77A+Q264A, S114A and N115A. As a negative control the empty vector expressing GFP -His_8 was used. Time course assays were initiated by the addition of 5 μM rhodamine or rhodamine cholate to 100 μl of cells shaking at 900 rpm on a thermomixer comfort at 37 °C. At specified time points the reaction was terminated by centrifugation at 13,000 rpm for 60 seconds. Cells were washed in equal volumes of 1xPBS, resuspended in 100 μl of fresh 1xPBS and transferred to a 96-well black clear plate (Nunc). Rhodamine fluorescence was measured at 580 nm (excited at 530 nm). The results were normalized for the amount of protein expressed using the GFP fluorescence measured at 510 nm (exc. 488 nm) using a spectrofluorometer.

3.3. Crystallization and structure determination

3.3.1. $ASBT_{NM}$ E260A

3.3.1.1. Crystallization

Purified $ASBT_{NM}$ E260A was concentrated to 4-8 mg/ml using a 50 kDa cutoff centrifugal concentrator (Millipore) and loaded onto a Superdex 200 10/300 gel filtration column (GE Healthcare) equilibrated in 20 mM Tris-HCl, pH 7.5, 0.15 M NaCl, 1 mM taurocholic acid and 0.06% LDAO. The protein peak was collected and concentrated using a 100 kDa cut-off centrifugal concentrator (Millipore) to 30 mg/ml. Purified proteins were flash froze in liquid nitrogen and stored at -80°C or immediately used for crystallization. The sample was diluted with the buffer, 20 mM Tris HCl pH7.5, 150 mM NaCl, to 15 mg/ml. Taurocholic acid was added to the protein solution to a final concentration of 10 mM. Samples were centrifuged at 15,000 g for 30 min at 4°C. Crystallisation trials were carried out with the Mosquito robot and the crystallization screens MemGold and Memsys&Memstart (Molecular Dimensions) and the same condition that gave crystals for the WT was also tried. The protein was mixed 1 µl : 1 µl with reservoir solution containing 50 mM sodium citrate pH 4.5, 70 mM NaCl, and 20-30% PEG 400. 24 wells hanging drop plate was incubated at 20 °C.

Dehydration of crystal

Crystals were harvested using a MicroMesh loop (MiTegen) and directly mounted on the humidity controller HC1 (Sanchez-Weatherby *et al.* 2009). After removing extra precipitant solution from the loop using a small piece of Kimwipe, dehydration was carried out. Different humidity ranges from 40% to 80% and dehydration time from 1 min to 10 min were tested. Dehydrated crystals were frozen in liquid nitrogen and screened using synchrotron radiation at the Diamond Light Source.

3.3.1.2. Data collection and analysis

An X-ray diffraction data set was collected from beamline IO4 at the Diamond Light Source. Diffraction data were collected at 100 K using a beam size of 85 μm x 85 μm at 100% intensity at a wavelength of 1.07 Å (11.58 keV) with an oscillation range of 0.5 °, 2.0 seconds per image and recorded on a CCD detector. The intensities from the collected data were integrated with XDS (Kabsch 2010) and scaled with SCALA in the CCP4 program suite (Winn *et al.* 2011). The initial model was prepared from the wild type structure, 3ZUY. Refinement, model building and electron-density map calculations were performed using Phenix refine (Afonine *et al.* 2012) and COOT (Emsley and Cowtan 2004). Molprobity (Davis *et al.* 2007) was used to monitor and improve protein geometry.

3.3.2. $ASBT_{NM}$ Q77A

3.3.2.1. Crystallization

Q77A mutant was crystallized by the lipidic cubic phase (LCP) method. As one of the advantages of LCP crystallization method is that detergent exchange is not necessary before the crystallization setup the last purification step using size exclusion chromatography was skipped and, after the reverse HisTrap steps, proteins were directly concentrated using a 100 kDa cutoff centrifugal concentrator (Millipore) to a final concentration of 25 mg/ml in the buffer containing 20 mM Tris HCl. 150 mM NaCl, 10% glycerol and 0.03% DDM.

LCP preparation

10 µl of 25 mg/ml of purified proteins were loaded into a gas-tight syringe (100 µl volumes/Hamilton) using a Pipetman with 200 µl tips. The syringe was weighed and the weight of the empty syringe subtracted. The required amount of monoolein was calculated from the ratio of 2 : 3 (wt/wt) of protein and monoolein. The calculated amount of monoolein was added to another gas-tight syringe (250 µl volume/ Hamilton). The two syringes were connected by a coupler assemble. The LCP was mixed by pushing the mixture forwards and backwards between the two syringes until the mixture turned transparent, which indicates LCP formation. The prepared homogeneous LCP was then transferred to a 100 µl syringe and the needle assembly was connected to the syringe for dispensing.

Initial screening

For initial screening, MemGold and MemSys & Memstart crystallization screens were set up by a robot (Mosquito) at 20°C. 50 nl of LCP and 1000 nl of precipitant solution were dispensed onto a glass plate and sandwiched by a thin glass cover plate. These crystallization plates were incubated at 20°C. The plates were observed using a microscope with cross polarizers.

Optimization of conditions

From an initial hit from the screening, optimized custom screening conditions were prepared. The E10 condition of MemSys&MemStart, 0.1 M NaCl, 0.1 M MES pH 6.5, 0.1 M $LiSO_4$, 30% PEG400, was optimized as 0.1 M NaCl, 0.1 M MES pH 5.5 – pH 7.0, 0 M – 0.15 M $LiSO_4$, 24% - 32% PEG400. The LCP crystallization plates were set up with this custom screening by a robot system (Mosquito) at 20°C. 50 nl of LCP and 1000 nl of precipitant solution were dispensed onto the glass plate and sandwiched by a thin glass cover plate. The crystallization plates were incubated at 20°C. The plates were observed using a microscope and tiny crystals were obvious when viewed between crossed polarizers.

Harvesting LCP crystals from sandwich glass plates

The glass cover plate was cut using a glass-cuttting stone. The square-shaped cut glass was then removed using tweezers. As soon as possible after opening, crystals were observed between crossed polarizers and harvested using Micromount (Mitogen) loops. To reduce background scattering, crystals were harvested carefully with a minimum amount of LCP around the crystals. Harvested crystals were immediately cryocooled in liquid nitrogen.

3.3.2.2. Data collection and analysis

An X-ray diffraction data set was collected at beamline I24 at the Diamond Light Source. Diffraction data were collected at 100 K using a beam size of 10 μm x 10 μm 100% beam at a wavelength of 0.98 Å (12.68 keV) with an oscillation range of 0.5 °, 0.1 seconds per images and a Pilatus3 6M detector. The intensities from the collected data were integrated with XDS and scaled with SCALA in the CCP4 program suite. The structure was solved by molecular replacement with Phaser (McCoy *et al.* 2007). The initial model was prepared from the wild type structure, 3ZUY. Refinement, model building and electron-density map calculations were performed using Phenix refine and COOT. Molprobity was used to monitor and improve protein geometry.

3.3.3. Wild type $ASBT_{NM}$

3.3.3.1 Crystallization

Sample preparation

Purified WT $ASBT_{NM}$ was concentrated to 4-8 mg/ml using a 50 kDa cutoff centrifugal concentrator (Millipore) and loaded onto a Superdex 200 10/300 gel filtration column (GE Healthcare) equilibrated in 20 mM Tris-HCl, pH 7.5, 0.15 M NaCl, 1 mM taurocholic acid and 0.06% LDAO. The protein peak was collected and concentrated using a 100 kDa cut-off centrifugal concentrator (Millipore) to 30 mg/ml. Purified proteins were flash frozen in liquid nitrogen and stored at -80°C or immediately used for crystallization. In addition to LDAO, various detergents were tried for crystallization trials including NM, OG, DM, cymal5 and MNG14.

In complex with other bile acids

10 mM of each bile acids, cholic acid, chenodeoxycholic acid, lithocholic acid, glycocholic acid and deoxycholic acid were mixed with crystallization samples and incubated for 30 min on ice and centrifuged at 15,000 g for 30 min at 4°C. Initial crystallization screening, MemGold and Memsys&Memstart (Molecular Dimensions), for $ASBT_{NM}$ in complex with bile acids was conducted using a robot system (Mosquito) with a protein and precipitant ratio of 100 nl : 100 nl. Crystallization plates were then sealed with a thin plastic seal and incubated at 20°C.

In complex with rhodamine

Taurocholic acid and rhodamine were added to the protein solution to a final concentration of 1 mM and 10 mM respectively and incubated for 1 hour at 4°C. Samples were centrifuged at 15,000 g for 30 min at 4°C. Following the results from screening the sparse matrix screens the crystallization condition was optimized. The protein was mixed 1 µl : 1 µl with reservoir solution containing 50 mM sodium citrate pH 4.5, 70 mM NaCl, and 22-24% PEG 400. 24 wells hanging drop plate
was incubated at 20 °C.

Crystals were harvested and dehydrated in the same way as for E260A

3.3.3.2. Data collection and analysis

An X-ray diffraction data set was collected at beamline IO2 at the Diamond Light Source. Diffraction data were collected at 100 K using a beam size of 80 µm x 83 µm 100% beam at a wavelength of 0.98 Å (12.66 keV) with an oscillation range of 0.5 °, 2.0 seconds per images and recorded on a CCD detector. The intensities from the collected data were integrated with XDS (Kabsch 1993) and scaled with SCALA in the CCP4 program suite. The initial model was prepared from the wild type structure, 3ZUY. Refinement, model building and electron-density map calculations were performed using Phenix refine and COOT. Molprobity was used to monitor and improve protein geometry.

3.3.4. Homology modeling of human ASBT

The homology model of human ASBT was prepared by MODELLER (Eswar *et al.* 2006) using $ASBT_{NM}$ WT, 3ZUY, and a multiple sequence alignment of $ASBT_{NM}$ (UniPort ID: Q9K0A9) to the human ASBT (UniPort ID: Q12908), human NTCP (UniPort ID: Q14973), SLC10A3 (UniPort ID: P09131), SLC10A4 (UniPort ID: Q96EP9), SLC10A5 (UniPort ID: Q5PT55), SLC10A6 (UniPort ID: Q3KNW5) and SLC10A7 (UniPort ID: Q0GE19) using ClustalW2 (www.ebi.ac.uk/Tools/msa/clustalw2/). Evaluation of the model was checked by using MolProbity server.

3.4. Biophysical methods

3.4.1. Circular Dichroism (CD) spectroscopy

Sample preparation

As imidazole interferes with CD spectroscopy, it was necessary to remove all traces of imidazole from the sample solution. In the purified sample imidazole still remained after dialysis at less than 2 mM in final concentration. Thus, buffer exchange was required before carrying out the CD experiment. Purified WT and mutants were concentrated to 0.5 ml using a 50 kDa cutoff centrifugal concentrator (Millipore) and loaded onto a Superdex 200 10/300 gel filtration column (GE Healthcare) equilibrated in 20 mM Tris-HCl, pH 7.5, 0.15 M NaCl, and 0.05% DDM. The SEC profile showed a single peak at a retention volume of 13 ml to 15ml. The fractions from this peak were collected and aliquoted into 0.5 ml eppendorf tubes without concentrating to avoid concentrating the DDM. Aliquoted samples were flash frozen in liquid nitrogen and stored at -80°C. Purified $ASBT_{NM}$ was defrosted and the concentration was adjusted to 30 μM with the CD buffer, 20 mM Tris-HCl, pH 7.5, 0.15 M NaCl, and 0.05% DDM.

Near UV (240-340nm)

0.2 ml of samples were prepared with or without 200 μM taurocholic acid. Each sample was loaded into a 10 mm pathlength glass cells and mounted on beamline B23 at Diamond Light Source. Absorption from the near UV wavelength (240-340nm) was measured at 20°C with 10 repeat scans.

Far UV (170-260nm)

Taurocholic acid was added to 30 μM $ASBT_{NM}$ at concentrations of 30, 60, 150, 600, 900, 1200 and 1800 μM respectively and incubated for 30 min at 4°C. 0.2 ml of each samples was loaded into a 10 mm pathlength glass cell and mounted on beamline B23 at Diamond Light Source. Absorption from the far UV wavelength (170-260nm) was measured at 20 °C with 20 repeat scans. CD data at 193 nm was plotted versus number of repeated scan to compare the differences in the unfolded protein ratio at each taurocholic acid concentration.

The data were processed using CD Apps software and Origin software.

3.4.2. Isothermal Titration Calorimetry (ITC)

Sample preparation

Purified WT $ASBT_{NM}$ was concentrated to 4-8 mg/ml using a 50 kDa cutoff centrifugal concentrator (Millipore) and loaded onto a Superdex 200 10/300 gel filtration column (GE Healthcare) pre-equilibrated in the ITC buffer, 1xPBS pH 7.8, 100 mM NaCl and 0.03% DDM. The SEC profile showed a single peak at a retention volume of 13 ml to 15ml. SDS PAGE showed that samples were highly pure without significant contamination of other proteins. The samples were concentrated to 15 mg/ml using 50 kDa cutoff centrifugal concentrator and loaded into 10 kDa cutoff dialysis cassette, (Slide-A-Lyzer Dialysis Cassettes / Thermo scientific). The cassette was incubated with stirring overnight in 3 l of ITC buffer (see below). This dialysis buffer was used for ligand solution preparation. The sample was used for the ITC experiment directly.

ITC experiment

The isothermal titration calorimetry experiments were performed at 25 °C on a MicroCal iTC200 (Malvern) at Oxford University. 200 µl of prepared 227 µM $ASBT_{NM}$ sample was degassed and loaded into the sample cell. 50 mM of taurocholic acid solution was prepared with ITC buffer, 1xPBS pH 7.8, 100 mM NaCl, 0.03% DDM and degassed. The degassed ligand solution was filled into the syringe unit. After a stable baseline had been achieved, the ligand was titrated into the stirred sample cell (1000 rpm). The injection sequence consisted of 2.5 µl injections during 5.0 seconds at 180 seconds spacing up to 16 injections. As a control the dilution factor of the ligand in the ITC buffer was also measured. The titration data were processed using the Origin-ITC software package (Malvern). Heats of ligand dilution were

subtracted from the raw data. The subtracted heat changes for each titration was integrated and plotted versus the molecular ratio of $ASBT_{NM}$ and taurocholic acid. The data were processed using Origin iTC_{200} software.

3.4.3. Microscale Thermophoresis (MST)

Sample preparation

For the MST experiment at Imperial College London, the fluorescence of GFP was used to monitor the protein mobility. Purification procedures were finished by elution of Ni-NTA resin purification. 1 ml of sample was applied onto a PD-10 column (GE-healthcare) equilibrated with the MST buffer and let pass through with gravity flow. Then 1.7 ml of the MST buffer were loaded and the flowthrough discarded. An additional 2.3 ml of MST buffer were then loaded the flow through collected in a15 ml falcon tube. This step was repeated to completely remove imidazole from the sample. The sample was aliquot into 0.5 ml eppendorf tubes and flash frozen in liquid nitrogen and stored at -80°C.

MST experiment

Unlabelled experiment: Purified $ASBT_{NM}$ was diluted to 500 nM with the MST buffer, 20 mM Tris-HCl, 150 mM NaCl and 0.03% DDM, buffer and 10 µl of samples were aliquot into 16 1.5 ml eppendorf tubes. Taurocholic acid was added to the first tube at a final concentration of 2.5 mM then serial dilutions were prepared by transferring 10 µl of samples to the following tubes. (Concentration range from 0.3 µM to 2.5 mM) Each sample were transferred to glass capillaries (Monolith standard capillaries from Nanotemper GmbH) and inserted into Monolith NT.LabelFree (Nanotemper GmbH) for MST-analysis.

GFP labeled experiment: Purified $ASBT_{NM}$ GFP fusion protein was diluted to 50 nM with MST buffer and 10 µl of samples were aliquoted to 16 1.5 ml eppendorf tubes. Taurocholic acid was added to the first tube at final concentration of 20 mM then

serial dilutions were prepared by transferring 10 µl of samples to the following tubes. For example, taurocholic acid concentrations in each tube are 20 mM, 10 mM, 5 mM, 2.5 mM, 1.25 mM, 0.63 mM, 0.31 mM, 0.16 mM, 78.13 µM, 39.06 µM, 19.53 µM, 9.77 µM, 4.89 µM, 2.44 µM, 1.22 µM and 0.61 µM. Various taurocholic acid concentration ranges were also used. Each sample were transferred to the glass capillaries (Monolith standard capillaries from Nanotemper GmbH) and inserted into Monolith NT.115 (Nanotemper GmbH) for MST-analysis.

CHAPTER 4

Results

4. Results

4.1. Expression and Purification

4.1.1. Expression

The following $ASBT_{NM}$ mutants were made, Q77K, Q77L, T112V, S114A, N115A, S128A, T132A, I146C, E260L, G267Q, A269C, H294Q, N295A, N295L, Q77A + E264A, A114A + S128A, A146C + A269C, N115A + T132A, Q260A + N115A and Q260A +Q264A. These mutations were prepared in addition to those made previously by Dr Hu (M48A, Q77A, K217E, E260A, Q264A, N265A, S291A and H294A). (Table. 4.1. lists the mutations and the reasons for making these mutations.) The expression conditions were screened to enable production of large amounts of protein for functional studies and crystallization. The best condition used Lemo21 cells in PASM5052 media (2% inoculation rate) supplemented with 0.75 mM rhamnose. The cells were grown at 37 °C and 220 rpm until the $O.D._{600}$ reached 0.5 and induced by the addition of 0.4 mM IPTG. The induced cells were incubated for 20 hours at 30 °C. All mutants expressed well in this condition with an average yield of 3.8 mg/ l /$O.D._{600}$ of expression. (Fig. 4.1. and Table. 4.2.) About two third of the mutants had similar expression levels to WT (4 mg / l / $O.D_{600}$), whereas the rest of the mutants expressed slightly less well than WT (2-3 mg / l / $O.D_{600}$). These expression levels gave suitable large amounts of homogeneous protein for crystallization studies.

Table. 4.1. $ASBT_{NM}$ mutants

Binding target	Position	Aim
Na1	S114A N115A S128A T132A E260A E260L S114A + S128A N115A + E260A N115A + T132A	Is sodium 1 important for transport?
Na2	Q77A Q77L Q264A Q77A + Q264A	Is sodium 2 important for transport?
	Q77K	Can the positively charged lysine mimic the sodium ion?
Na1 and Na2	E260A + Q264A	What is the effect of preventing any sodium from binding?
Substrate	M48A N265A	Both of these residues are highly conserved throughout the SLC10 family. They are both in the substrate binding pocket – what happens if they are mutated?
	N295A N295L	This makes the only direct hydrogen bonding interaction to the taurocholic acid in the structure. In the human protein the equivalent residue is a leucine.
	H294A	This interacts indirectly with the substrate in the structure through water molecules. It is reasonably conserved throughout the SLC10 family.
Other	S291A	Differences in affinity of drugs binding to mouse and human proteins have been attributed to a mutation at this postion.
	T112V	This residue is also near to taurocholic acid in the structure but its side chain was rather disordered.
	G267Q H294Q	Both of these residues are highly conserved as glutamine throughout mammalian ASBT homolog. They are both in the substrate binding pocket – what happens if they are mutated?
	I146C A269C I146C + A269C	From human ASBT model structure, these residues are both cysteine.

Table. 4.2. Expression screening of $ASBT_{NM}$ WT and mutants

	O.D. $_{600}$	**RFU**	**mg/l**	**mg / l / O.D $_{600}$**
S114A	5.2	87,000	22.6	4.3
N115A	4.0	49,000	12.7	3.2
S128A	5.6	102,000	26.4	4.7
T132A	6.2	91,000	23.6	3.8
E260A	4.8	87,000	22.6	4.7
E260L	4.6	52,000	13.5	2.9
Q77A	4.4	46,000	11.9	2.7
Q77K	4.8	53,000	13.7	2.9
Q77L	4.4	33,510	8.7	2.0
Q264A	5.2	76,320	19.8	3.8
Q77A+Q264A	4.6	46,750	12.1	2.6
Q77A+E260A	5.6	86,800	22.5	4.0
Q260A+Q264A	5.0	46,000	11.9	2.4
M48A	5.0	48,000	12.4	2.5
T112V	5.6	92,000	23.9	4.3
N265A	5.8	82,000	21.3	3.7
G267Q	6.0	100,000	25.9	4.3
S291A	5.2	102,000	26.4	5.1
H294A	5.0	93,000	24.1	4.8
H294Q	5.4	91,000	23.6	4.4
N295A	3.2	84,000	21.8	6.8
I146C + A269C	5.4	91,000	23.6	4.4
K217E	7.0	107,000	27.7	4.0
WT	5.2	80,900	21.0	4.0

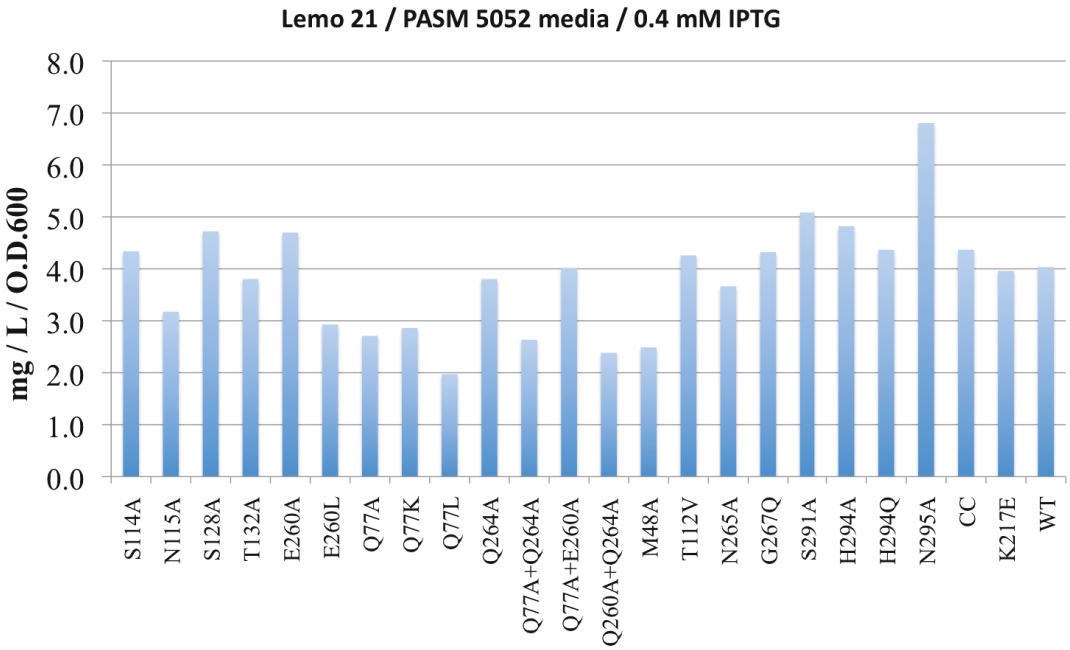
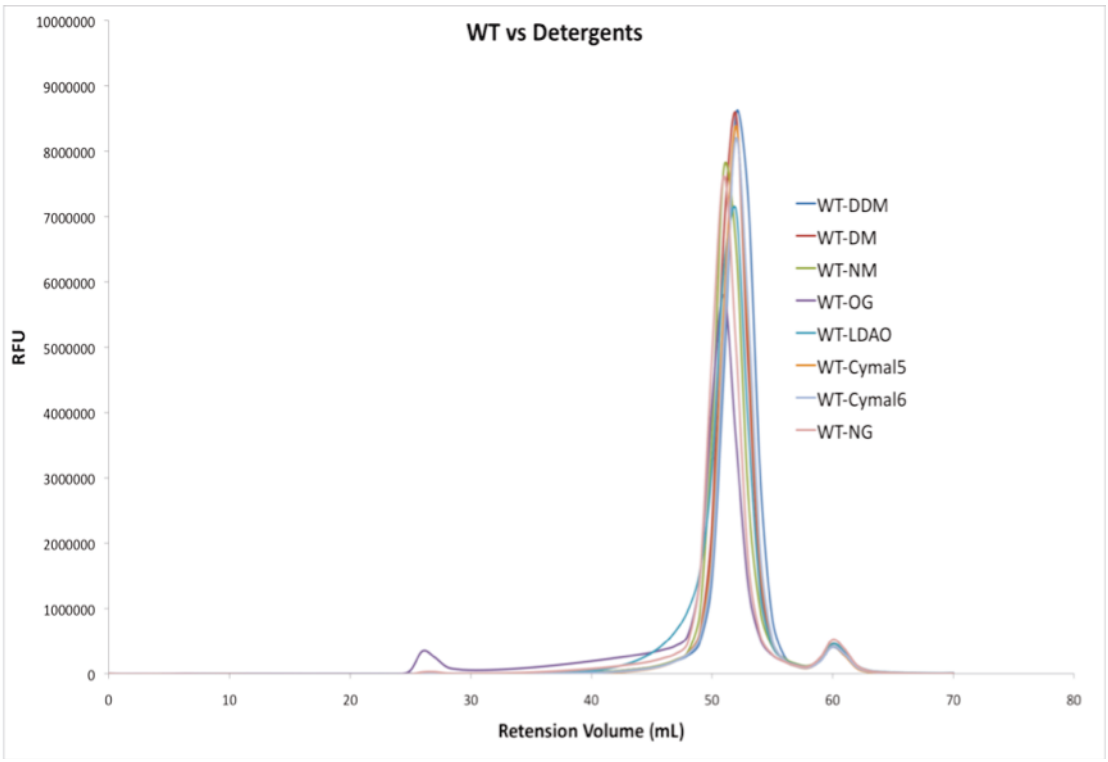


Fig. 4.1. Expression screening of $ASBT_{NM}$ WT and mutants

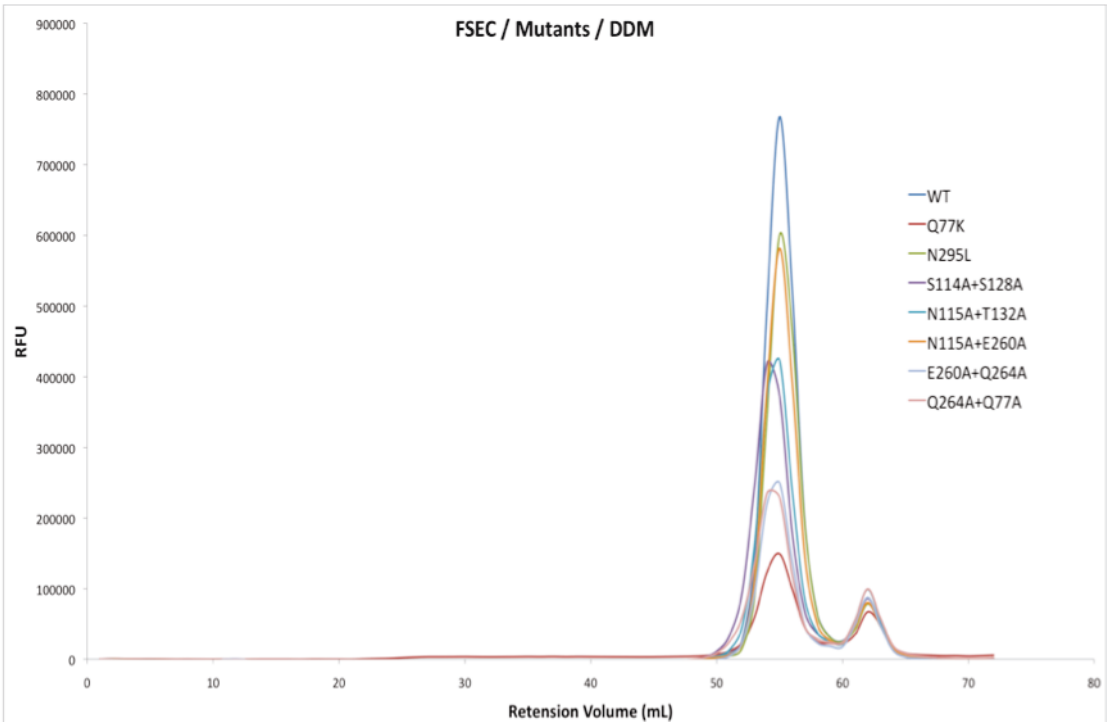
Expression levels were monitored by measuring the GFP fluorescence count from the whole cell and converting this to the amount of $ASBT_{NM}$. The vertical scale represents the amount of $ASBT_{NM}$ (mg/l) over the $O.D._{600}$ value.

4.1.2. FSEC

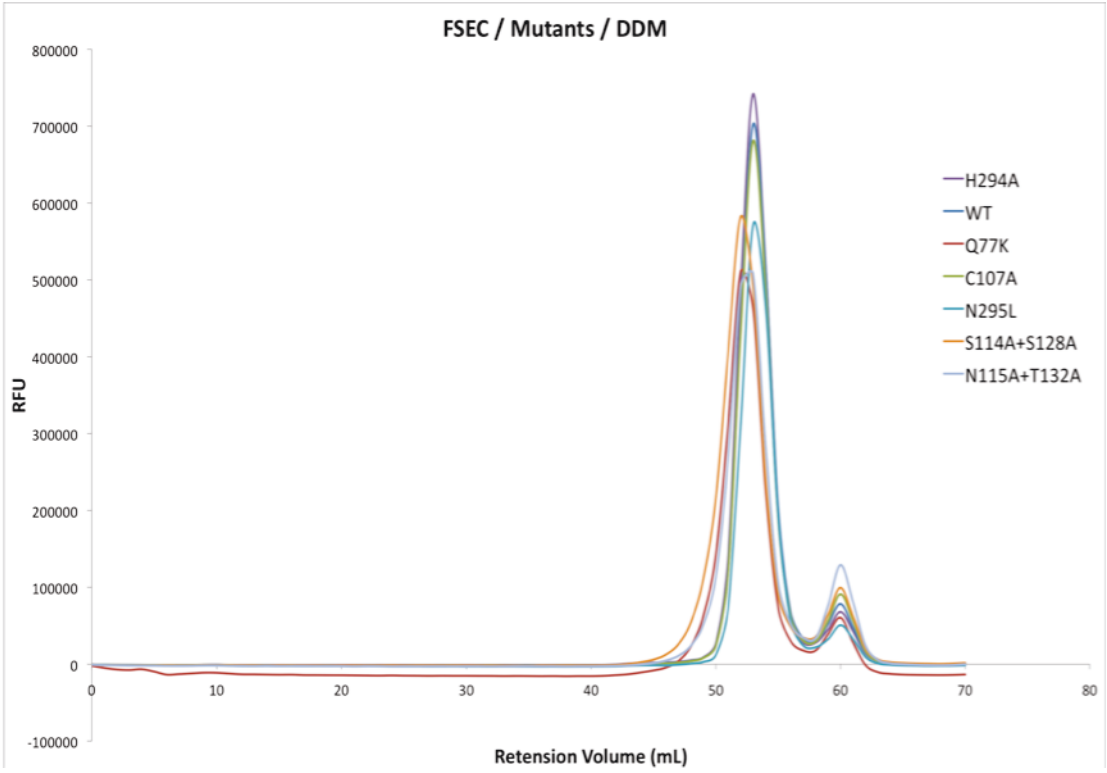
As shown by the results from the Fluorescence Size Exclusion Chromatography screen (FSEC), $ASBT_{NM}$ WT is monodisperse in DDM, DM, NM, NG, OG, LDAO, Cymal5 and Cymal6. (Fig. 4.2.a.) All the $ASBT_{NM}$ mutants had similar profiles. (Fig.4.2.b and c) This suggested that the mutants would be stable enough for purification and crystallization experiments as seen for WT.


WT vs Detergents
RFU
Retension Volume (mL)
WT-DDM
WT-DM
WT-NM
WT-OG
WT-LDAO
WT-Cymal5
WT-Cymal6
WT-NG

a


FSEC / Mutants / DDM
RFU
Retension Volume (mL)
WT
Q77K
N295L
S114A+S128A
N115A+T132A
N115A+E260A
E260A+Q264A
Q264A+Q77A

b



c

Fig. 4.2. FSEC analysis of $ASBT_{NM}$ WT and mutants.

WT and all the mutants show monodipersed peaks at the retention volume of 50 ml to 55 ml. a. $ASBT_{NM}$ WT in 8 detergents, DDM, DM, NM, OG, LDAO, Cymal5, Cymal6 and NG. b. FSEC analysis in DDM for WT, Q77K, N295L, S114A+S128A, N115A+E260A, E260A+Q264A and Q264A+Q77A. c. FSEC analysis in DDM for WT, H294A, Q77K, C107A, N295L, S114A+S128A and N115A+T132A.

4.1.3. Purification

$ASBT_{NM}$ WT and mutants were purified using established protocols by affinity purification using Ni-NTA resin following by TEV cleavage. GFP was removed using a second HisTrap column after the protein had been cleaved. The purities of each of the proteins are shown in (Fig. 4.3.)

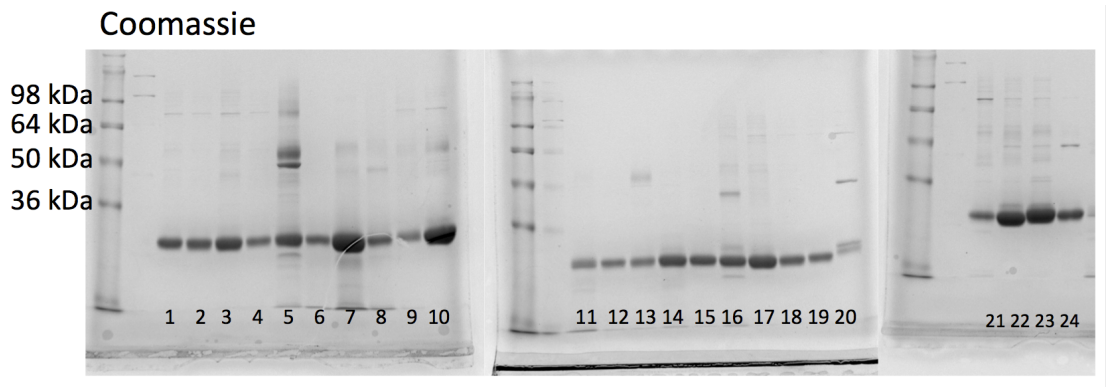


Fig. 4.3. SDS-PAGE analysis of $ASBT_{NM}$ WT and mutants.

S114A (lane 1), N115A (lane 2), S128A (lane 3), T132A (lane 4), E260A (lane 5), E260L (lane 6), Q77A (lane 7), Q77K (lane 8), Q77L (lane 9), Q264A (lane 10), Q77A+Q264A (lane 11), Q7A+E260A (lane 12), Q260A+Q264A (lane 13), M48A (lane 14), T112V (lane 15), N265A (lane 16), G267Q (lane 17), S291A (lane 18), H294A (lane 19), H294Q (lane 20), N295A (lane 21), I146C+A269C (lane 22), K217E (lane 23), WT (lane 24). The SDS-PAGE shows highly purified samples. In average 2-3 mg of purified proteins were obtained from 1 l of cell culture.

4.2. Biochemical methods

4.2.1. Whole cell assay (Radio labelled substrate)

From previously published data by Hu et al (2011), the activities of the wild type, Q77A, E260A, N265A and N295A were measured by a cell-based assay using a radio labeled substrate. To obtain more functional information, this assay was carried out for all the other mutants. However, initial experiments showed some inconsistency. At this point it was decided to turn to proteoliposomes to eliminate any unknown factors that could affect the uptake assay system, such as different expression levels or a wide variety of membrane proteins some of which might be capable to uptake/export bile acid across the membrane.

4.2.2. Proteoliposome transport assay

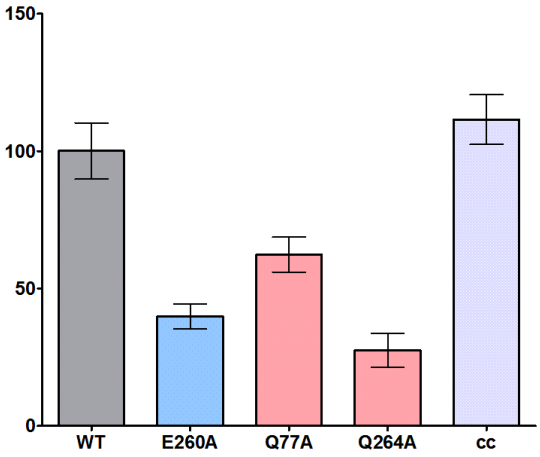
$ASBT_{NM}$ transports its substrate across the membrane from higher to lower concentration of sodium ions. Proteoliposomes were prepared with no sodium inside and a high sodium concentration outside. Thus, though $ASBT_{NM}$ is likely to be inserted into the lipid bilayer in different orientations the assay measures only substrate uptake into the proteoliposome. The results of the assay are shown in Fig. 4.4.

Control of the assay

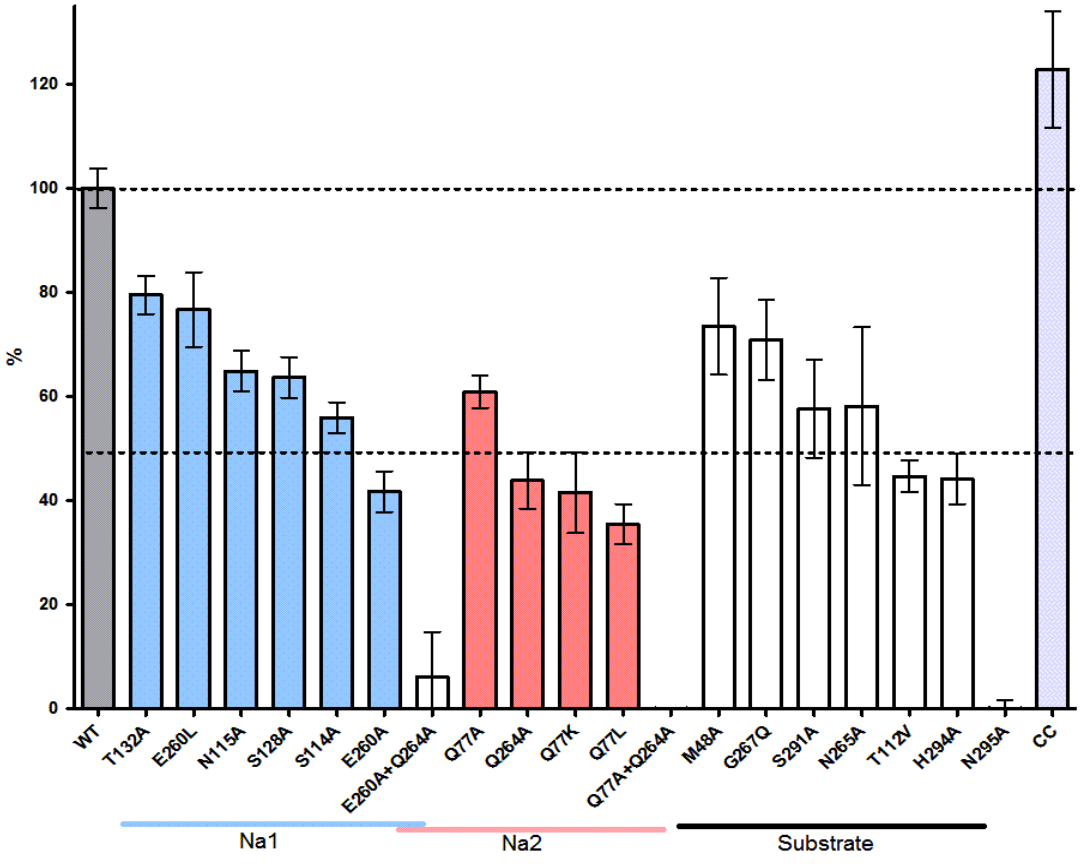
The assay was prepared with both positive and negative controls. Negative control: NapA was selected as a negative control for the assay. The assay result showed significantly lower uptake of taurocholic acid for NapA compared to $ASBT_{NM}$ WT. Positive control: From a homology model of human ASBT, C144 and C270 (I146 and A269 in $ASBT_{NM}$) are both within disulphide bond formation of cysteines 105 and 106, which are equivalent to C107 and C108 in $ASBT_{NM}$. Though in the reduced environment of the cell membrane it is unlikely that the residues would form a disulphide bond it was interesting to see whether a protein with these disulphide bridges could be made. This proved to be a good positive control in the assay as the mutations are not next to either the sodium ion or substrate binding sites. The proteoliposome transport assay shows almost the same activity for this mutants compared to WT.

In general the assays were repeated three times using protein from the same purification batch. The reproducibility of the results from the transport assay with different batches of proteoliposomes was confirmed with WT and E260A, and reproducibility among different batches of purification samples was tested with WT,

Q77A, Q264A, E260A and I146C+A269C in two different experiments using slightly different protocols that were carried out in two separate visits to Sweden where the assays involving radioactivity were carried out. The experimental condition of the 2nd experiment was modified from the 1st experiment; the amount of proteoliposome for the assay was changed from 50 µl to 150 µl to enhance the signals. Among these samples, Q77A, E260A and I146C+A269C showed similar values, around 60%, 40% and 100% respectively, whereas Q264A varied slightly in the two experiments. (Fig. 4.4.)


150
100
50
0
WT
E260A
Q77A
Q264A
cc

a


%
120
100
80
60
40
20
0
WT
T132A
E260L
N115A
S128A
S114A
E260A
E260A+Q264A
Q77A
Q264A
Q77K
Q77L
Q77A+Q264A
M48A
G267Q
S291A
N265A
T112V
H294A
N295A
CC
Na1
Na2
Substrate

b

Fig. 4.4. Proteoliposome transport assay results.

The amount of radio labeled taurocholic acid transporter for each mutant were converted to a percentage of the WT activity after the transport measured for the negative control NapA was subtracted. The grey column shows the WT activity, blue represents Na1 mutants, red represents Na2 mutants, white represents substrate binding mutants and light blue represents I146C+A269C (CC). (The double mutant involving both Na1 and Na2 binding sites E260A+Q264A is also in white.) a) The 1st experiment b) The 2nd experiment.

Table. 4.3. Proteoliposome transport assay result (2nd experiment).

	%	Error
WT	100.0	3.8
T132A	79.5	3.7
E260L	76.7	7.2
N115A	64.9	4.0
S128A	63.7	3.9
S114A	56.0	3.0
E260A	41.8	3.9
Q77A	60.9	3.1
Q264A	43.9	5.4
Q77K	41.6	7.8
Q77L	35.5	3.9
E260A+Q264A	6.1	8.7
Q77A+Q264A	0.0	3.3
M48A	73.5	9.3
G267Q	70.9	7.8
S291A	57.7	9.4
N265A	58.2	15.2
T112V	44.7	3.0
H294A	44.2	4.8
N295A	0.0	7.6
I146C+A269C	122.8	11.2

Na1 & Na2 mutants

The Na1 mutants, T132A, E260L, N115A, S128A, S114A and E260A, have activities from 40% to 80% of the WT, whereas, the Na2 mutants, Q77A, Q264A, Q77K and Q77L have from 35% to 60% activity. (Fig. 4.4 and Table. 4.3.) Na1 mutants are reasonably active with more than 50% activity except E260A with 40%. Na2 mutants are less active than Na1 mutants with lower than 50% activity except Q77A with 60%. Notably, double mutants of E260A & Q264A and Q77A & Q264A completely lost uptake activity.

Substrate mutants

Mutants of substrate binding pocket residues, M48A, G267Q, S291A, N265A, T112V, H294A and N295A, appeared to have moderate activity from 45% to 75% except N295A, which showed no activity.

Comparison with the previously published data

For unknown reason, whole cell transport assay using radio labeled ligand did not work in this study that was well reproducible in the previous studies. It would due to the various factors in the living bacterial cell that cannot be controlled experimentally. Thus, instead of optimizing the experimental conditions to reproduce the proper condition, proteoliposome transport assay was investigated. Compared to the whole cell transport assay result from the previously published data, there are some inconsistencies between the transport activities of mutants. Q77A shows less than 10% activity in the whole cell assay and 60% in the proteoliposome assay. N265A and N295A show around 20% activities in the whole cell and 60% and 0% activities in the proteoliposome assay. E260A shows the same activity in both assay systems.

There are some possibilities to answer this inconsistency, for example, whole cell assay involves the effect of other intrinsic transporters, proteoliposome assay is performed with purified proteins that would be more or less damaged during the process and proteoliposome assay was not repeated with different batch of purified samples. Further investigation is required to understand these differences.

4.2.3. Whole cell assay (Fluorescence substrate)

Cell based assay

Previously an uptake assay was carried out using radioactive substrate (tritiated taurocholic acid) and *E.coli* cells harbouring $ASBT_{NM}$ (Hu, 2011). As it was not possible to carry out radioactivity work at Diamond or the RCaH it was decided to investigate whether we could develop a fluorescence based assay using cholate linked to rhodamine. Rhodamine cholate gave a good signal in the assay compared to the negative control of cells expressing GFP. Thus, the signal of rhodamine cholate seemed to be related to the expression of $ASBT_{NM}$. As only a small amount of rhodamine cholate was available, the assay was tried with rhodamine and it gave a good signal as well. Then, the assay was set up using rhodamine alone. However when the mutants were tested all mutants Q77K, T112V, N295A, N295L, S114A + S128A, N115A + T132A, N115A + Q260A, Q260A +Q264A, Q77A + Q264A, S114A and N115A show very similar values. (Fig. 4.5.)

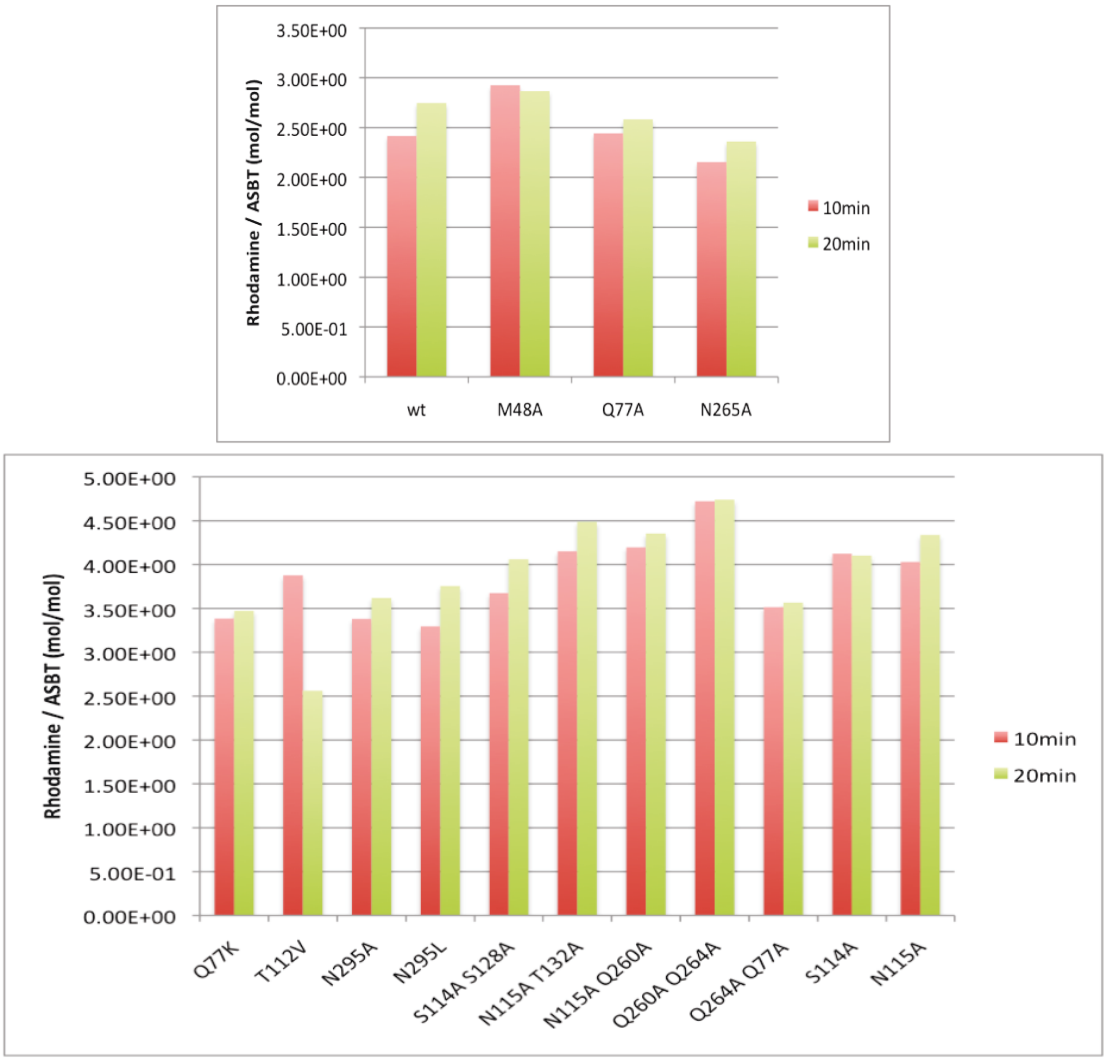
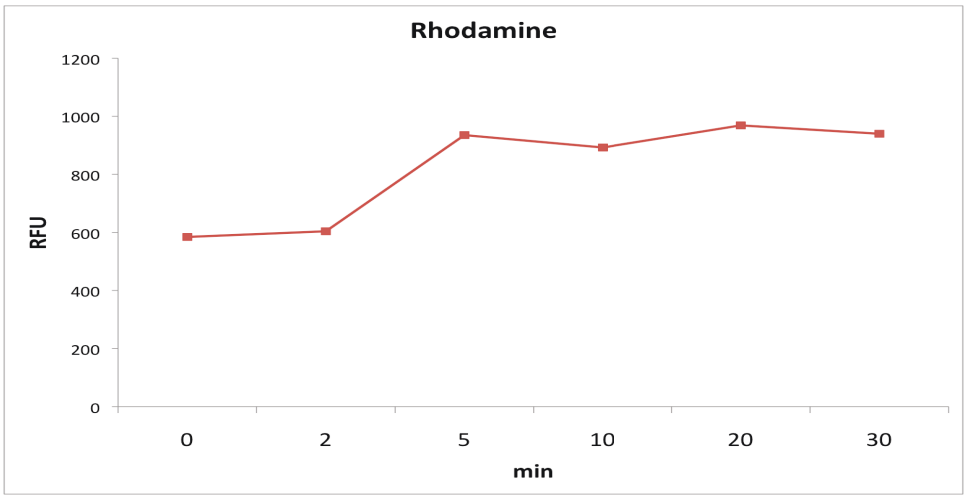


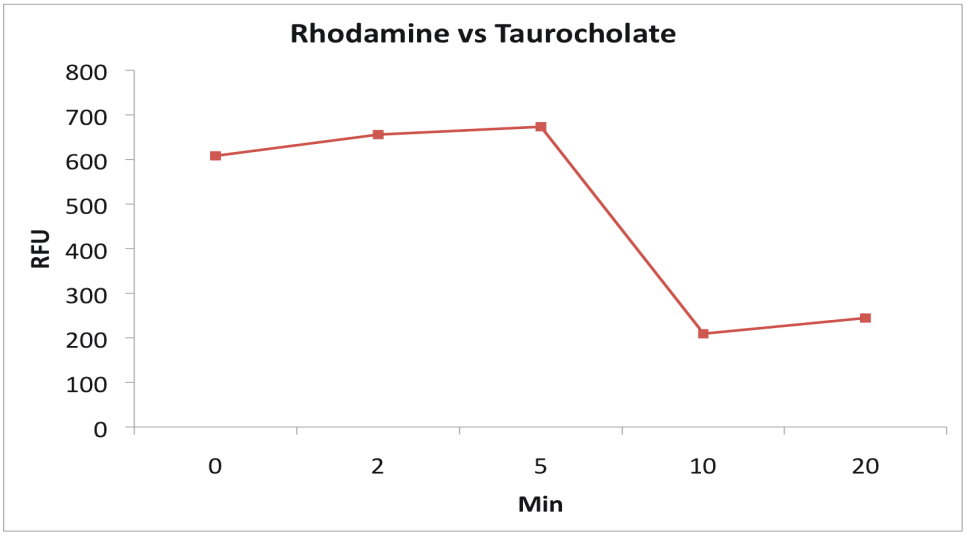
Fig. 4.5. $ASBT_{NM}$ hourbouring *E.coli* whole cell and rhodamine assay.

The *E.coli* cells were mixed with rhodamine and incubated at 37 °C. After 10 min (red column) and 20 min (green column) incubation, cells were separated from the rhodamine solution and washed with buffers. Molecular ratio between $ASBT_{NM}$ and rhodamine were calculated from the fluorescence of rhodamine and GFP.

In the initial experiments taurocholic acid was omitted from the stop buffer. In transport assays the addition of "cold" substrate in the stop buffer is often used to remove any fluorescence substrate that has bound to the protein rather than having been transported. The addition of taurocholic acid to the stop buffer caused the fluorescence count to decrease. (Fig. 4.6.)



a



b

Fig. 4.6. Time course fluorescence based assay of $ASBT_{NM}$ in *E.coli* cells.

a). Time course assay of $ASBT_{NM}$ and rhodamine. b). taurocholic acid was added at 5 min incubation. Fluorescence of rhodamine significantly decreased after the addition of taurocholic acid.

This appears to be more consistent with binding rather than transport. As no difference could be observed in the binding of rhodamine between WT and mutants this assay was not thought to be appropriate to evaluate the mutants. However, from these results it appeared that rhodamine could bind to the extracellular side of $ASBT_{NM}$. It was thought that it might be possible to use rhodamine as a ligand that could trap the conformation of $ASBT_{NM}$ in the outward facing state.

4.3. Crystallization and structure determination

Crystallization of all the mutants, especially mutants in the sodium binding sites, was tried. Among those mutants, two structures were solved, Q77A and E260A. The proteoliposome transport assay result showed that both E260 and Q77 are important residues for the transport of taurocholic acid. Thus, these mutants were focused on.

4.3.1. E260A

The E260A mutation showed around 40% of WT transport activity, which was the lowest among the mutants in the Na1 binding site.

4.3.1.1. Crystallization

The E260A mutant crystallised in similar conditions to the WT. Crystals were grown at 20°C using the vapour diffusion method. Crystals appeared overnight and reached a maximum size after 3-4 days. (Fig. 4.7.) The sizes of the crystals were under 50 µm. It was found that dehydration of the crystal was necessary to improve the resolution of the diffraction data as seen for the WT crystals.

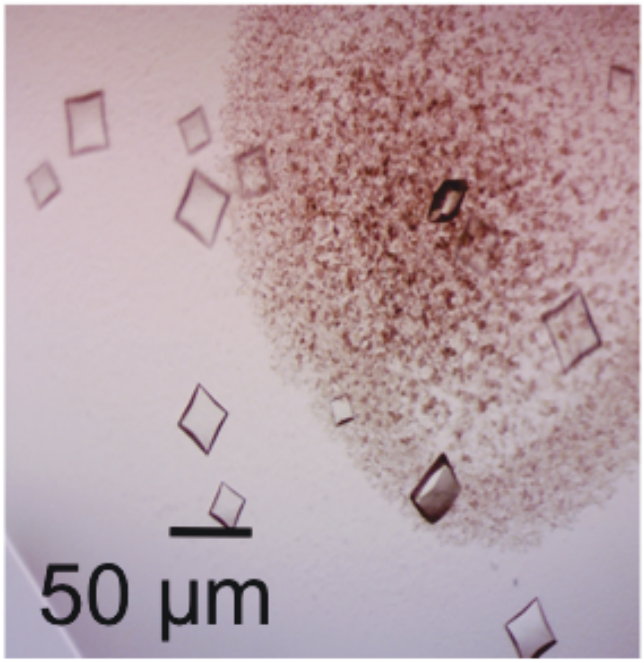


Fig. 4.7. Crystal of $ASBT_{NM}$ E260A.

Crystals of $ASBT_{NM}$ E260A grown using the vapour diffusion method. The size of the crystal is around 50 mm.

4.3.1.2. Data Collection and Analysis

These crystals had the same space group as the wild-type structure and diffracted to 3.0 Å. (Fig. 4.8.) (Table. 4.4.) A data set was collected from a single crystal. The resolution limit of the data to use for further processing was determined to be 3.0 Å where the Correlation coefficient (CC_{50}) was 0.52. The WT structure, 3ZUY, was used as the initial model for the refinement and the Free R column was copied from the reflection file used for 3ZUY. Refinement parameters were screened to find the best parameters. 3 cycles of XYZ coordinate refinement was selected as a standard refinement parameter. In addition this the following options were tested individually: Individual B-factors, Group B-factor, Occupancies, TLS and using Reference model restraints to the previously solved WT structure (PDB code; 3ZUY). Among these options, Individual B-factors and Reference model restraints gave the best improvement as judged by the R-value and R_{free}-value. It appeared that the best R-values were obtained after 4 cycles in Phenix and did not improve with further cycles. The main changes that were carried out during model building were as follows: Glutamate 260 was replaced with an alanine; the sodium ion was placed in the Na2 binding site bound to Q77 and Q264, whereas no electron-density was observed in the Na1 binding site. Two molecules of taurocholic acid were placed in the inward binding pocket and at the surface of the protein respectively in the same positions as for the WT structure. The final R-value was 23.2% and the R_{free}-value was 29.5%. RMSD from ideal values were 0.012 (Bond length) and 1.788 (Bond angle). Other statistics including validation parameter can be seen in the table. 4.8.

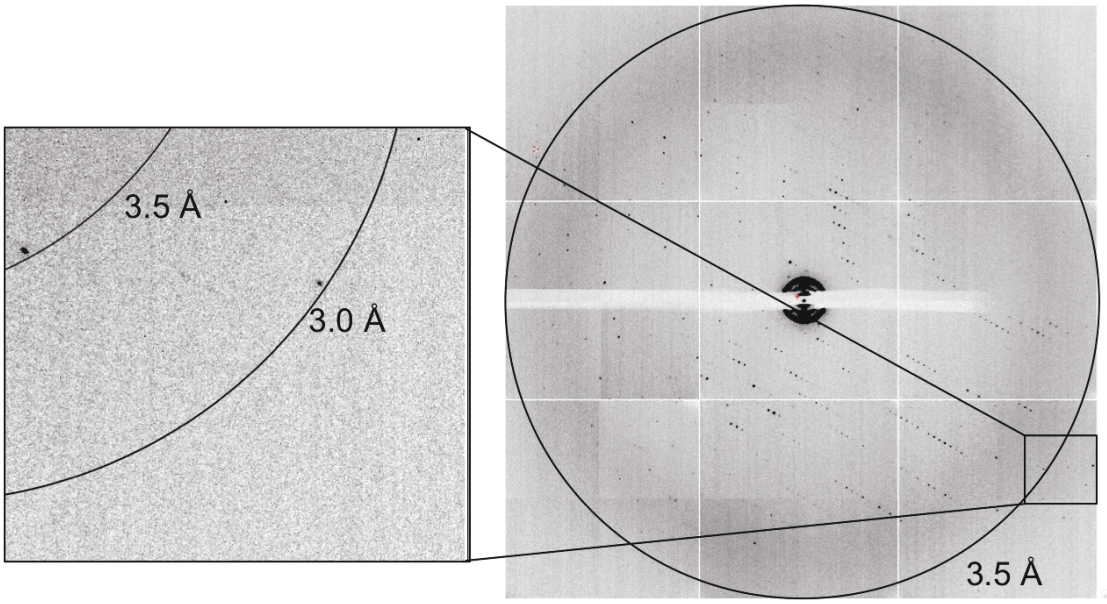


Fig. 4.8. $ASBT_{NM}$ E260A X-ray diffraction image.

The black circle indicates the diffraction limit at a resolution of 3.5 Å. The left box shows the spots at the highest resolution.

Table. 4.4. $ASBT_{NM}$ E260A data collection and refinement statistics.

Crystal	**E260A**
Wavelength (Å)	1.0703
Beamline	IO4 / DLS
Oscillation range	0.5 °
Exposure time	2.0 s
Transmission	100%
Beam size	85 mm x 85 mm
Space group	$P4_122$
Resolution (Å)	80.6 - 3.0 (3.2 - 3.0)
CC_{50}	0.99 (0.52)
Cell dimensions (Å)	***a***=***b***=72.5, ***c***=161.1
	α=β=γ=90
Number of measured reflections	74076
Number of unique reflections	10024
Completeness (%)	96.9 (82.6)
Redundancy (%)	7.4 (3.1)
$I/\sigma(I)$	13.0 (1.1)
R_{merge} (%)[a]	10.5 (71.8)
Solvent content (%)	64

Refinement	
Resolution (Å)	48.9 – 2.9 (3.1-2.9)
Number of reflections	17681
R-factor (%)	23.3
R-free (%)	25.2
R.m.s.d. from ideal values	
Bond lengths (Å)	0.005
Bond angles (°)	1.15
Ramachandran outliners (%)	0.0
Ramachandran favored (%)	99.7
Rotamer outliners (%)	0.4

Values in parentheses are for the high resolution shells.
[a] $R_{merge} = \Sigma_{hkl} \Sigma_I |I_i(hkl) - \langle I(hkl) \rangle| / \Sigma_{hkl} \Sigma_I I_i(hkl)$, where $I_i(hkl)$ is the intensity of an individual reflection and $\langle I(hkl) \rangle$ is the average intensity.

The electron density showed that no large scale conformations had taken place relative to the WT structure, 3ZUY. The electron density at the Na1 binding site is consistent with an alanine residue instead of glutamate at position 260 (Fig. 4.9.a.) Negative difference density was observed when glutamate was refined at this position. (Fig. 4.9.b)

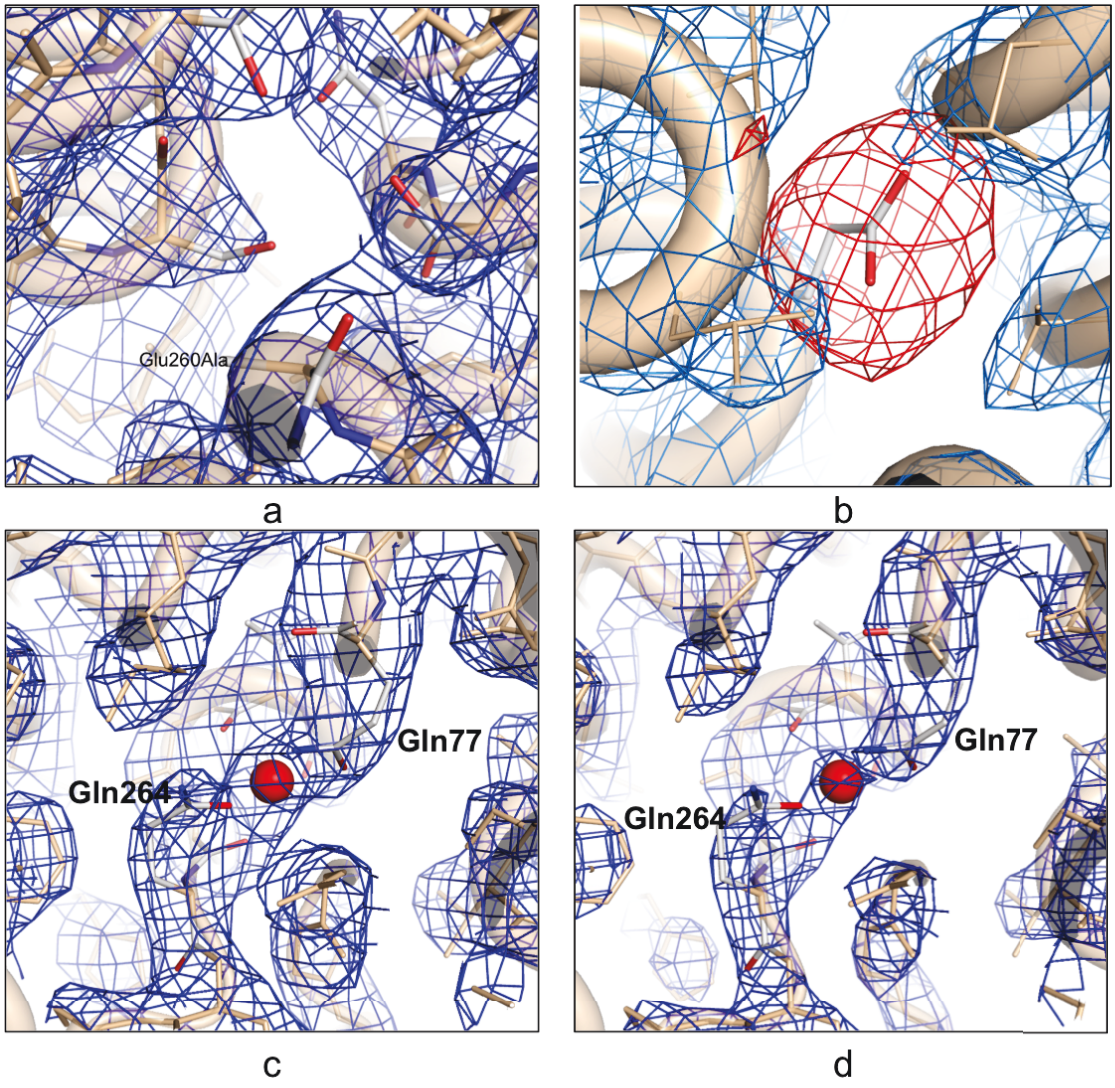


Fig. 4.9. ASBT$_{NM}$ E260A X-ray structure and electron densities.

Electron density map of E260A. a). The electron density at the Na1 binding site. The 2mFo-DFc map was calculated at 1.0 sigma (blue mesh). Glutamate 260 was substituted to alanine. b). 2mFo-DFc map (blue mesh) and mFo-DFc map (red mesh)

were calculated for glutamate 260 at 1.0 sigma and -3.0 sigma respectively. The negative mFo-DFc map can be seen around the side chain of glutamate 260. c). The electron density at the Na2 binding site in the presence of a sodium ion. The 2mFo-DFc maps were calculated at 1.0 sigma and d) 2.0 sigma. The electron density for Na2 can be clearly observed.

Good electron density was seen in the Na2 binding site even when the maps were calculated at 2.0 sigma, (Fig. 4.9. c. and d.) whereas no electron density was observed for the sodium ion in the Na1 binding site. To prove this observation did not come from the low resolution of diffraction data, electron density maps for the wild-type structure were calculated at the same resolution, 3.0 Å or lower, and compared with the maps from the E260A structure. (Fig. 4.10.) In these maps the electron density of Na1 in the wild type was clearly observed (even calculated at 4 Å, Fig. 4.10.b).

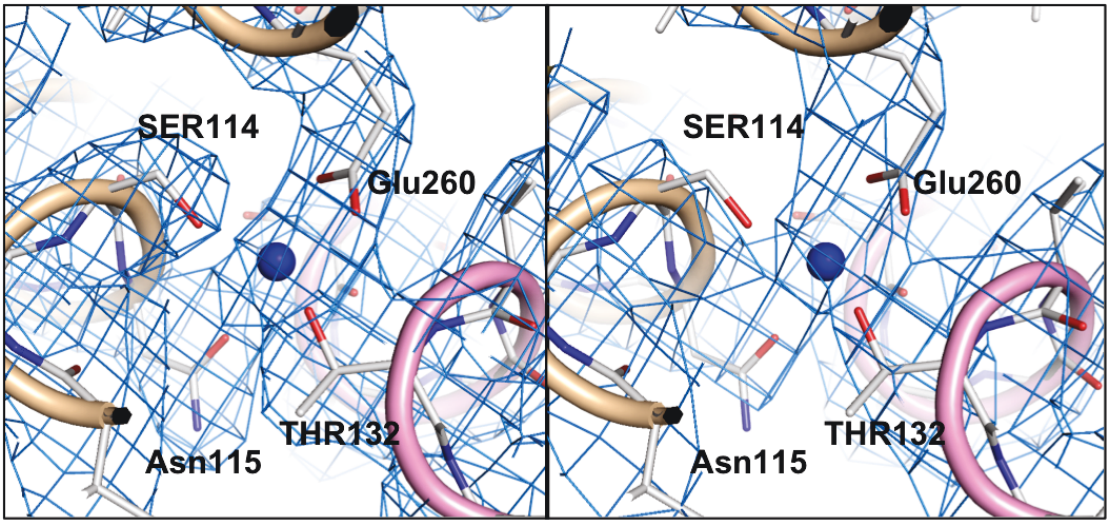


Fig. 4.10. The Na1 binding site of $ASBT_{NM}$ WT X-ray structure and electron densities.

2mFo-DFc maps in the Na1 binding site of $ASBT_{NM}$ WT a). at 3.0 Å and b). at 4.0 Å. 1.0 sigma maps were shown as blue mesh. Na1 was represented as blue sphere and electron density was clearly observed.

When the Na1 from the wild type structure was included in the E260A structure (Fig. 4.11.) strong negative electron density was observed in this site.

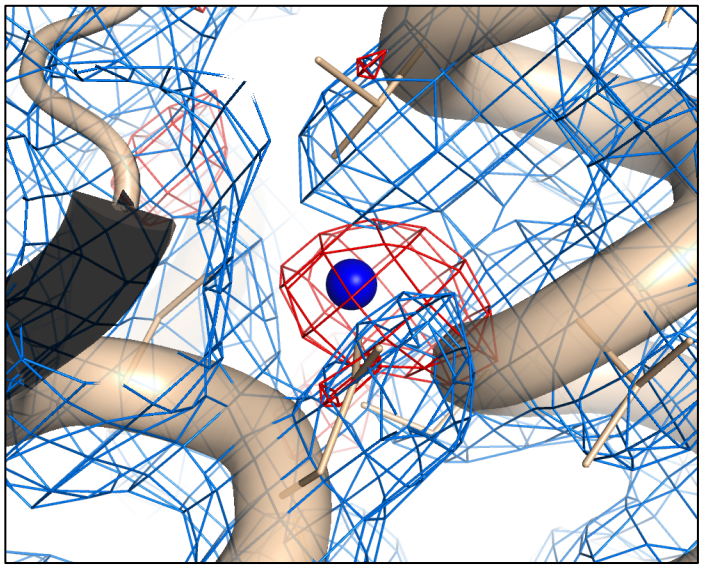


Fig. 4.11. The Na1 binding site of ASBT$_{NM}$ E260A X-ray structure and electron densities.

2mFo-DFc map (1.0 sigma) and mFo-DFc map (-3.0 sigma) shown in the region of the Na1 binding site. Na1 (blue sphere) was superposed from 3ZUY WT structure and strong negative electron density was observed.

As a final check isomorphous difference Fo-Fo maps were calculated by using the structure factors of the WT and E260A with phases calculated using the WT structure. Differential maps at -3.0 sigma levels showed that clear negative electron density was observed at the positions of side chain of E260, Na1 and a water molecule that had been present in the WT structure. (Fig. 4.12.) Notably, no electron density was observed in this map at the Na2 position. From these data it seems that substitution of glutamate 260 with an alanine causes Na1 to be lost, or at least much more weakly bound, but has little effect on Na2.

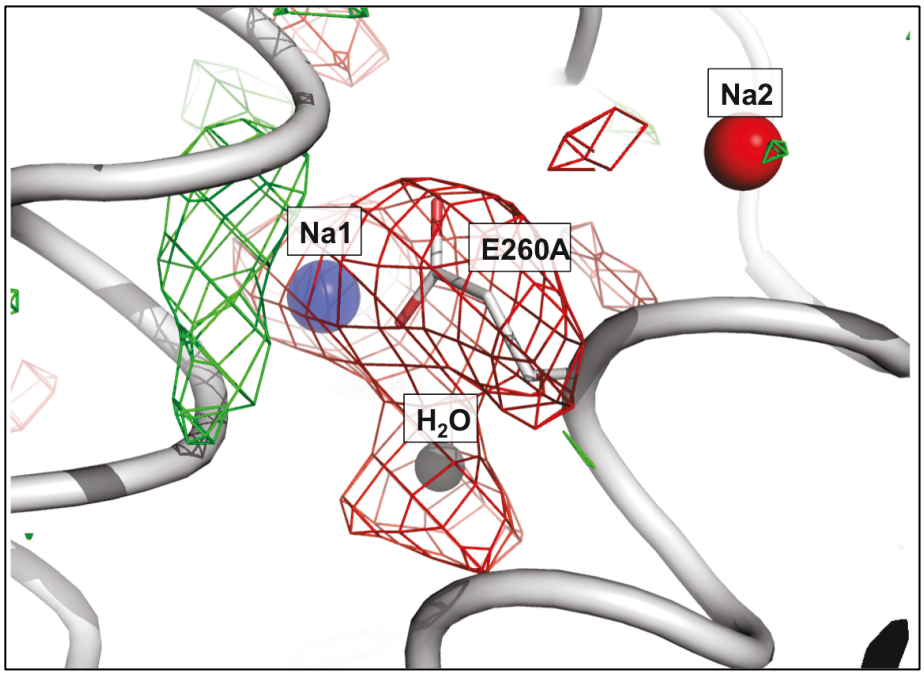


Fig. 4.12. Fo-Fo maps showing the differences between the WT and E260A structures.

The red mesh shows the Fo-Fo map at –3.0 sigma and the green mesh at 3.0 sigma.

A comparison of the $ASBT_{NM}$ WT, 3ZUY, and the E260A structures gives an RMSD 0.24 based on the respective Cα atoms. No large conformational changes were observed in either the taurocholic acid or sodium ion binding sites. (Fig. 4.13.)

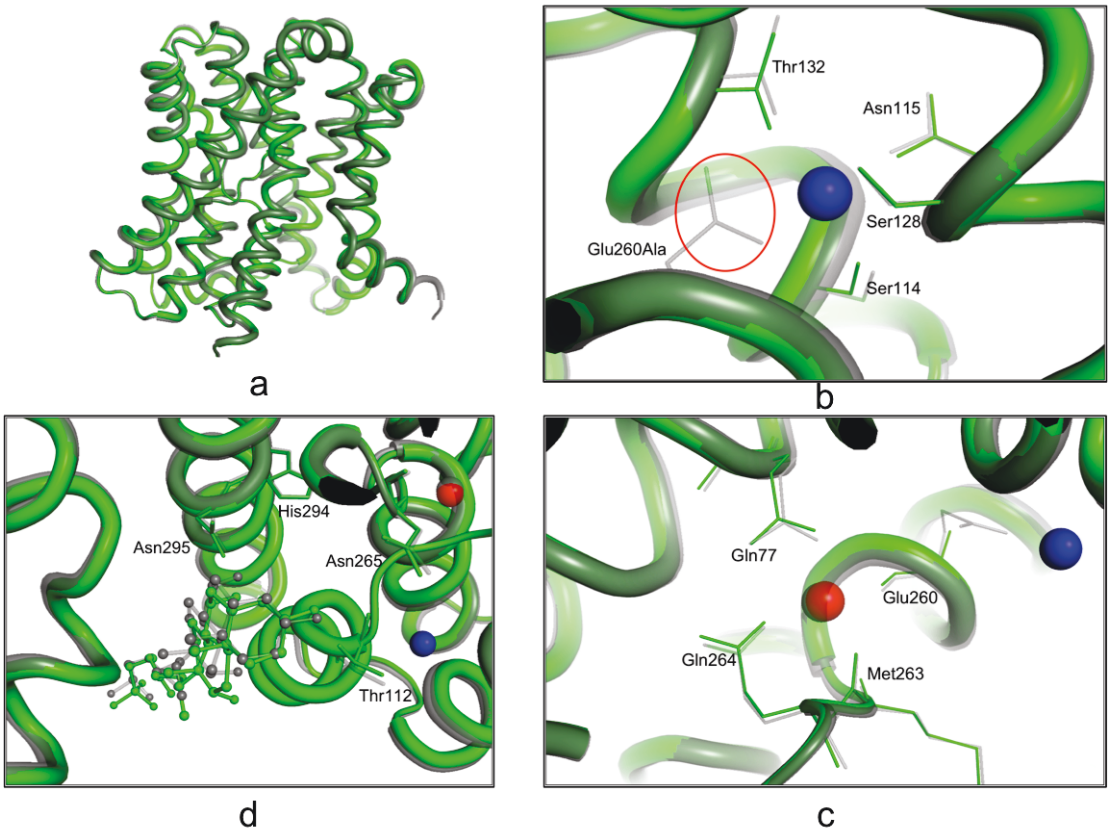


Fig. 4.13. Superposition of WT (3ZUY) and E260A structures.

The WT is shown as a grey ribbon and E260A as a green ribbon. The Na1 from WT is shown as a blue sphere and Na2 from both WT and E260A as red spheres (overlapped). a). Overview of superposed structures. b). Superposed Na1 binding site. The red circle indicates the position of the side chain of E260 in the WT structure. c). Superposed Na2 binding site. The Na2 from WT and E260A were assigned at almost the same position. d) Superposed taurocholic acid binding site. Minor changes were observed between the two molecules.

In summary, the mutation from glutamate to alanine at residue 260 causes Na1 to be lost from the binding site. Neither the mutation nor the loss of Na1 caused any conformational change with respect to the previously solved WT structure.

4.3.2. Q77A

Q77 is one of the two residues that bind the Na2 through its side chain. The proteoliposome transport assay result showed that mutation of Q77 to alanine resulted in a protein with 60% activity compared to WT. Q264 is the only other residue that interacts with Na2 through its side-chain. Q264A expressed well and was monodisperse in FSEC. However, after solubilisation Q264A was not stable and precipitated.

4.3.2.1. Crystallization

The previous vapour diffusion crystallization condition that resulted in crystals of the WT and E260A proteins was tried for the Q77A mutant as well. However, no crystals were obtained, even when carrying out a broad screen, around this condition changing pH and PEG concentration. In addition no good crystals were found using sparse matrix screens. However, crystals were obtained using the LCP method. These crystals were grown at 20°C and reached a maximum size after 2-3 weeks. The best crystals were obtained from the optimized condition, 0.1 M NaCl, 0.1 M MES pH 5.5, 0.1 M $LiSO_4$ and 28% PEG400. (Fig. 4.14.) Although, the crystallization method was different from the WT and E260A crystals, this condition was similar to that of vapour diffusion method. The crystals did not grow bigger than 50 mm.

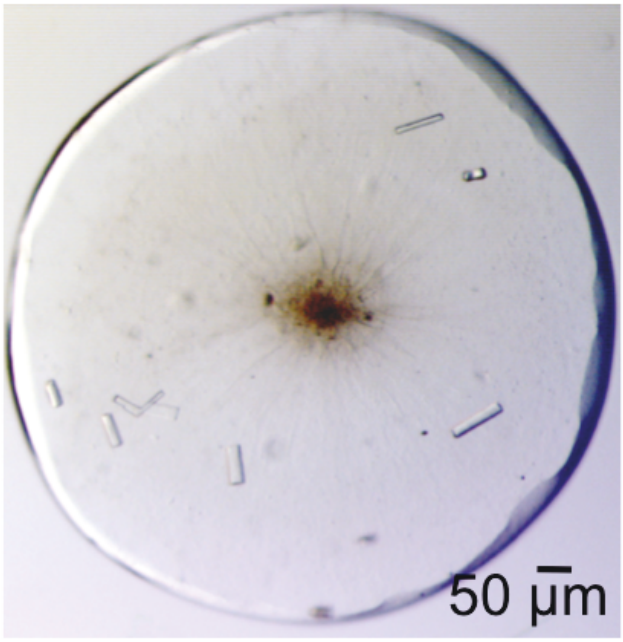


Fig. 4.14. Crystal of $ASBT_{NM}$ Q77A.

Crystals of $ASBT_{NM}$ Q77A from LCP method. The size of the crystals is around 50 µm.

4.3.2.2. Data Collection and Analysis

The crystals were indexed as space group of $P2_1$. To collect a complete data set it was necessary to collect data from three different positions of a single crystal (Fig. 4.15. and Fig. 4.16.) This was done using the microfocus beamline.

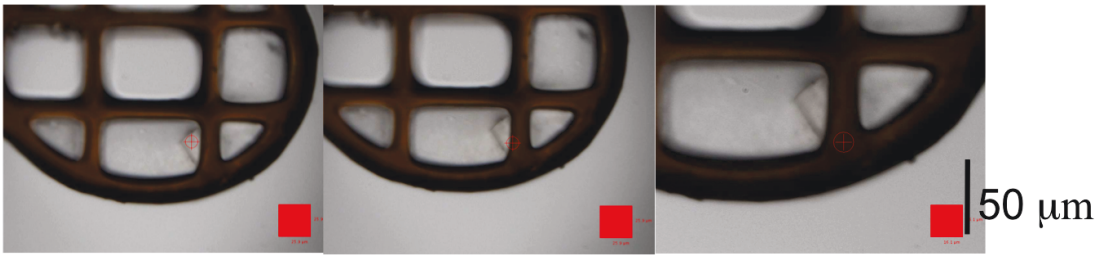


Fig. 4.15. Crystal of $ASBT_{NM}$ Q77A in a loop

A Q77A crystal was fished using a MicroMesh loop and mounted on the microfocus beamline. The three pictures show the different positions of the crystal during the data collection. The red circle indicates the beam position.

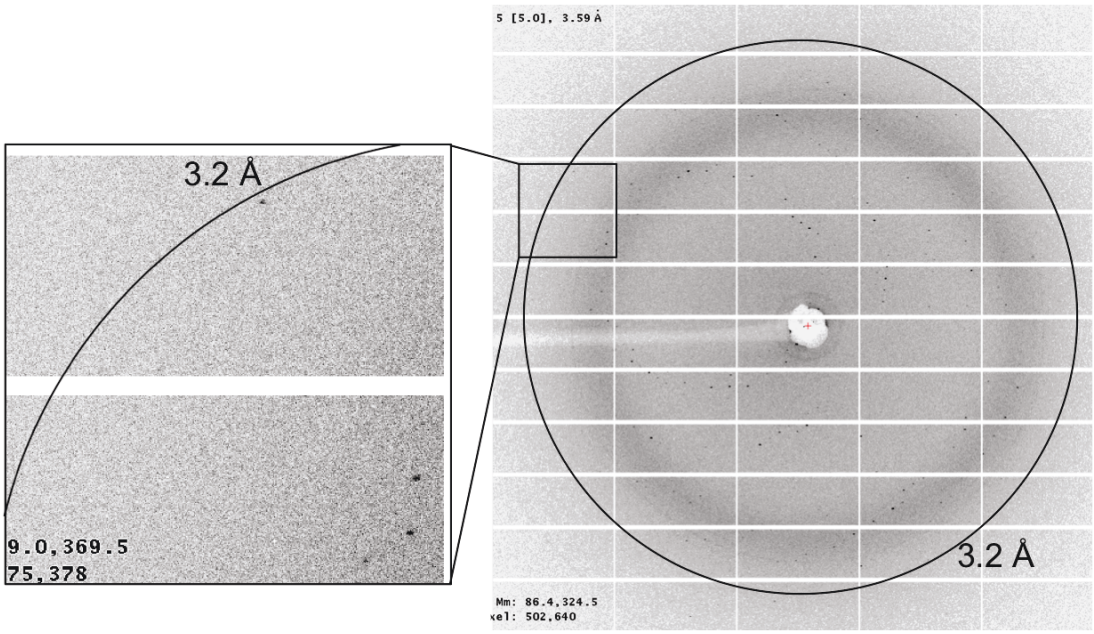


Fig. 4.16. ASBT$_{NM}$ Q77A X-ray diffraction image.

The black circle indicates the diffraction at a resolution of 3.2 Å. The left box shows the spots at the highest resolution.

The resolution was cut at 3.2 Å where the CC_{50} was 0.53. The structure was solved by molecular replacement method using the wild type structure, 3ZUY, as the model. The structure contains 4 molecules in the asymmetric unit with a solvent content of 53%. This is much lower than the wild type crystals solved by vapour diffusion. The final R-value is 24.3 and the R_{free}-value 30.4. RMSD from ideal values were 0.003Å (Bond length) and 0.800° (Bond angle). Other statistics including validation parameter can be seen in the Table. 4.5.

Table. 4.5. $ASBT_{NM}$ Q77A data collection and refinement statistics.

Crystal	**Q77A**
Wavelength (Å)	0.9778
Beamline	I24 / DLS
Oscillation range	0.5 °
Exposure time	0.1 s
Transmission	100%
Beam size	10 mm x 10 mm
Space group	$P12_11$
Resolution (Å)	47.4 - 3.2 (3.4 - 3.2)
CC_{50}	0.99 (0.53)
Cell dimensions (Å)	***a***=85.0, ***b***=88.8, ***c***=96.1
	a=b=90, g=114.4
Number of measured reflections	105782
Number of unique reflections	21255
Completeness (%)	98.4 (98.5)
Redundancy (%)	5.0 (4.9)
$I/\sigma(I)$	6.6 (1.1)
R_{merge} (%)[a]	22.4 (141.8)
Solvent content (%)	53

Refinement	
Resolution (Å)	47.4 – 3.2 (3.3-3.2)
Number of reflections	35669
R-factor (%)	24.3
R-free (%)	30.4
R.m.s.d. from ideal values	
Bond lengths (Å)	0.003
Bond angles (°)	0.80
Ramachandran outliners (%)	0.1
Ramachandran favored (%)	97.9
Rotamer outliners (%)	2.6

Values in parentheses are for the high resolution shells.
[a] $R_{merge} = \Sigma_{hkl} \Sigma_I |I_i(hkl) - \langle I(hkl) \rangle| / \Sigma_{hkl} \Sigma_I I_i(hkl)$, where $I_i(hkl)$ is the intensity of an individual reflection and $\langle I(hkl) \rangle$ is the average intensity.

Details of the refinement are described below. As for the E260A structure the refinement parameters were screened to find the best parameters. 3 cycles of XYZ coordinates refinement was selected as a standard refinement parameter. Among the options tested, Individual B-factors, TLS parameters and Reference model restraints improved the model. The best R-value and R_{free}-value values were obtained when these four parameters were selected together. No improvement could be obtained after 5 cycles. No large-scale conformational change was observed between the WT and the Q77A structure and the Q77A forms an inward facing conformation. In initial maps significant electron-density was not observed in either Na1 or Na2 binding sites. This was then examined more closely. The electron density maps showed clear negative density around Q77 if it was modeled as a glutamine as in the wild type structure rather than the alanine of the mutant. (Fig. 4.17.a.) When Na1 or Na2 were superposed from the 3ZUY structure and mFo-DFc maps were calculated at -3.0 sigma. (Fig. 4.17.b and d) Strong negative electron densities were observed at the Na2 binding site and the broad electron densities were observed at Na1.

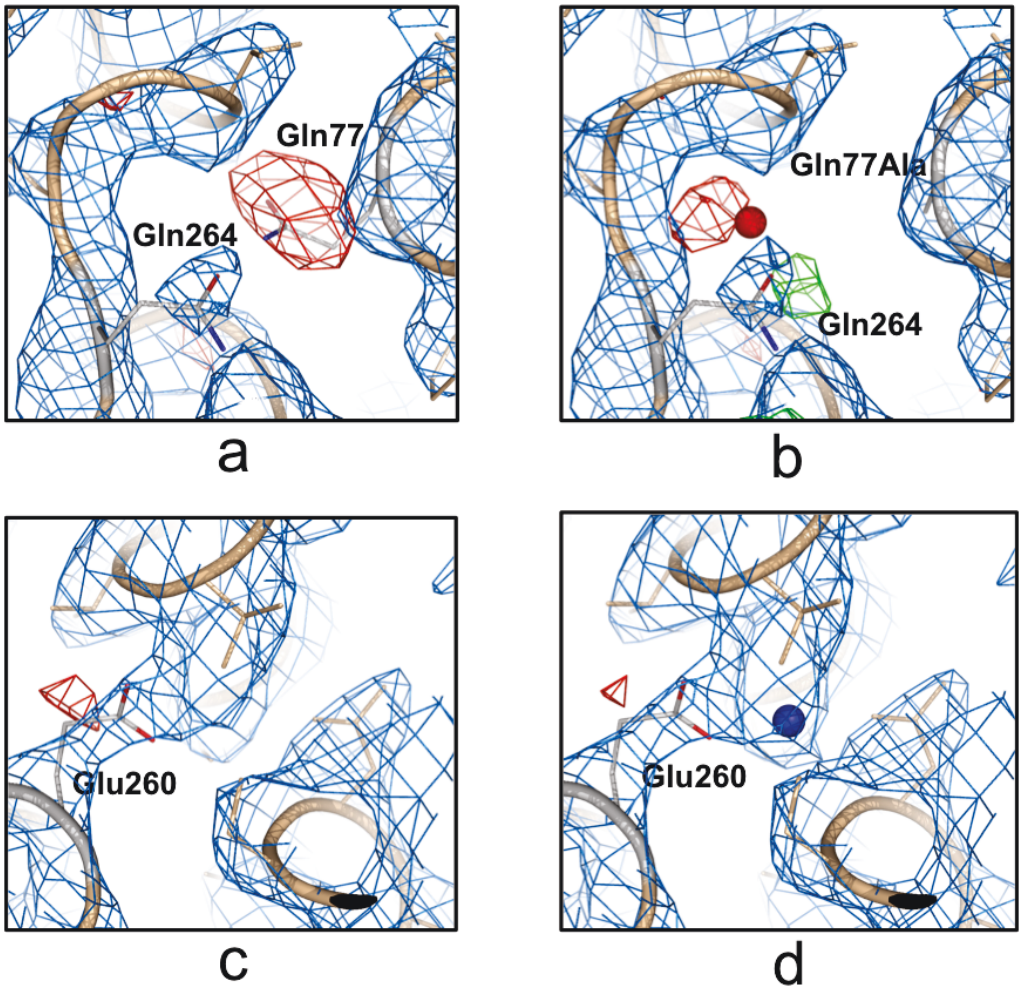


Fig. 4.17. Electron density map of $ASBT_{NM}$ Q77A structure.

2mFo-DFc map was calculated at 1.0 sigma and represented as blue mesh. mFo-DFc map was calculated at -3.0 sigma and represented as red mesh. a). The negative mFo-DFc map can be seen around the side chain of glutamine 77. No significant electron density was observed for Na2. b). Na2 was obtained from superposed 3ZUY that represented negative electron density. c). Na1 binding site of Q77A showed that no significant electron density was observed for Na1. d). Na1 was obtained from superposed 3ZUY that represented the broad electron density.

The electron density of Na1 and Na2 in the WT structure were calculated at the same resolution, 3.2 Å or lower, and compared in the region of the sodium binding sites with the Q77A structure. (Fig. 4.18.) Even at the resolution, electron densities of Na1 and Na2 in wild type were clearly observed (even calculated at 4 Å), whereas in Q77A there was not a significant electron density at Na2 binding site. (Fig. 4.17.)

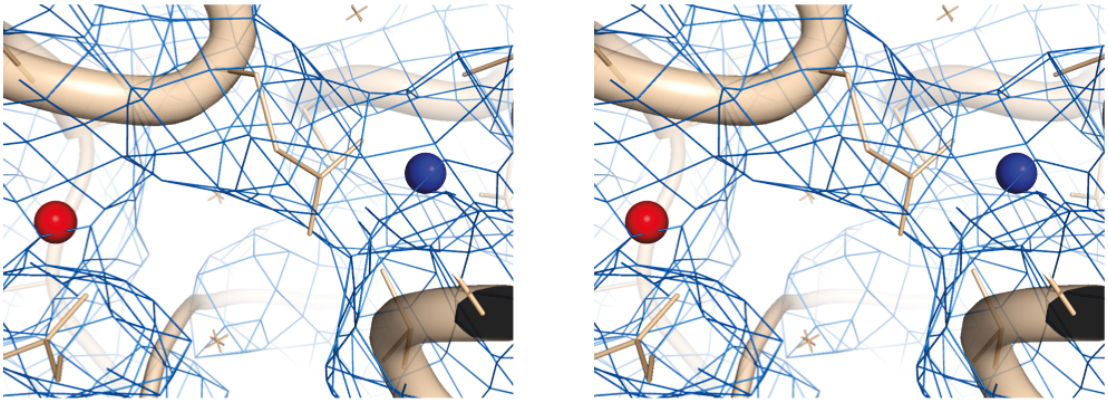


Fig. 4.18. The Na1 and Na2 binding sites of $ASBT_{NM}$ WT X-ray structure and electron densities.

2mFo-DFc maps were calculated a). at 3.2 Å and 2.0 sigma and b). at 4.0 Å and 0.5 sigma. Na1 and Na2 were represented as red and blue spheres respectively. Electron density maps for Na1 and Na2 were observed at both resolutions.

Because the space group of Q77A was different from the other structures, calculation of Fo-Fo maps between WT and Q77A structure factors was not applicable. In this structure, no significant electron density could be observed in either the Na1 or the Na2 binding sites, though some density could be observed in the Na1 binding site. However, still it is possible that sodium ions may be bound in the binding site at lower occupancies and could not be observed due to the low resolution data.

A comparison of $ASBT_{NM}$ WT, 3ZUY, and Q77A structures showed an RMSD between Cα of 0.60. Overall the protein was in the same inward-facing conformation as the wild-type structure but some local changes were observed as described below.

Na2 binding site of $ASBT_{NM}$ Q77A X-ray structure

In the Na2 binding pocket, there are only two amino acid residues, Q77 and Q264 that directly bind to Na2 with their side chain. Though there is no clear conformational change of the main chain, substitution of Q77A or the absence of a sodium ion could affect the local structure around the pocket. (Fig. 4.19.d.) During refinement Gln264 was slightly moved toward the center of the Na2 binding site by around 1.0 Å. However due to the resolution of the Q77A structure, it is impossible to discuss this difference.

Na1 binding site of $ASBT_{NM}$ Q77A X-ray structure

Although the coordinates of all the residues corresponding to Na1 binding were similar to the wild type structure, density for a sodium ion was not clearly observed in the pocket. (Fig. 4.19.b) This may be due to the quality of the data but it could also be possible that the local conformational changes around the Na2 binding site caused by the Q77A substitution would affect the neighbouring Na1 binding site as well. This indirect conformational change might reduce the binding affinity of Na1.

Substrate binding site of $ASBT_{NM}$ Q77A X-ray structure

While it was necessary to add taurocholic acid to the protein to obtain crystals of $ASBT_{NM}$ using vapour diffusion the crystal structure of Q77A was solved in the absence of taurocholic acid. Overall, between WT and Q77A no movements of the back-bone and side-chain of each residue were observed in the inward facing open pocket. (Fig. 4.19.c.) The conformation of the residues that bind to taurocholic acid in the WT structure do not change in the Q77A structure including T112, N265, H294 and N195.

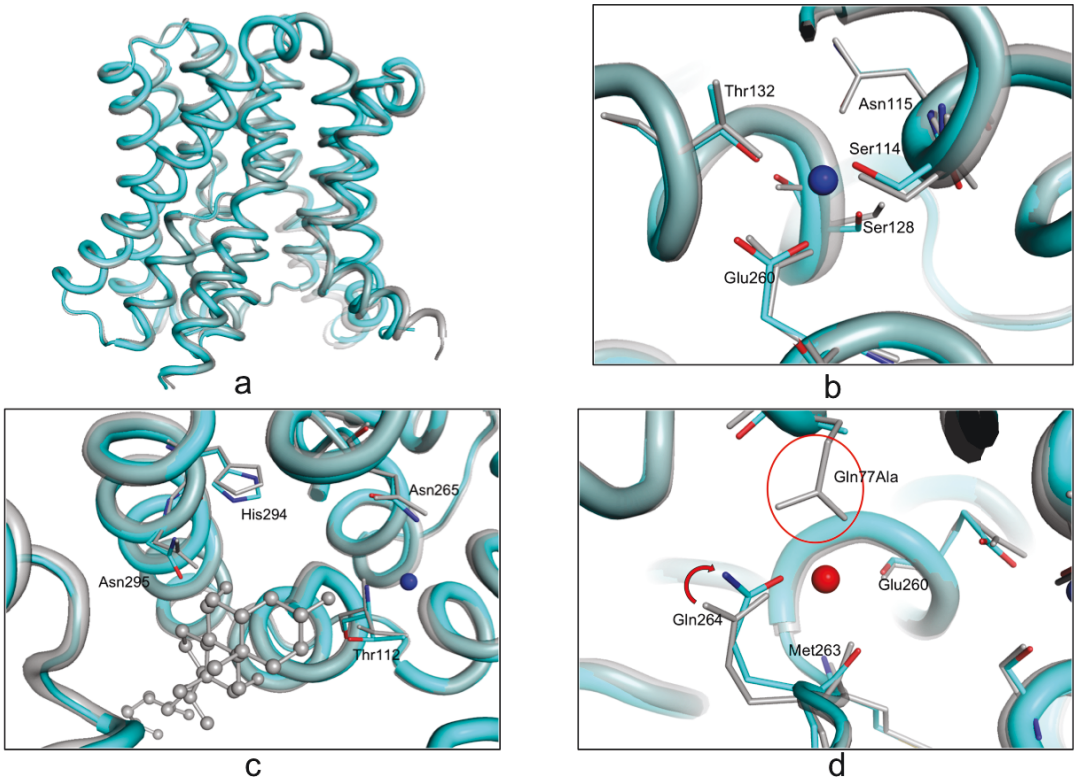


Fig. 4.19. Superposition of $ASBT_{NM}$ WT (3ZUY) and Q77A structure.

WT is shown as a grey ribbon and Q77A as a light blue ribbon. Na1 from WT is shown as a blue sphere and Na2 from WT is shown as a red sphere. a). Overview of superposed structures. b). Superposed Na1 binding site. c). Superposed taurocholic acid binding site. d). Superposed Na2 binding site. Red circle indicated the side chain of Gln77 of WT structure. Gln264 is in a slightly different position in the two structures.

The space group of the Q77A crystal is different from the other $ASBT_{NM}$ structures, and the crystal packing is completely changed. Having two differently packing crystal structures can help us understand where the flexible regions of the protein are. In the WT and E260A structures a kink of TM1 was observed between Thr14 and Pro15 and the phosphate tail of taurocholic acid interacted with Lys13. The suspicion was that the kink in the helix was due to taurocholic acid binding. In the Q77A structure this kink still exists but the N-terminal part of the helix was tilted slightly from the WT structure toward the direction of the inward open pocket. (Fig. 4.20.) This suggests that the kink is not caused by either crystallisation in detergent solution or the addition of taurocholic acid. In addition to the TM1, part of TM6 and TM7 (obvious differences are observed between Pro 173 and Leu192) slightly moved to be off from the core domain with the distance of 2.0 Å at the maximum.

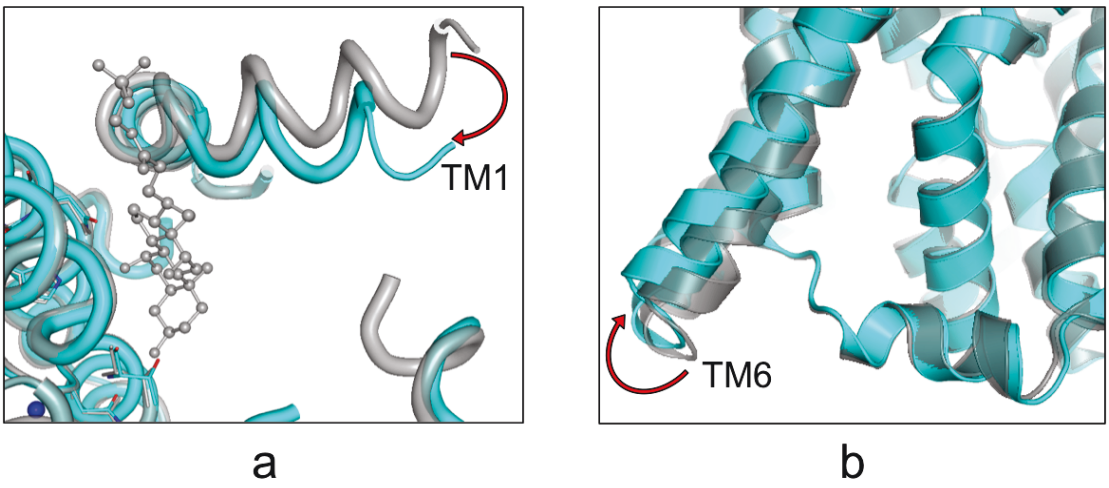


Fig. 4.20. Superposition of WT (3ZUY) and Q77A structures at TM1, TM6 and TM7.

WT is shown as a grey ribbon and Q77A as a light blue ribbon. a. TM1 of Q77A tilted to inward facing pocket. b. TM6 and TM7 of Q77A moved away from the core domain.

4.2.3. WT in complex with rhodamine

In addition to the two mutant structures, WT crystallization was tried in order to solve the complex structure with another ligand than taurocholic acid. Rhodamine was selected as a candidate ligand to trap the WT in the outward facing conformation. As the whole cell binding assay result showed it could bind to $ASBT_{NM}$ but not be transported, it was assumed that rhodamine could bind to the extracellular side of $ASBT_{NM}$.

4.2.3.1. Crystallization

Crystals were obtained from the vapour diffusion method using similar conditions for the previously solved WT structure. The crystals have the same pink colour of rhodamine. (Fig. 4.21.)

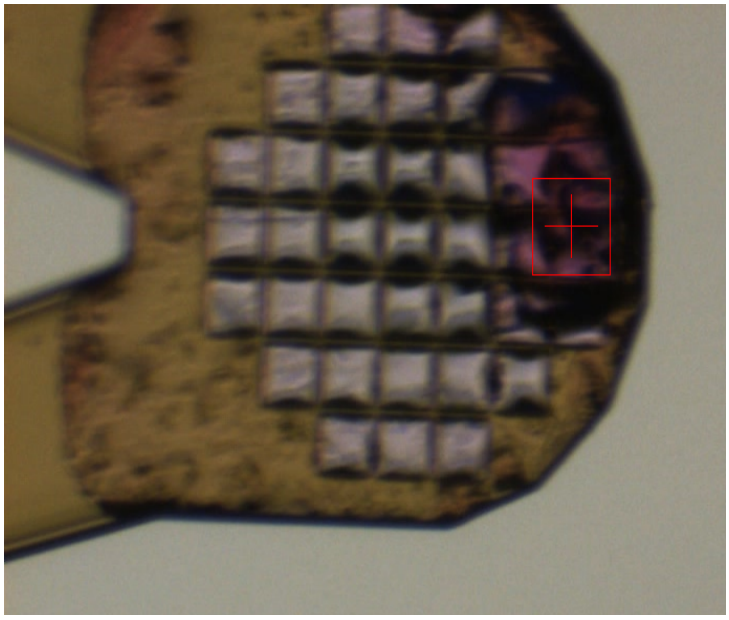


Fig. 4.21. Crystal of $ASBT_{NM}$ WT in the presence of rhodamine.

The pink rhodamine crystal mounted on the MicroMesh loop. The red square is 50 mm x 50 mm.

4.3.3.2. Data Collection and Analysis

An X-ray diffraction data set was collected at 3.5 Å. (Fig. 4.22.) The crystals had the same space group and similar cell dimensions as the wild type $ASBT_{NM}$ structure in complex with taurocholic acid. (3ZUY: $P4_122$, a=b=73.4, c=162.5) The refinement protocol was similar to E260A giving a final R-value of 28.3% and R_{free}-value of 33.1% at 3.6Å. The RMSD from ideal values were 0.04Å (Bond length) and 1.128° (Bond angle). There was no outlier in a Ramachandran plot and the number of residues in the favoured region was 99.7%. The number of rotamer outliers was 1.7%. The electron density showed that no large scale conformations had taken place relative to the 3ZUY structure. (Fig. 4.22.) No clear density was observed in the binding site. However, at this low resolution we cannot rule out that some rhodamine has weakly bound.

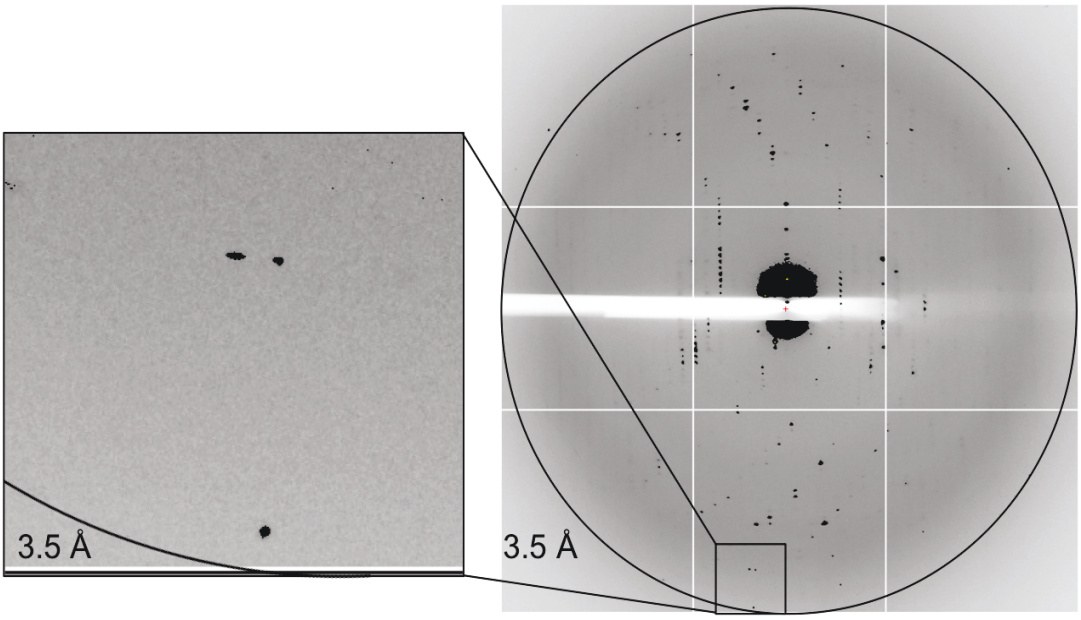


Fig. 4.22. $ASBT_{NM}$ WT in complex with rhodamine X-ray diffraction.

The black circle indicates the diffraction limit at a resolution of 3.5 Å. The left box shows the spots at the highest resolution.

Table. 4.6. $ASBT_{NM}$ WT data collection and refinement statistics.

Crystal	**WT-Rhodamine**
Wavelength (Å)	0.9795
Beamline	IO4 / DLS
Oscillation range	0.5 °
Exposure time	2.0 s
Transmission	100%
Beam size	85 mm x 85 mm
Space group	$P4_122$
Resolution (Å)	30.9 - 3.7 (3.9 - 3.7)
CC_{50}	0.99 (0.85)
Cell dimensions (Å)	***a***=***b***=74.82, ***c***=162.92
	α=β=γ=90°
Number of measured reflections	26677
Number of unique reflections	5060
Completeness (%)	94.1 (82.2)
Redundancy (%)	5.3 (5.1)
$I/\sigma(I)$	7.5 (1.8)
R_{merge} (%)[a]	10.2 (73.4)

Refinement	
Resolution (Å)	30.8 – 3.7 (3.9-3.7)
Number of reflections	5036
R-factor (%)	28.31
R-free (%)	33.07
R.m.s.d. from ideal values	
Bond lengths (Å)	0.004
Bond angles (°)	1.13
Ramachandran outliners (%)	0.0
Ramachandran favored (%)	99.7
Rotamer outliners (%)	1.7

Values in parentheses are for the high resolution shells.
[a] $R_{merge} = \Sigma_{hkl} \Sigma_I |I_i(hkl)-\langle I(hkl)\rangle|/\Sigma_{hkl} \Sigma_I I_i(hkl)$, where $I_i(hkl)$ is the intensity of an individual reflection and $\langle I(hkl)\rangle$ is the average intensity.

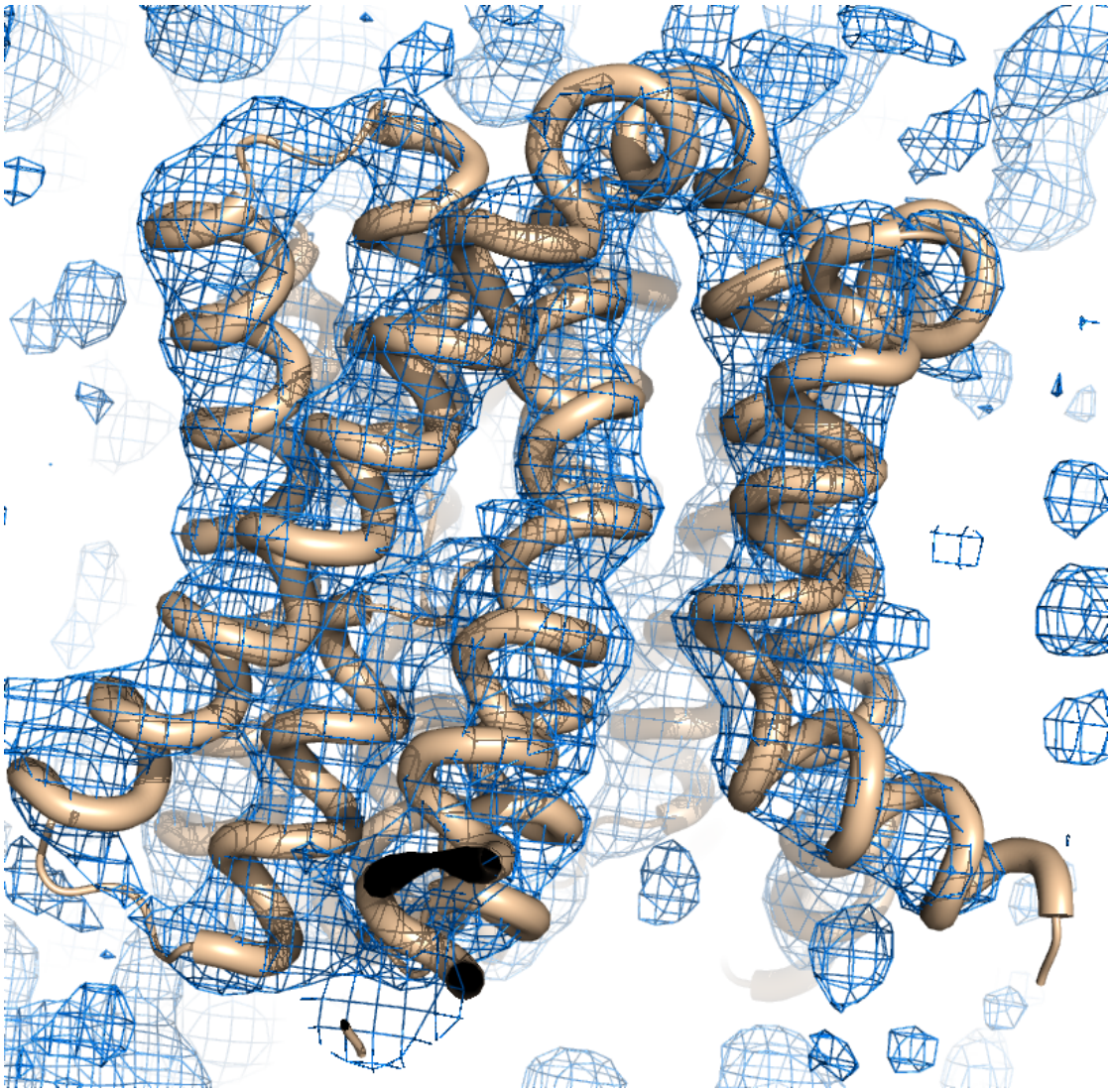


Fig. 4.23. Overview of $ASBT_{NM}$ WT structure and electron density map. $ASBT_{NM}$ was represented as ribbon style coloured with wheat. The 2mFo-DFc map was calculated at 1.0 sigma and shown as blue mesh. No significant electron density was observed in the binding pocket.

4.3.4. Homology modeling of human ASBT

The sequence identity of $ASBT_{NM}$ to human ASBT is 26% and the residues forming the Na1 and Na2 binding sites are highly conserved. From the WT $ASBT_{NM}$ structure, 3ZUY, a homology model of human ASBT was prepared. (Fig. 4.24) The C-terminal amino acid residues of human ASBT, 313-348, were omitted from the model, which acts as a sorting signal for apical trafficking in rat (Sun *et al.* 2003). It is noteworthy that human ASBT has an extracellular N-terminus and a cytoplasmic C-terminus (Hagenbuch and Meier 1994) and 9 transmembrane helices. Thus, TM1 in this homology model was actually exposed to the extracellular side. Both the Na1 binding site (S112, N114, S126, T130 and E261) and the Na2 binding site (Q75 and Q265) were formed as for WT $ASBT_{NM}$. On the contrary to the conserved Na1 and Na2 binding sites, the inward facing pocket consists of different residues in the two species as described below. In WT $ASBT_{NM}$, taurocholic acid bound to N295, possibly with Thr112 and through a water molecule to H294, followed by hydrophobic residues in the inward facing pocket. In human ASBT H294 is replaced by a glutamine, which is a relatively conservative change. Q297, on the other hand, is a leucine (L298). A leucine at this position is conserved in human ASBT and other members of the SLC10 family (NTCP and SOAT). (Fig. 4.25.)

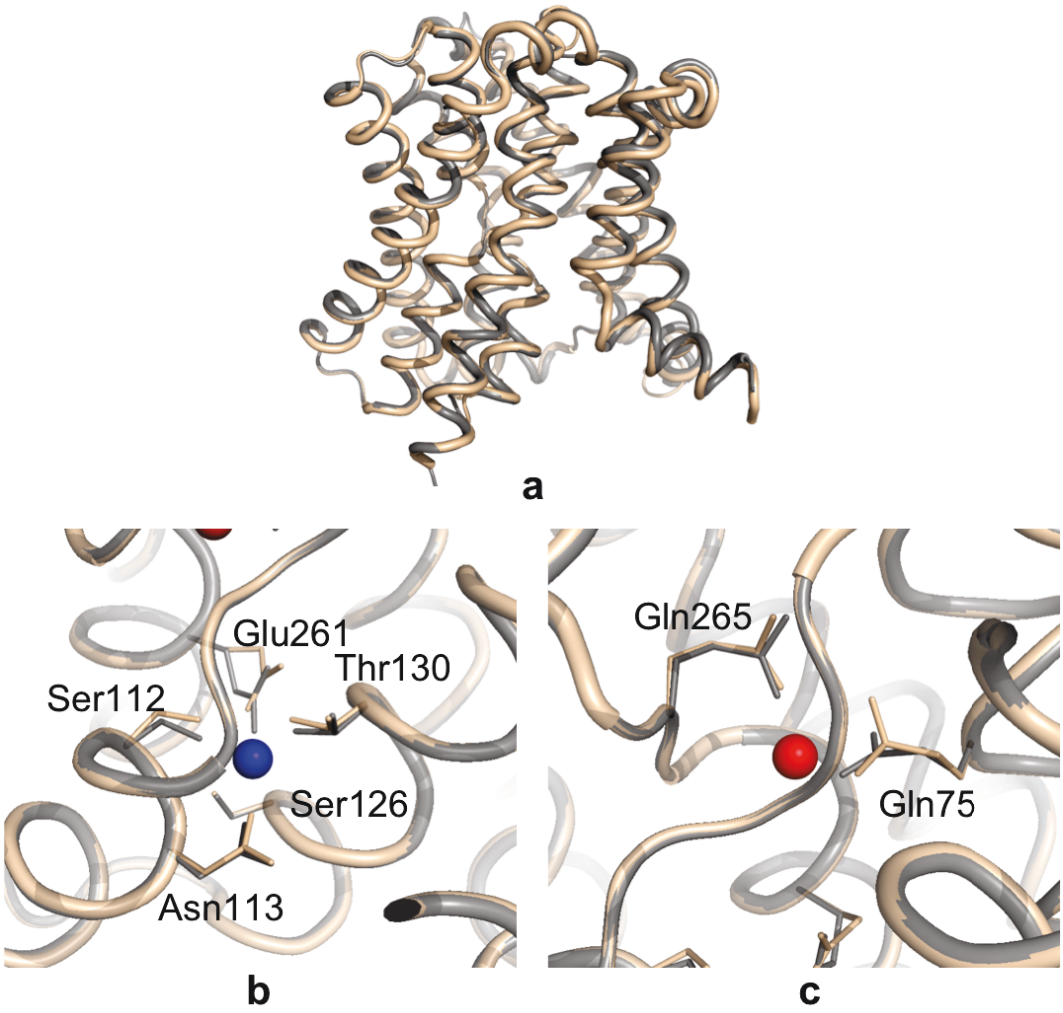


Fig. 4.24. Superposed structures of human ASBT homology model and $ASBT_{NM}$.

a). Overview of superposed structures. Grey and wheat ribbons represented human ASBT model and $ASBT_{NM}$ respectively. b). Na1 binding sites. Na1 was shown as blue sphere from $ASBT_{NM}$ structure. c). Na2 binding sites. Na2 was shown as red sphere from $ASBT_{NM}$ structure.

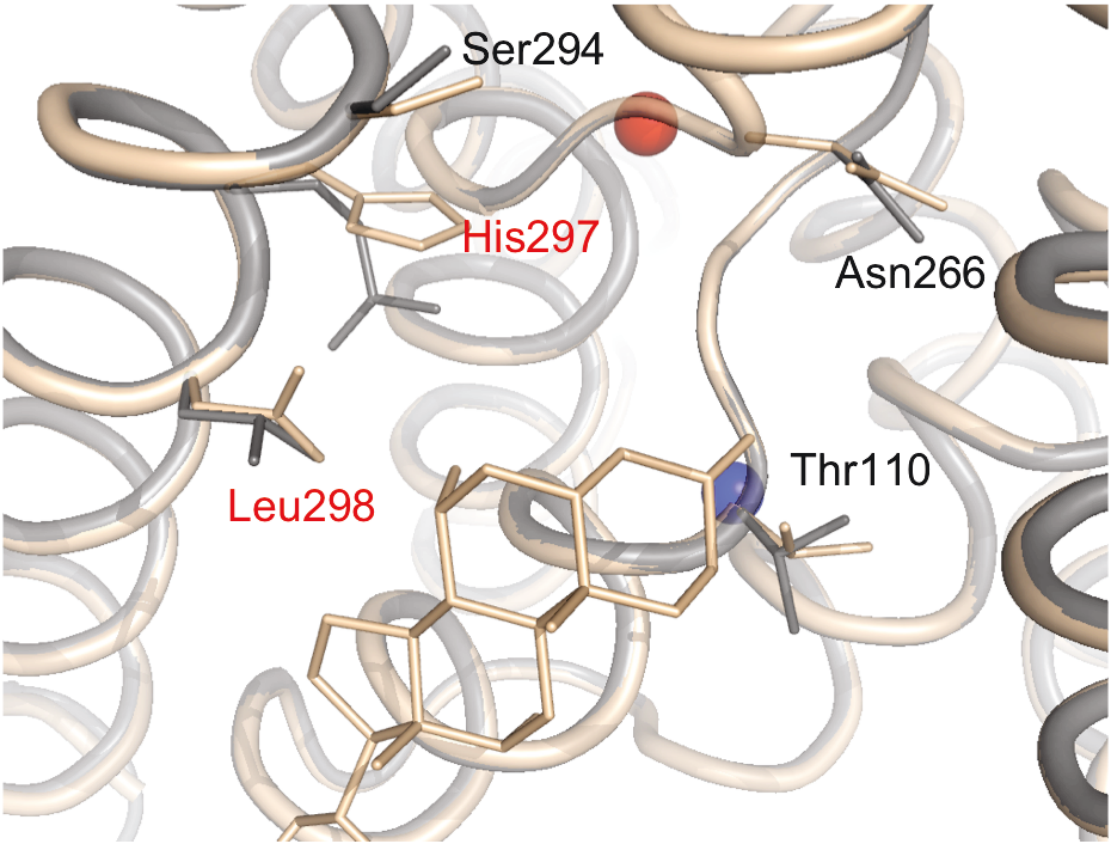


Fig. 4.25. Superposed structures of human ASBT homology model and $ASBT_{NM}$ at taurocholic acid binding pocket.

Grey and wheat ribbons represented human ASBT model and $ASBT_{NM}$ respectively. His297 and Leu298 of human ASBT were different from $ASBT_{NM}$ and highlighted as red characters.

4.4. Biophysical methods

Two X-ray crystal structures of $ASBT_{NM}$ mutants were solved giving insight into how the sodium binding sites were maintained by the residues forming the respective sites. The contribution of each mutated residues was examined by the proteoliposome transport assay. In addition to these data, the detailed quantitative parameters of binding reaction would be important to characterise $ASBT_{NM}$ function.

Because of the detergent properties of bile acids, functional analysis of the $ASBT_{NM}$ and bile acid reaction is extremely difficult and demands careful experimental approaches. The critical micellar concentrations of bile acids are lower than other detergents with around 3 - 10 mM. Thus, two physical events happen at the same time when bile acids are added to $ASBT_{NM}$, binding and stabilization by a micellar effect. To measure the functional activity a detergent molecule is not suitable in the assay system except as a substrate molecule with a concentration at lower than the CMC value.

4.4.1. Circular dichroism (CD)

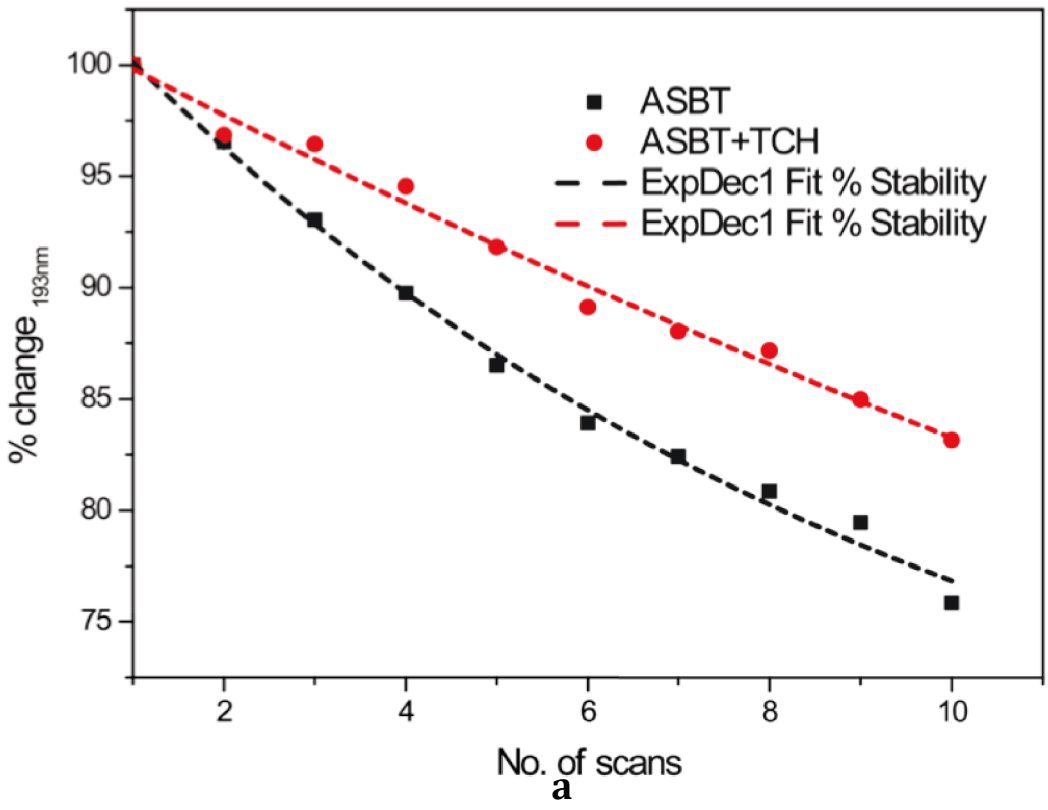
CD spectroscopy was performed to evaluate the binding affinity of taurocholic acid to $ASBT_{NM}$ in detergent solution. Two different types of experiments were tried as described below.

Near UV (250-330nm) region

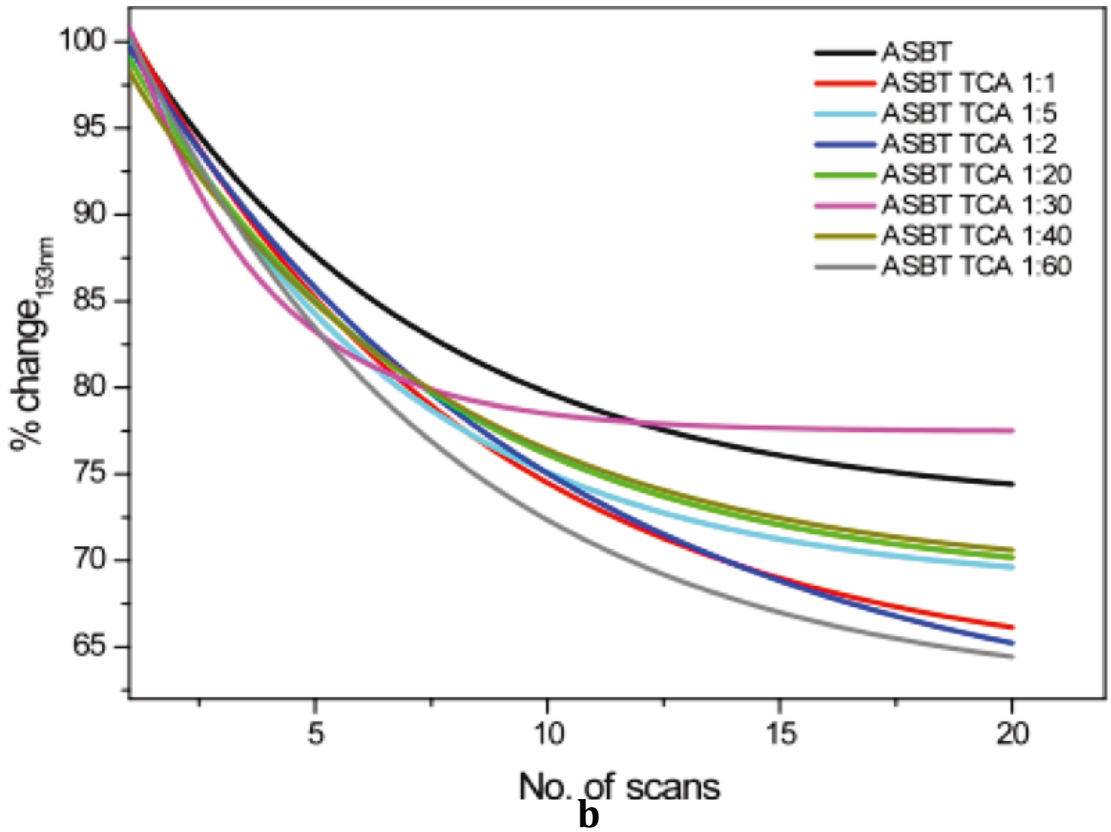
At the near UV region, it is possible to monitor the tertiary structure of aromatic residues. In $ASBT_{NM}$ a phenylalanine, (Phe 15), is located 3.4 Å from the taurocholic acid. It was thought that if the rotamer of Phe15 was changed by binding taurocholic acid, differences of signals could be detected in the near UV region and the binding affinity could be obtained by titrating the concentration of taurocholic acids to $ASBT_{NM}$. Unfortunately the spectra from $ASBT_{NM}$ were unaltered when taurocholic acid was added to the solution even at 200 μM. As it was not clear whether this is due to the lack of interaction between Phe15 and taurocholic acid or due to the low signal from the phenylalanine, Phe15 was substituted with a tryptophan. This resulted in noisy spectra, which were difficult to interpret. After this experiment, the structure of Q77A was solved without taurocholic acid. In the structure, the conformation of Phe15 was the same as that of the previously solved structure so it is perhaps unsurprising that no signal was observed.

Far UV region (170-260 nm)

As a second step it was decided to use the Far UV region. This region of the spectrum gives information about the secondary structure of the protein. It is possible to determine the affinity of taurocholic acid to $ASBT_{NM}$ by titrating different concentrations of taurocholic acid and measure the stability of the protein as binding of taurocholic acid would help keep $ASBT_{NM}$ folded under the experiment. Differences in the stability were measured in the presence of taurocholic acid. As shown in Fig. 4.26.a, the effect of taurocholic acid on the stability of $ASBT_{NM}$ was apparent from the spectra. This gave conflicting results. From the result of the first measurement, compared to no taurocholic acid condition, the spectrum in the presence of 20 μM taurocholic acid showed $ASBT_{NM}$ to be more stable. When the experiment was carried out with various molar ratios of taurocholic acid to determine the K_D value. $ASBT_{NM}$ was destabilized in most of the conditions. (Fig. 4.26.b.) Notably, the stabilities were not proportional to the concentration of taurocholic acid. Furthermore, reproducibility of the measurement with the fixed taurocholic acid concentration was not good either. The detergent character of taurocholic acid could affect this result as taurocholic acid can be incorporated into the DDM micelle in the buffer (Luckey, 2008) and affect the stability of the protein.


ASBT
ASBT+TCH
ExpDec1 Fit % Stability
ExpDec1 Fit % Stability
% change 193nm
No. of scans
100
95
90
85
80
75
2
4
6
8
10

a


ASBT
ASBT TCA 1:1
ASBT TCA 1:5
ASBT TCA 1:2
ASBT TCA 1:20
ASBT TCA 1:30
ASBT TCA 1:40
ASBT TCA 1:60
% change 193nm
No. of scans
100
95
90
85
80
75
70
65
5
10
15
20

b

Fig. 4.26. CD spectroscopy result in the far UV region.

CD data at 193 nm were extracted from 10 repeated scans and converted to the relative values against the first scan. Percentages were plotted versus the number of repeated scans. Decline of the curves represent the unfolding of $ASBT_{NM}$. a) Black square shows $ASBT_{NM}$ and red sphere shows $ASBT_{NM}$ in the presence of taurocholic acid at a 1:5 molor ratio. b). In the presence of various taurocholic acids molar ratios to $ASBT_{NM}$. (red=1:1; cyan=1:5, blue=1:2; green=1:20; pink=1:30; olive=1:40; and grey=1:60)

In summary SRCD spectroscopy detects differences of $ASBT_{NM}$ stability in the presence of taurocholic acid. However the experimental conditions to investigate the effect of taurocholic acid on $ASBT_{NM}$ could not be optimized. This may be due to several factors that could not be controlled including detergent concentration in the buffer and detergent aspect of taurocholic acid rather than as a ligand of $ASBT_{NM}$.

4.4.2. Isothermal Titration Calorimetry (ITC)

From the CD spectroscopy result it seemed difficult to obtain the binding affinity of taurocholic acids by measuring the stability of $ASBT_{NM}$. Instead, ITC directly measures the reaction of the binding by detecting the heat changes in the system. Thus, ITC was performed to observe the binding reaction of taurocholic acid.

To determine the K_D value accurately from ITC, plotting a curve through the integrated heat changes of each titration against the molar ratio should give a sigmoidal line. The dilution factor of taurocholic acid was small enough that it did not affect the heat from the reaction between $ASBT_{NM}$ and taurocholic acid binding. (Fig. 4.27.) The reaction stoichiometry and the K_D are obtained from the centre of the isotherm. Once the ligand molecules in the ITC cell reach equilibrium, the following heat changes gradually decreased as the protein gets saturated. As shown in the ITC result the heat change did not reach saturation even when the molar ratio was 50. (Fig. 4.28.)

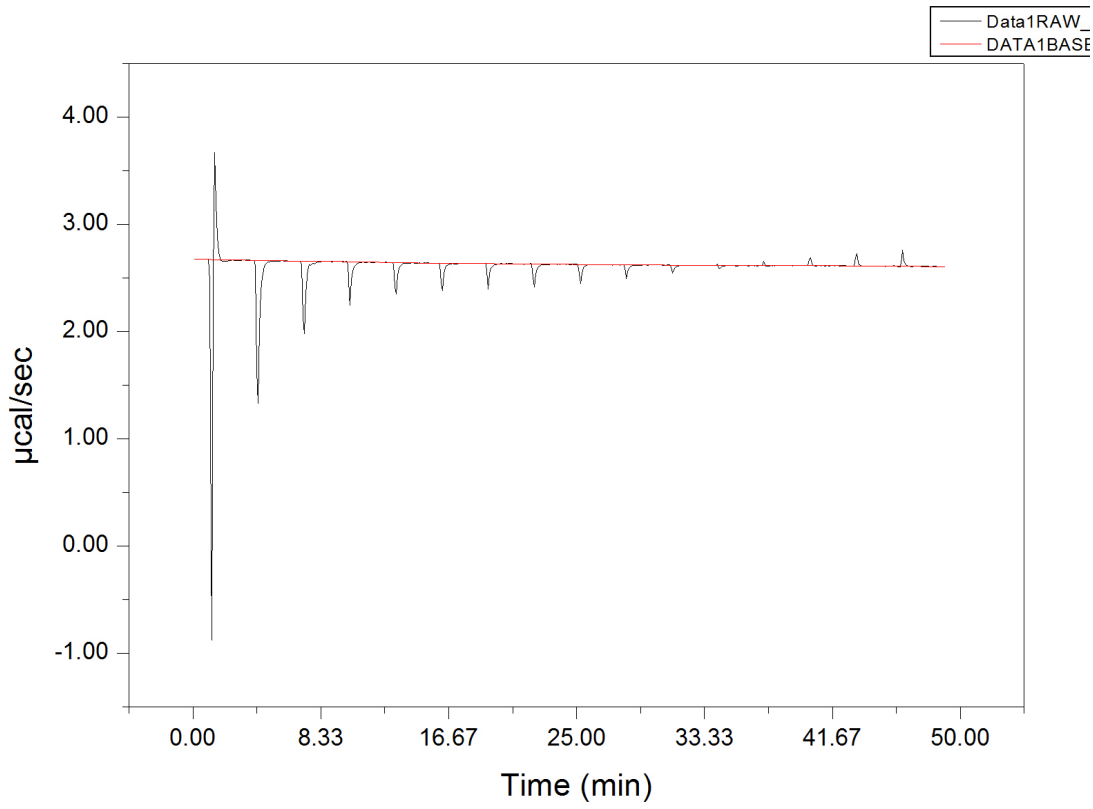


Fig. 4.27. Result of ITC dataset of the baseline.

Heat change versus time titration curve. Each peak represents an injection of taurocholic acid into the sample cells filled with the ITC buffer. Since the initial titration often give a noise signal, the initial peak was not used for the subtraction.

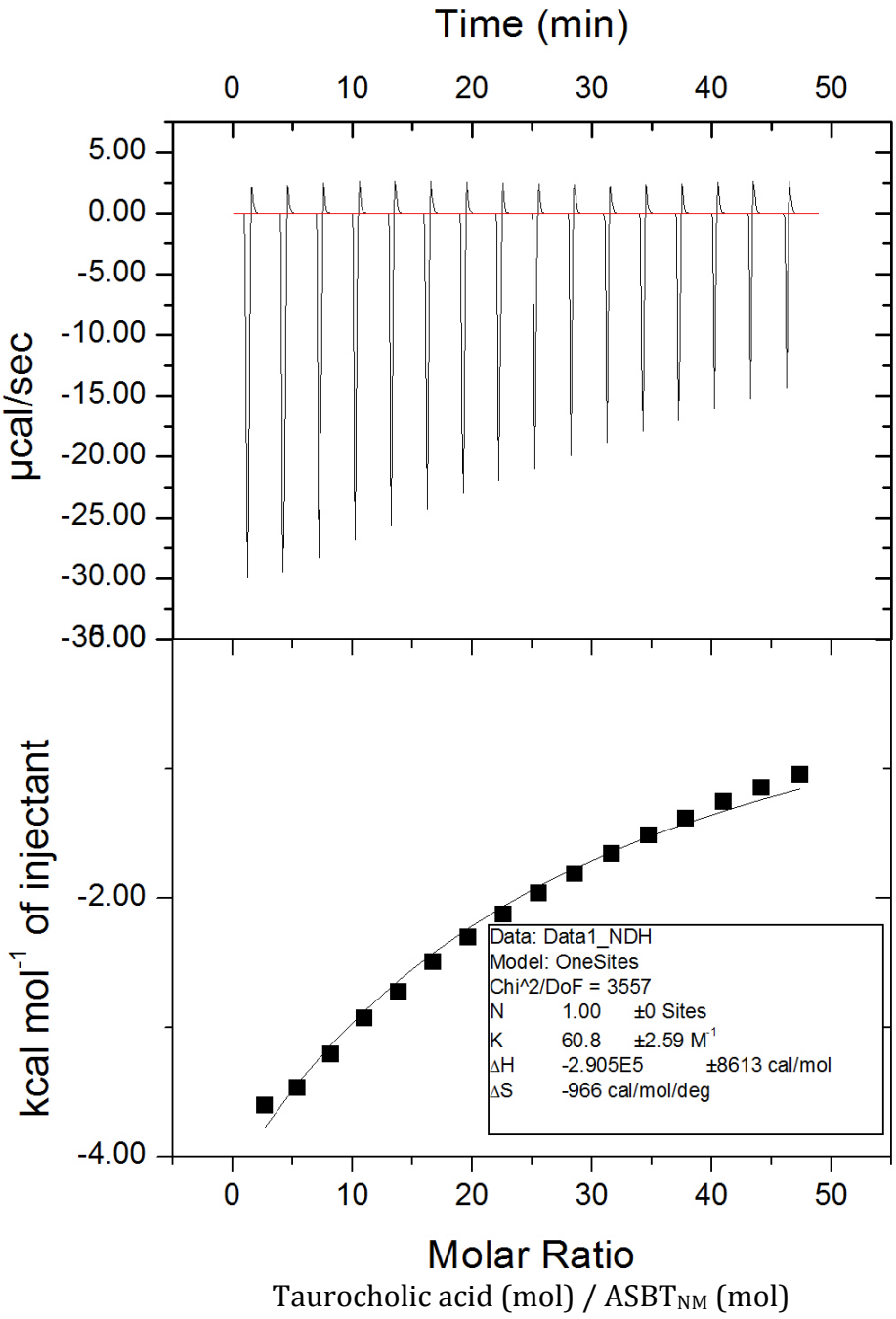


Fig. 4.28. Result of ITC dataset.

Top). Heat change versus time titration curve. Each peak represents an injection of taurocholic acid into the sample cells filled with $ASBT_{NM}$. The heat changes of the taurocholic acid dilution were subtracted. Bottom). Integrated heat changes for each injection versus molecular ratio of taurocholic acid and $ASBT_{NM}$ in the cell.

From this result it is likely that taurocholic acid bound to $ASBT_{NM}$ in detergent buffer. However, the titration curve did not fit to the expected bile acid binding affinity deduced from the transport assays. It is possible that the experimental environment might interfere the measurement of binding reaction, for example, the detergent micelle, sample cells and stirring by syringe unit.

4.4.3. Microscale Thermophoresis (MST)

The MST technique was demonstrated at RCaH. During this demonstration we measured the affinity of $ASBT_{NM}$ binding to taurocholate. The K_D was estimated to be 31 μM, which is consistent with the expected K_D from transport assays. (Fig. 4.29.) Further experiments were performed at Imperial College London. The machine used at RCaH monitored protein mobility by measuring intrinsic tryptophan fluorescence. On the other hand, the machine at Imperial College London measured GFP fluorescence rather than intrinsic fluorescence and required the protein to be conjugated to GFP.

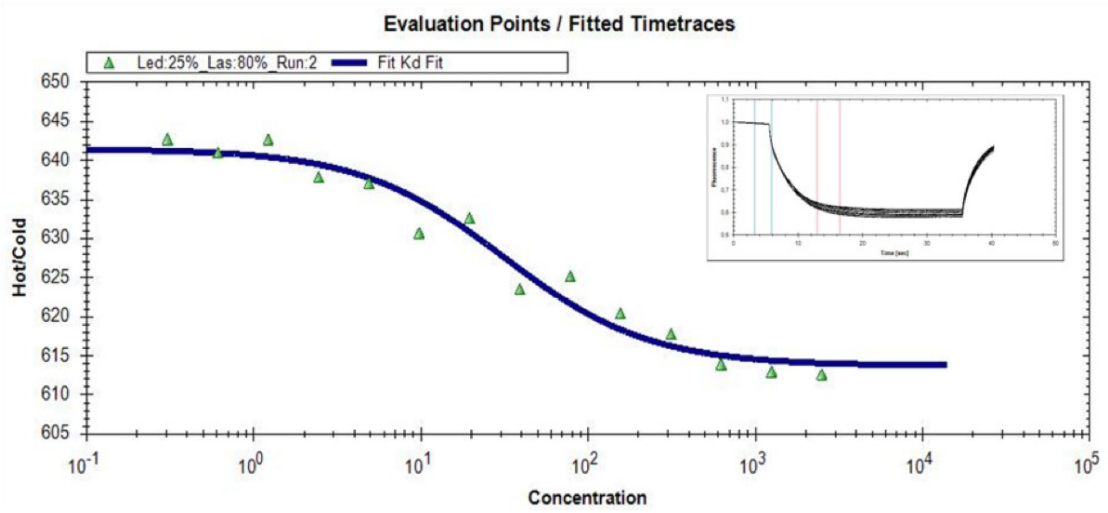


Fig. 4.29. Result of MST data

MST result from the demonstration at RCaH. In the experiment $ASBT_{NM}$ was 500 nM, while taurocholic acid was titrated between 0.3 μM and 2.5 mM. Sigmoid plotting curve was plotted against the concentrations of taurocholic acid.

However, due to the limited access to the equipment and the lack of experience of use of this newly developed machine, no good results were obtained. The preliminary results of using the MST at RCaH suggest that it could be a useful technique for measuring the binding of substrates to $ASBT_{NM}$ in the future.

CHAPTER 5

Discussion

5. Discussion

5.1. Relationship between the structures and the function of $ASBT_{NM}$

In order to understand better the mechanism of taurocholic acid re-absorption by ASBT in the small intestine, functional and structural studies were carried out in this thesis. X-ray crystallography requires large amounts of purified protein, which has to be stable and homogeneous. Since, mammalian membrane proteins are poorly expressed heterologously, bacterial homologues are often used (Drew *et al.* 2006). The work in this thesis focused on a homologue of ASBT from *Neisseria meningitides* ($ASBT_{NM}$). To interpret the data from the transport assays of the mutants it is desirable to see how the mutations affect the structure of the protein. The X-ray crystal structures of the mutants E260A and Q77A were solved where the mutated residues are in the Na1 and the Na2 binding sites respectively. In human ASBT, the residues corresponding to E260 and Q77 in $ASBT_{NM}$ are crucial for both taurocholic acid and sodium transport (Sun *et al.* 2006; Banerjee *et al.* 2008; Sabit *et al.* 2013). The E260A structure shows that Na1 is not present in the pocket or at least the occupancy is much lower than for the WT protein. No difference is observed at the Na2 binding site. For the Q77A mutation the electron density in the both sodium ion binding sites is less than for WT. Neither of these mutations causes large changes to the protein structure and both structures still show the inward-facing state.

From the work described in the results the most reliable data to measure transport activity of mutants of $ASBT_{NM}$ was using proteoliposomes and a radiolabelled substrate. As the RCaH had no capabilities for carrying out radioactive measurements this assay was carried out in Sweden. Although, not all the mutants were repeated with different batches of purified samples, the structural and proteoliposome assay data are found to be correlated each other as described in below.

Mutations of residues forming the Na1 binding site

The results from the proteoliposome transport assay showed that E260A had the lowest transport activity of all the five alanine mutants of the residues forming the Na1 binding site. This result coincides with the fact that E260 is the only charged residue in the Na1 binding site. (Fig. 5.1.) The X-ray crystal structure of E260A revealed that sodium ion was not present in the Na1 binding site. These results suggest that E260 is necessary for the binding of Na1 and that Na1 is important for activity. Compared to E260A, E260L showed significantly higher transport activity, around 80% of WT. The purpose of this mutant was to block sodium ions binding at Na1 by occupying the space with a bulky leucine residue rather than alanine. Thus, it was expected that lower activity be obtained than with the other mutants at this site. It is possible that under the conditions of the assay the leucine allows the protein to take a conformation that is favourable for activity, though in the cell environment lack of sodium sensitivity may be detrimental. It is also possible that this measurement was an error. Although it was repeated twice this was with the same batch of proteoliposomes.

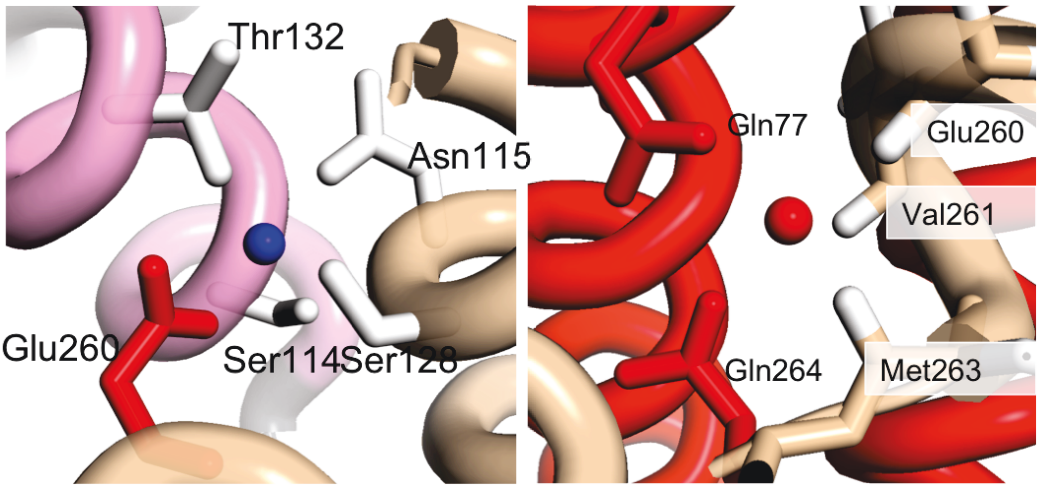


Fig. 5.1. Na1 and Na2 binding sites of $ASBT_{NM}$

Left). The side chains of Ser114, Asn115, Ser128, Thr132 and Glu260 interact with Na1. The backbone of Ser128 interacts with Na1. Glu260 is colored as red to represent the charged residue and the other residues are colored as white to represent no charged residues. Right). The side chains of Gln77 and Gln264 interact with Na2. The backbones of Val261, Glu260 and Met263 interact with Na2. Gln77 and Gln264 are colored as red to represent the charged residue and the other residues are colored as white to represent no charged residues.

Mutations of residues forming the Na2 binding site

From the proteoliposome transport assay, both Q77A and Q264A showed significantly lower transport activities compared to WT, around 60% and 40%. When these two residues were both mutated to alanine, transport activity was completely lost. In the X-ray crystal structure of Q77A, electron density for sodium ions was not clearly observed at either the Na1 or the Na2 binding sites though there did appear to be density at both sites. The results indicate that substitution of Q77 might not result in complete loss of binding of Na2. Even without Q77 present, the other residues (Q264 and backbones of Met263, Val261 and Glu260) could keep the sodium ion in the binding site with a decreased affinity. (Fig. 5.1.) Also it is possible that the electron density in the binding site could come from water molecules binding with weak affinities. On the other hand, Q77 and the other residues could also support the transport activity of Q264A. As shown in the transport assay, double mutation of these residues resulted in loss of activity. Thus, at least one of Q77 and Q264 is necessary for transport. In the same way as for E260L, Q77L was prepared to see whether this would block the sodium ion from binding at Na2 or not. The result shows that Q77L has significantly lower activity than Q77A. This result suggests that the substitution of Q77 to leucine rather than alanine would not only decrease the affinity of Na2 but also prevent it binding. On the other hand, the aim of the Q77K mutant was to replace Na2 with a positively charged residue. In the sodium proton antiporters, which are structurally homologous to $ASBT_{NM}$ a lysine is situated at the same place as the sodium ion (Lee *et al.* 2013, Fig, 5.2.). In the transport assay this mutant showed around half the activity of WT, even lower than Q77A. Although this result supports the importance of Na2, further experiments are required to confirm whether Q77K could actually mimic the sodium ion in the binding site or not.

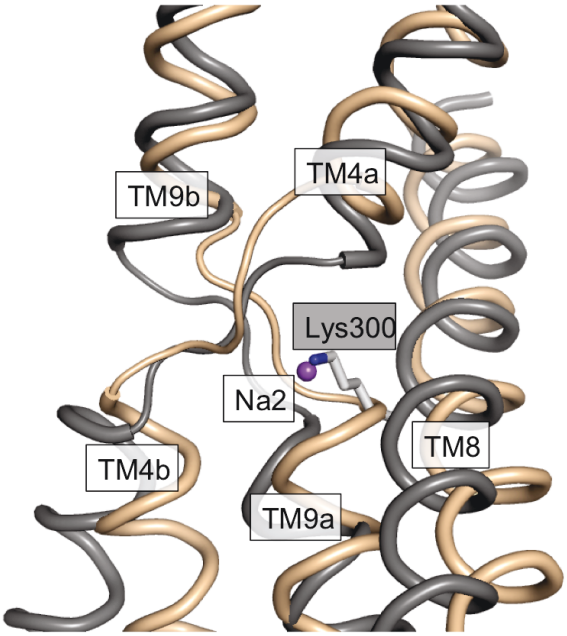


Fig. 5.2. Superposed Na2 binding site of $ASBT_{NM}$ to NhaA.

Structural comparison of Na2 of $ASBT_{NM}$ and Lys300 of NhaA. Grey and wheat ribbons represented NhaA and $ASBT_{NM}$ respectively. The Na2 in ASBTNM is depicted as purple sphere and Lys300 in NhaA as stick model. TM4, TM8 and TM9 of $ASBT_{NM}$ were superposed on TM4, TM10 and TM11 of NhaA. Na2 of $ASBT_{NM}$ is situated in the nitrogen atom position of Lys300 of NhaA.

Mutations in both sodium ion binding sites

From the transport assay of residues in both the sodium ion binding sites, it seems that both ions contribute to transport of taurocholic acid. On average mutants of the Na2 binding site show a larger decrease in activity than the mutants at the Na1 binding site. The double mutation of residues in both the Na1 and Na2 sites, E260A and Q264A, results in complete loss of transport activity. Although both Na1 and Na2 might have some binding affinities without those residues, when they are combined it would lead to loss of transport activity.

Substrate specificity

Seven amino acid residues located in the substrate binding pocket of the inward-facing structure were substituted to alanine or other amino acids to investigate their role in transport. (Fig. 5.4.) Among these residues M48, N265 and S291 are conserved in human ASBT and alanine mutants show around 60% to 70% activity compared to WT. Though these residues do not directly interact with taurocholic acid in the structure, they are located in the possible transport pathway between the panel domain and the core domain. The decreased activity of these residues could support that taurocholic acid is transported through between the two domains. T112 is also conserved in human ASBT and close to the taurocholic acid but it could not be assigned well in the X-ray crystal structure (Hu, 2011). However, compared to M48, N265 and S291, alanine substitution at this position shows lower transport activity. T112 could have an ability to bind to taurocholic acid. H294 interacts with taurocholic acid through a water molecule and alanine substitution shows around 45% activity. In human ASBT the equivalent residue is Q297. Similar to T112, H294 could also have an essential role for the transport of taurocholic acid. G267 is one of the two non-conserved residues in human ASBT and humanized mutant G267Q shows around 70% activity. In spite of the difference between alanine and glutamine, G267Q still possesses reasonably high activity among the other mutant. Since the substrate binding pockets are not well conserved, this substitution could slightly decrease the activity in $ASBT_{NM}$. The transport assay shows that N295 is crucial for activity with completely loss of uptake of taurocholic acid when it is replaced by an alanine. This result is consistent with the structural information that N295 is the only residue that directly binds to taurocholic acid through its side chain. On the other hand, as mentioned in the results chapter, the whole cell transport assay result from the

previously published data shows N295A as around 20 % activity. Though the exact activity is not clear from this study, N295 is still the one of the important residue for the transport activity.

Although $ASBT_{NM}$ showed similar transport activity to human ASBT, there were some non-conserved residues around the inward facing pocket. N295 was one of those unique residues. Detailed comparisons between human and bacterial ASBTs are described later.

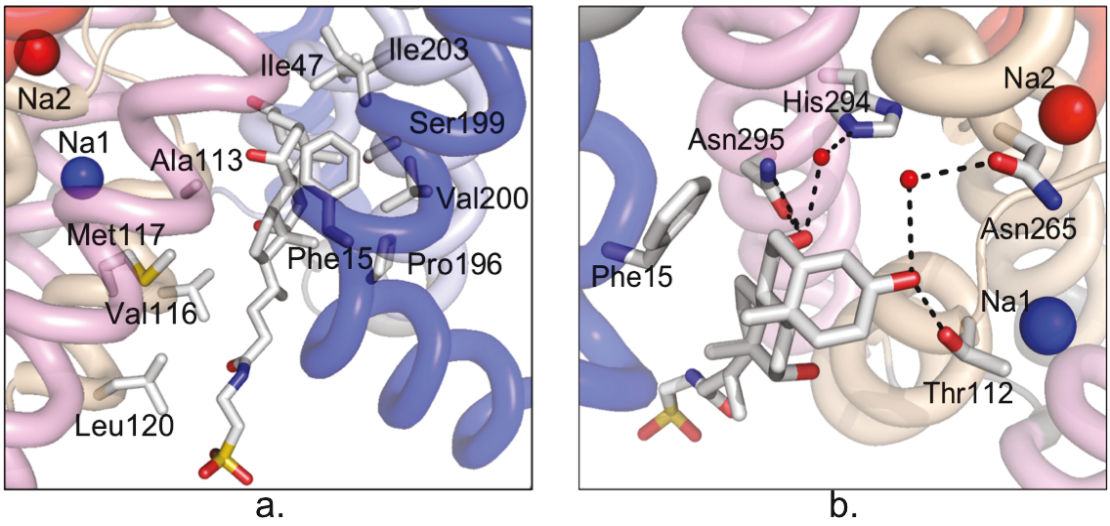


Fig. 5.3. Inward facing pocket in $ASBT_{NM}$ (3ZUY)

a. Inward facing open pocket. The inward facing pocket consists of hydrophobic residues, Phe15, Leu47 Ala113, Val116, Met117, Leu120, Pro196, Ser199, Val200 and Ile203. b. Taurocholic acid binding residues in $ASBT_{NM}$ inward facing open pocket. Thr112 and Asn295 form hydrogen bonding with taurocholic acid. Both Asn265 and His294 interact with taurocholic acid via water molecules.

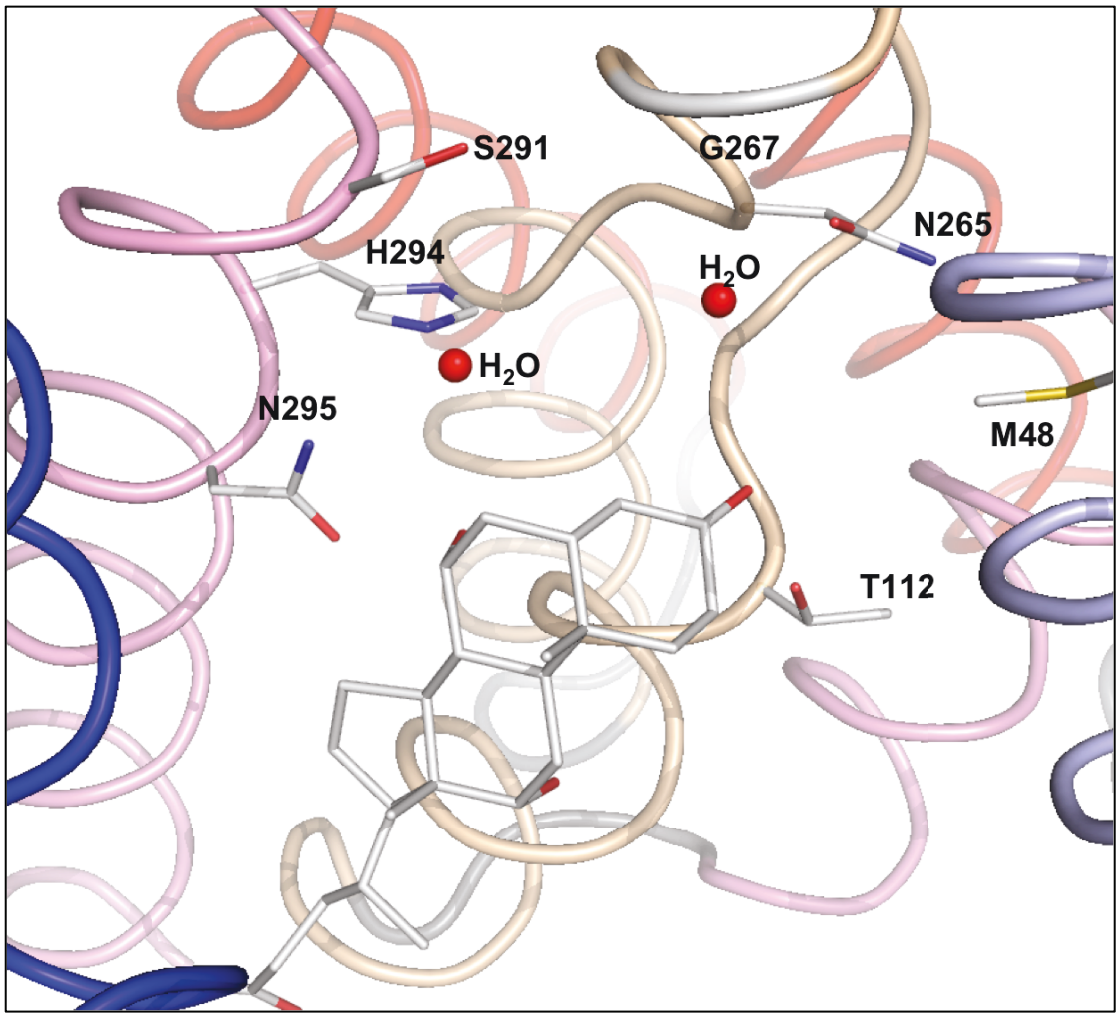


Fig. 5.4. The inward facing pocket of $ASBT_{NM}$ (3ZUY) for proteoliposome transport assay

The residues for proteoliposome transport assay are highlighted as stick model. Two red spheres represent water molecules.

5.2. X-ray crystal structure of ASBT from *Yersinia frederiksenii*.

While this thesis was being written up, the structure of another bacterial homologue of ASBT from *Yersinia frederiksenii* ($ASBT_{Yf}$) was solved (Zhou *et al.* 2014). The sequence identity of $ASBT_{Yf}$ to $ASBT_{NM}$ is 43% and most of the functionally important residues are highly conserved. (Fig. 5.5.) $ASBT_{Yf}$ transports taurocholic acid with a similar K_M value to $ASBT_{NM}$ (around 50 μM). For the $ASBT_{Yf}$ sodium ions were shown to be necessary for the transport of taurocholic acid, in which the stoichiometry of sodium ions to taurocholic acid is 2:1. The structure was solved of the protein in both the inward facing and the outward facing conformation by the LCP crystallization method to 1.95Å and 2.5Å respectively. (Fig. 5.6.) In spite of the high identities, some remarkable differences exist among them.

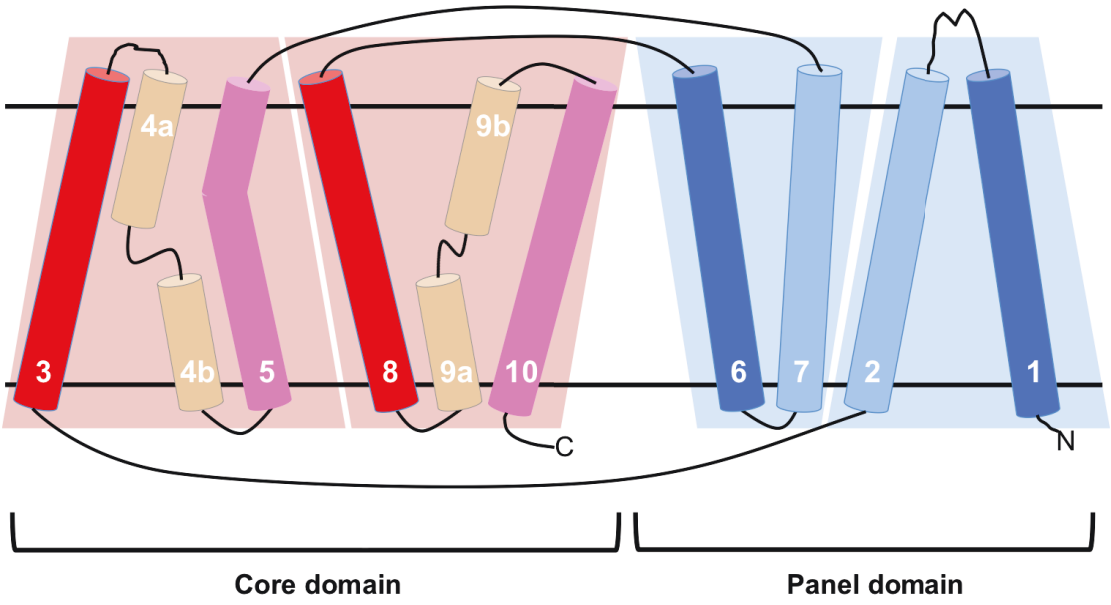


Fig. 5.5. Schematic diagram of the topology $ASBT_{Yf}$.

Cartoon representation of $ASBT_{Yf}$ oriented with the periplasm on top. The helices are coloured to depict TMs 1 to 10 and grouped by domain. Pink and light blue trapezoids indicate inverted repeat motifs, TM1 to 5 and TM6 to10 are psudo-symmetry related each other. Respective pink and light blue motifs form core domain and panel domain.

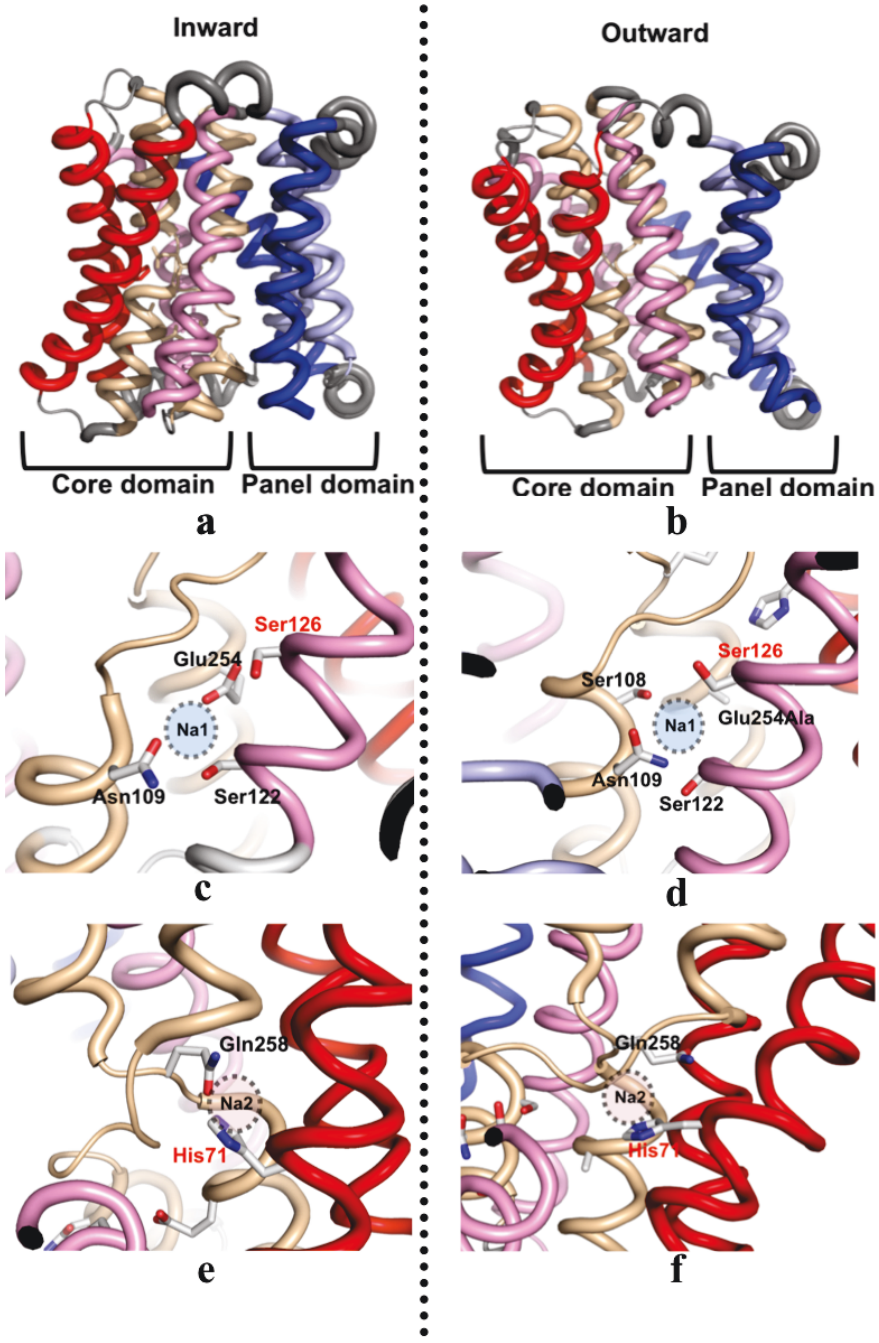


Fig. 5.6. X-ray crystal structures of $ASBT_{Yf}$.

The colours of helices are the same as Fig. 5.5. Overview structures of a). inward facing conformation (4N7W) and b). outward facing conformation (4N7X). The substrate binding pockets were formed between the panel domain and core domain in both inward and outward facing conformations. Supposed Na1 binding sites of $ASBT_{Yf}$ in c) inward facing conformation and d). outward facing conformation. The dashed circle indicates the superposed Na1 from $ASBT_{NM}$ WT structure. Ser126 was

highlighted as red label that was differ from Thr in $ASBT_{NM}$. The first turn of TM4b was unwound in the inward facing conformation. Supposed Na2 binding sites of $ASBT_{Yf}$ in e). inward facing conformation and f). outward facing conformation. Dashed circle indicated the superposed Na2 from $ASBT_{NM}$ WT structure. His71 was highlighted as red label that was differ from Gln in $ASBT_{NM}$.

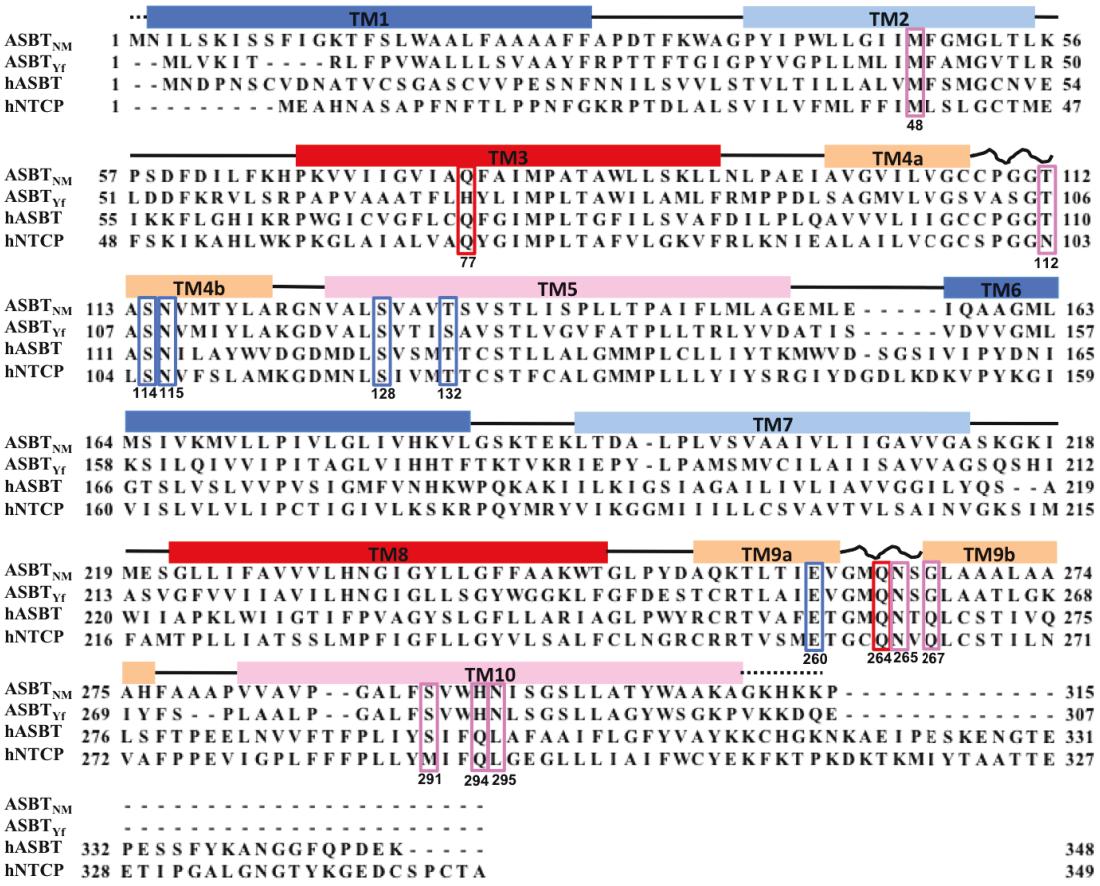


Fig. 5.7. Sequence alignment of ASBT$_{Yf}$ to ASBT$_{NM}$, human ASBT and human NTCP.

Sequence alignment of ASBTyf (UniPort ID: C4ST46) to ASBT$_{NM}$ (UniPort ID: Q9K0A9), human ASBT (UniPort ID: Q12908) and human NTCP (UniPort ID: Q14973) using ClustalW2 (www.ebi.ac.uk/Tools/msa/clustalw2/) and figure preparation in JalView. (Waterhouse *et al.* 2009) The sequence identity of ASBT$_{Yf}$ to ASBT$_{NM}$, human ASBT and human NTCP were 43%, 24% and 25% respectively. The coloured bars depicted the location of the transmembrane α-helices in ASBT$_{NM}$ and the colours of helices were the same as Fig. 5.5. Residues forming Na1 and Na2 binding sites were highlighted as blue and red boxes and inward facing open pocket as pink.

The superposed inward facing conformation structures of $ASBT_{NM}$ (3ZUY), and $ASBT_{Yf}$, (4N7W), showed that both the panel domain and the core domain highly resemble each other except for the kinked TM1 in $ASBT_{NM}$. (Fig. 5.8.) The inward facing conformation of $ASBT_{Yf}$ was solved without either taurocholate or sodium ions bound in the pocket (PDB code; 4N7W). Instead of taurocholic acid, a citrate molecule was bound in the inward facing pocket, which is contained in the crystallization condition. The amino acid residues in the Na1 and Na2 binding sites of $ASBT_{Yf}$ are highly conserved. The only substitutions are conservative: T132 in $ASBT_{NM}$ is a serine in $ASBT_{Yf}$ and Q77 in $ASBT_{NM}$ is a histidine in $ASBT_{Yf}$. A comparison of the sodium binding sites in $ASBT_{NM}$ and $ASBT_{Yf}$ showed that the first turn of TM4b is unwound in $ASBT_{Yf}$ and has moved away from the crossover region between TM4 and TM9. As a result, Ser108 and Asn109 (Ser114 and Asn115 in $ASBT_{NM}$) located in the TM4b are not in position to bind the sodium ion in the Na1 binding site. (Fig. 5.8) It is not clear why sodium ions were not observed in the inward facing $ASBT_{Yf}$ structure. The crystallization conditions were similar to those for $ASBT_{NM}$ (0.1 M Na Citrate and 0.1 M NaCl) and in fact contained slightly higher concentrations of sodium ions. In this structure there was a citrate bound in the active site. Interestingly, the tilt of TM4b exposes the Na1 binding site to the intracellular side and this is a possible sodium transport pathway. It can be assumed that the $ASBT_{NM}$ inward facing structure represents the intermediate state just before releasing substrate and/or sodium ions into the cytoplasm. As the conditions under which the crystals were grown are different to those in the cell, in which sodium concentration gradient between the cell membrane was absent, releasing sodium ion from $ASBT_{NM}$ sodium binding site to cytoplasm could not happen.

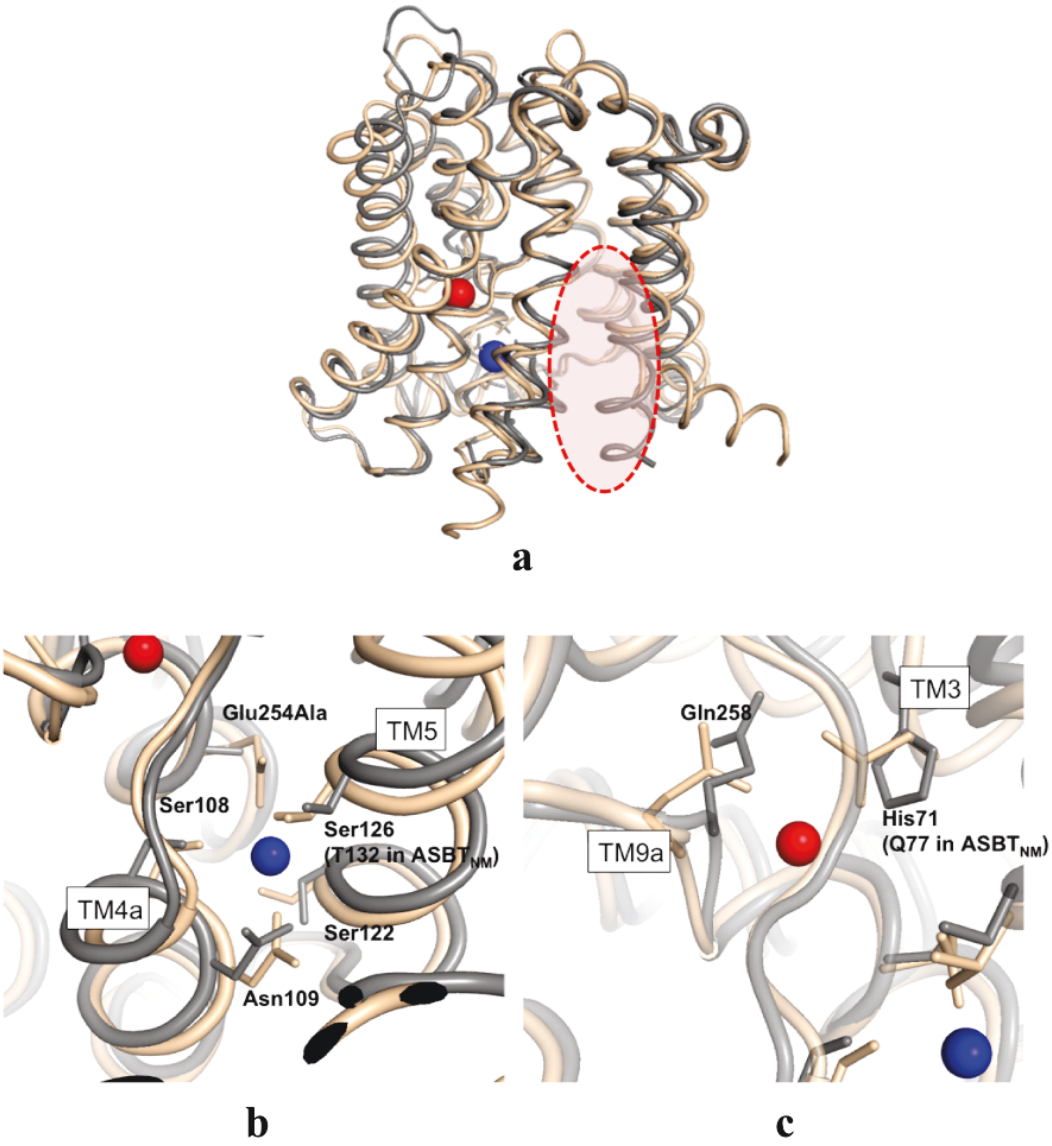


Fig. 5.8. Superposed inward facing conformations of $ASBT_{NM}$ and $ASBT_{Yf}$

Grey and wheat ribbons represent $ASBT_{Yf}$ and $ASBT_{NM}$ respectively. Red and blue spheres represent Na2 and Na1 from the $ASBT_{NM}$ structure. a). Overview of superposed structures. Red circle indicates the taurocholate binding site. b). Na1 binding site. c). Na2 binding site. No significant conformational changes were observed between the two structures.

The outward-facing structure of $ASBT_{Yf}$ was obtained with the equivalent mutation to E260A that was made for $ASBT_{NM}$ (PDB code; 4N7X). They obtained the outward facing conformation of $ASBT_{Yf}$ in crystallisation conditions that did not contain sodium ions in the crystallisation buffers (39% PEG400, 0.1 M Tris-HCl pH 8.5, 0.1 M KCl and 10 mM $MnCl_2$), though no attempt was made to remove the trace sodium ions. The pH value of 8.5 was higher than that of other $ASBT_{NM}$ and inward facing $ASBT_{Yf}$ structures. For $ASBT_{NM}$ no diffracting crystals were obtained under such conditions. The different results would come from various reasons; the crystallization methods were LCP in $ASBT_{Yf}$ and vapour diffusion in $ASBT_{NM}$, absence of sodium ion and taurocholic acid in the crystallization condition of $ASBT_{Yf}$ structure (the addition of taurocholate was necessary to obtain good crystals of $ASBT_{NM}$ using vapour diffusion, in which taurocholic acid binds both in the binding pocket and the crystallisation interface), and, importantly, these are different proteins. As for the inward facing structure, there were no substrate and sodium ions in the $ASBT_{Yf}$ outward facing structure. When the panel domain and the core domain were superposed to that of the inward facing conformation structure individually, each domain aligned well without significant conformational changes. When the core domains of each conformation are superposed, a large movement of the panel domain can be observed, in which the panel domain relatively "rotates" along the core domain. This rigid body motion of the panel domain and the core domain could explain the conformational change from inward facing to outward facing conformation of $ASBT_{Yf}$. From the inward facing conformation, the panel domain moves relative to the core domain and the outward facing pocket is formed by the dissociation of the core domain, TM9b, and the panel domain (TM2 and TM7). (Fig. 5.9.) Due to their highly similar sequence identity and homologous structures, it is likely that this

conformational change mechanism could be also applied for $ASBT_{NM}$ as well. In the $ASBT_{NM}$ structures, the small differences could be observed between the structure of the Q77A mutant and the WT at TM1, TM6 and TM7. Since the displaced TMs are distant from the substituted residue, it is likely that this comes from the different packing between the crystals formed from LCP or vapour diffusion methods and/or the absence of taurocholic acid. From this observation, this movement would imply the flexibility of the panel domain in the inward facing conformation. It is assumed that the flexibility of the panel domain might be important for taurocholic acid transport moving against the core domain.

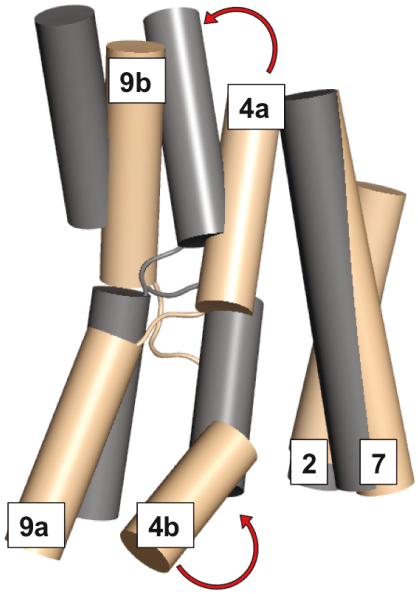


Fig. 5.9. Conformational change between inward and outward facing structures of $ASBT_{Yf}$.

Grey and wheat rods represented outward and inward facing structures of $ASBT_{Yf}$. Rigid body movement of TM4 and TM9 against TM2 and TM7 were observed.

To help to understand the outward facing conformation of WT $ASBT_{NM}$, the core domain of $ASBT_{NM}$ and $ASBT_{Yf}$ were superposed. (Fig. 5.10.) Overall, both TM4 and TM9 were well aligned in the inward facing and the outward facing conformation. However there were some minor differences that unlike the inward facing conformation of $ASBT_{Yf}$, the first turn of TM4b in the structure of $ASBT_{NM}$ forms an α-helix. One interpretation from this comparison is that TM4 and TM9 change their conformation, by unwinding TM4b, to release sodium ions into the cells with the sodium gradient as a driving force. This would mean that the E260A and E254A structures may not be representative of the protein with no sodium ion at Na1. The other possibility is that the citrate ion at the binding site of the inward-facing $ASBT_{Yf}$ causes some conformational changes of the helices.

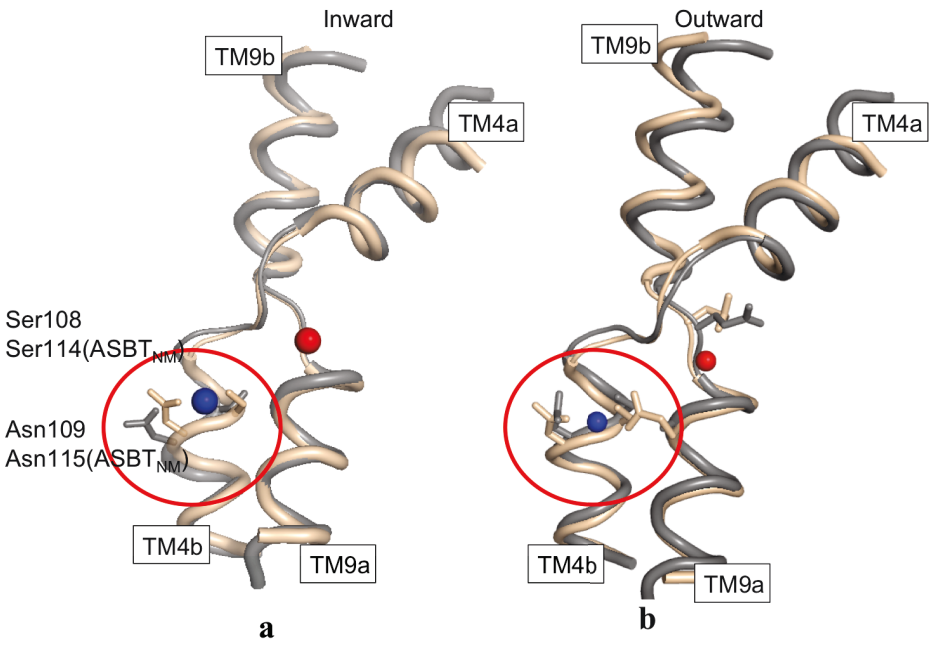


Fig. 5.10. Superposed structures of $ASBT_{NM}$ and $ASBT_{Yf}$ at the core domain.

a). Inward facing conformations were well aligned excepting Na1 binding sites. b). There were no significant differences among outward facing conformations.

The authors of the $ASBT_{Yf}$ paper used a scintillation proximity assay (Miller *et al.*) assay to measure the binding affinity of taurocholic acid to $ASBT_{Yf}$. This method observes the binding of radio labelled taurocholic acid to purified $ASBT_{Yf}$ in detergent solution. They mutated a number of residues in the protein and measure binding. Five of the mutated residues were the same as the $ASBT_{NM}$ mutants, T106V, S283A, N259V, N287V and H286A (T112A, S291A, N265A, N295A and H294A in $ASBT_{NM}$), though three of them were to valine rather than alanine. (Fig. 5.11.) Among these mutants, T106V, N259V, S283A and H286A support the activities seen for $ASBT_{NM}$. The outlier is N295A/N287V. For $ASBT_{NM}$ no transport was observed, while the binding to $ASBT_{YF}$ was around 80%. There can be a number of reasons for this difference. 1) These values were obtained from different methods. One measures binding the other transport. 2) The substituted residues were not the same, and this has an affect on the conformation of the protein (valine for $ASBT_{YF}$ and alanine for $ASBT_{NM}$). 3) The proteins are not the same and the binding mode differs between the two. 4) The proteoliposome transport assay was done on a single batch of purified sample, which had lost activity. However, this mutant also showed low activity in the whole cell assay previously carried out (Hu, 2011) and makes sense with the binding mode seen in the crystal structure. Further work is required to resolve this issue.

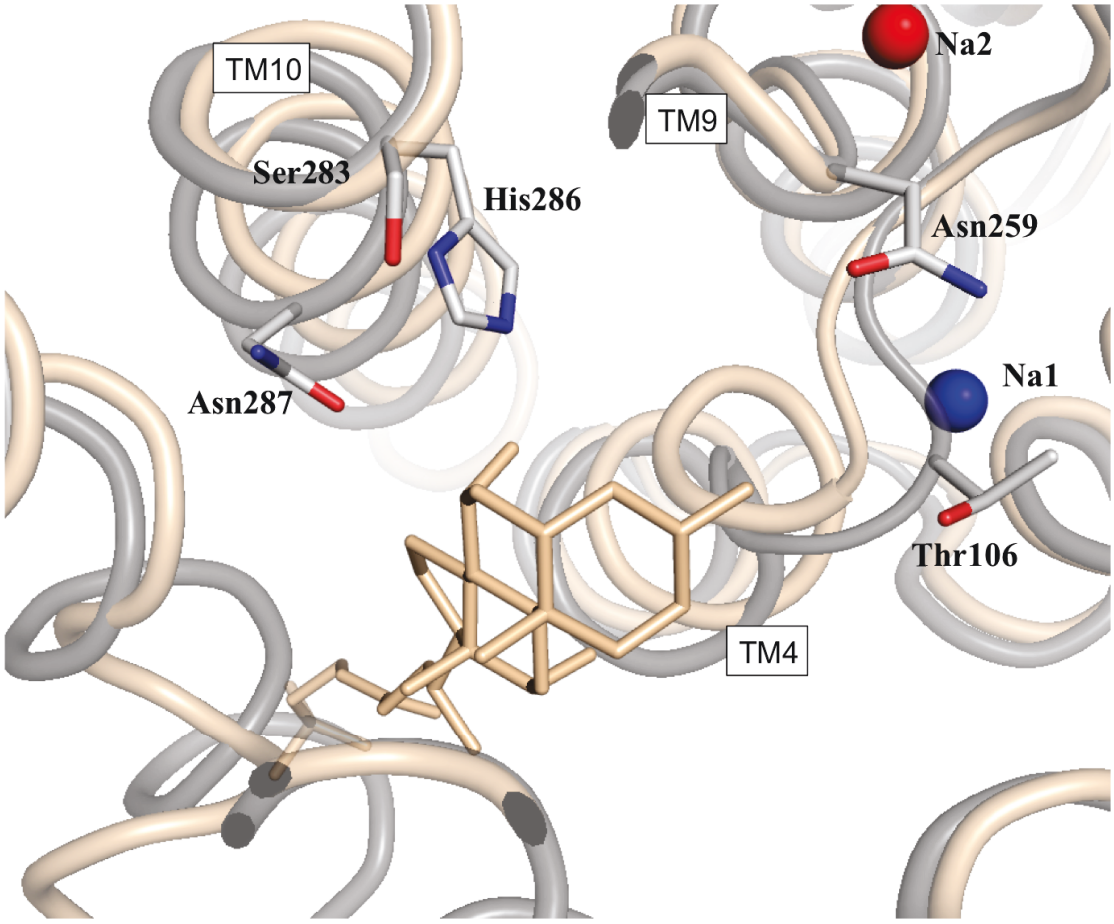


Fig. 5.11. Superposed structures of $ASBT_{NM}$ and $ASBT_{Yf}$ at the taurocholic acid binding site.

Grey ribbon and wheat ribbon represent $ASBT_{Yf}$ and $ASBT_{NM}$ respectively. Red and blue spheres represent Na2 and Na1 and wheat stick represents taurocholic acid from the $ASBT_{NM}$ structure. Sitck residues represent mutated residues of $ASBT_{yf}$.

5.3. Human ASBT homology model

Human ASBT has been extensively studied by mutagenesis coupled with cell-based transport assays. Alanine substitutions at Q75 (Q77; equivalent residues in $ASBT_{NM}$ are shown in brackets) and S112 (S114) were reported to cause loss of transport activity (Sabit *et al.* 2013; Saeki *et al.* 2013). Cysteine substitutions at T130 (T132), E261 (E260) and Q265 (Q264) result in less than 10% activity (Banerjee *et al.* 2008; Sabit *et al.* 2013). Though the absolute percentages differ, the loss of activity is consistent with the results seen for $ASBT_{NM}$. The difference in numbers may be due to the proteins being different or due to the different sensitivity of the assays. The, homology model from $ASBT_{NM}$ therefore can help us understand the human ASBT mechanism.

From the comparison between human ASBT and bacterial ASBTs, both the Na1 and the Na2 binding sites are likely to be very similar. (Fig. 5.12.) It is also likely that human ASBT will change from the outward to the inward-facing states by a rigid body motion of the core and the panel domains followed by the local change of discontinuous TM4 and TM9 helices for the transport of sodium ion. The exact movements are likely to differ especially since TM1 is not present in human ASBT. However, still the mechanism of taurocholic acid transport is not clear due to the low similarity of the mammalian and bacterial species in the substrate binding pocket. From the proteoliposome transport assay, the alanine mutation at N295 had no transport activity, as discussed above. As taurocholic acid is not a natural substrate of $ASBT_{NM}$ in the bacterial cell as described in the introduction, this asparagine might be related to the original substrate specificity of $ASBT_{NM}$. More structural information of other conformations, such as the occluded state, of ASBT is necessary to understand the precise bile acid transport mechanism.

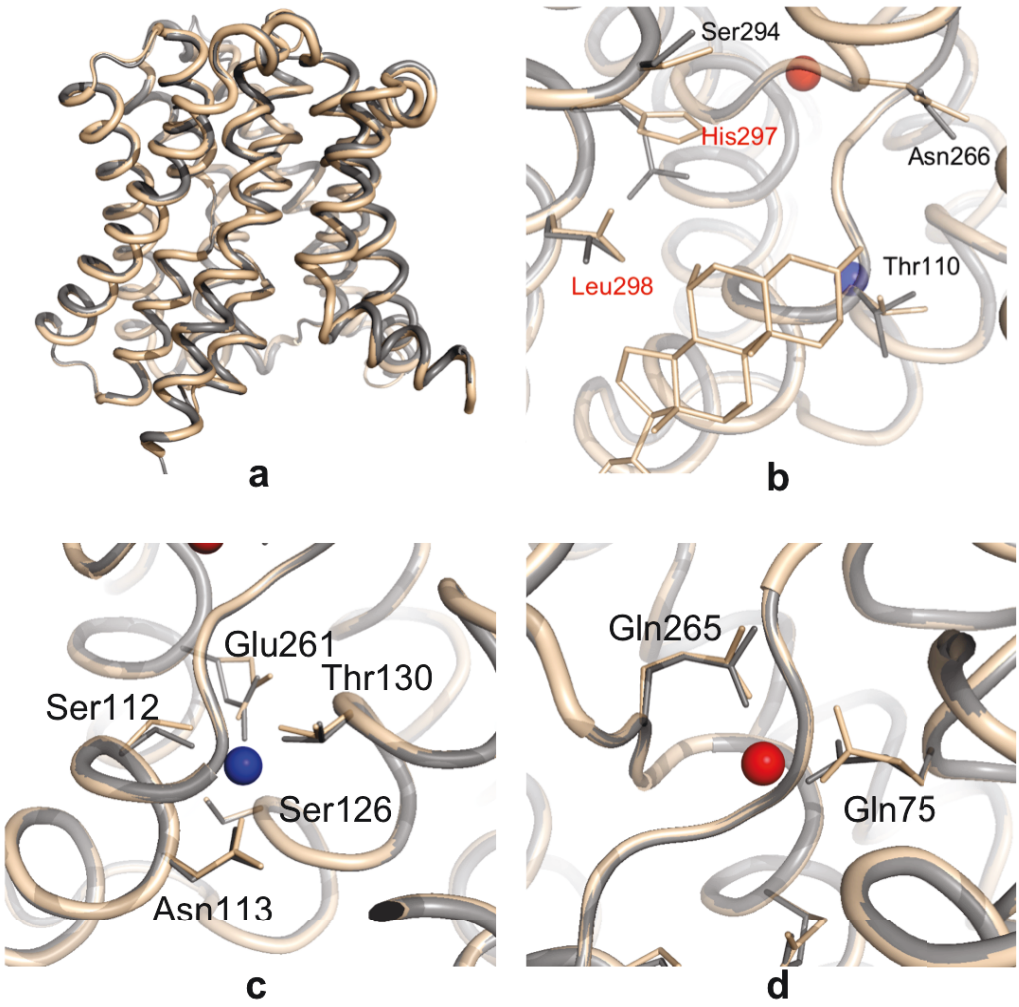


Fig. 5.12. Superposed structures of human ASBT homology model and $ASBT_{NM}$.

a). Overview of superposed structures. Grey and wheat ribbons represented human ASBT model and $ASBT_{NM}$ respectively. **b).** Grey and wheat ribbons represented human ASBT model and $ASBT_{NM}$ respectively. His297 and Leu298 of human ASBT were different from $ASBT_{NM}$ and highlighted as red characters. c). Na1 binding sites. Na1 was shown as blue sphere from $ASBT_{NM}$ structure. d). Na2 binding sites. Na2 was shown as red sphere from $ASBT_{NM}$ structure.

CHAPTER 6

Summary

6. Summary

The X-ray crystal structure of a bacterial homologue of ASBT, $ASBT_{NM}$, was previously solved at 2.2Å In this thesis, in order to understand the precise mechanism of ASBT transport, both structural and functional studies were done. The residues forming the Na1 binding site, the Na2 binding site and the inward facing open pocket were mutated to alanine or other amino acid residues to see the effect on the transport activity of $ASBT_{NM}$. These mutants were expressed in the *E.coli*, purified and reconstituted to the liposome and transport activities were measured by the radio labeled taurocholic acid uptake. The result shows the equivalent contributions of both Na1 and Na2 binding sites for the transport in which alanine substituted mutants decreased the activities. The inward facing open pocket mutants also decrease the transport activities. In particular N295A completely blocks taurocholic acid uptake that suggests the importance of N295 on $ASBT_{NM}$ transport activity. However, this is not conserved in the human ASBT. It should also be noted that the proteoliposome transport assay measurements in this study were not extensively repeated with different batches of protein.

E260 and Q77 are located in the Na1 and Na2 binding sites and alanine mutants give 40% and 60% activities. The X-ray crystal structures of these mutants were solved at 2.9 Å and 3.2 Å respectively. Overall, both mutants form the inward facing conformation as seen for the WT structure. In the E260A structure, Na1 could not be observed in the Na1 binding site. In the Q77A structure, electron density was much weaker in both the Na1 and Na2 binding sites. This may due to the mutation but also could be due to the low resolution of the data. These results indicate that the protein can still take the same conformation even when the functionally important sodium ions are not bound.

Local conformational changes were observed in the Q77A structure around the part of the panel domain that would come from the crystal packing and explain the flexibility of the panel domain. This observation supports the alternating access model of the secondary active transporter, in which movement between the core and the panel domain could happen during the transport of the substrate.

The X-ray crystal structures of ASBT from *Yersinia frederiksenii* ($ASBT_{Yf}$) were solved as the inward facing and the outward facing conformations. The two structures elucidated the supposed mechanism of the transport with the movement of the two domains that could be applied to $ASBT_{NM}$ and also human ASBT as well. Comparisons of human ASBT and bacterial ASBTs shows highly conserved Na1 and Na2 binding sites whereas the residues in the inward-open pocket in which the taurocholate binds in the $ASBT_{NM}$ structure are less conserved.

In addition to the proteoliposome assay, other biophysical techniques were tried to investigate the taurocholic acid and $ASBT_{NM}$ binding properties. CD spectroscopy and ITC measurement did not work well, likely due to the detergent aspect of taurocholic acid, which may stabilise the protein. Although the optimization of the experimental conditions has not been done, preliminary results with the MST suggest that it may be useful in measuring the binding of taurocholic acid to $ASBT_{NM}$.

Bibliography

Abe, T., Y. Kanemitu, et al. (2013). "SLC10A4 is a protease-activated transporter that transports bile acids." J Biochem **154**(1): 93-101.

Afonine, P. V., R. W. Grosse-Kunstleve, et al. (2012). "Towards automated crystallographic structure refinement with phenix.refine." Acta Crystallogr D Biol Crystallogr **68**(Pt 4): 352-367.

Aherne, M., J. A. Lyons, et al. (2012). "A fast, simple and robust protocol for growing crystals in the lipidic cubic phase." J Appl Crystallogr **45**(Pt 6): 1330-1333.

Alberts, B. (2010). "Cell biology: the endless frontier." Mol Biol Cell **21**(22): 3785.

Alrefai, W. A. and R. K. Gill (2007). "Bile acid transporters: structure, function, regulation and pathophysiological implications." Pharm Res **24**(10): 1803-1823.

Andersson, S., D. L. Davis, et al. (1989). "Cloning, structure, and expression of the mitochondrial cytochrome P-450 sterol 26-hydroxylase, a bile acid biosynthetic enzyme." J Biol Chem **264**(14): 8222-8229.

Ballatori, N., W. V. Christian, et al. (2005). "OSTalpha-OSTbeta: a major basolateral bile acid and steroid transporter in human intestinal, renal, and biliary epithelia." Hepatology **42**(6): 1270-1279.

Banerjee, A., N. Hussainzada, et al. (2008). "Electrostatic and potential cation-pi forces may guide the interaction of extracellular loop III with Na+ and bile acids for human apical Na+-dependent bile acid transporter." Biochem J **410**(2): 391-400.

Braun, A., A. Yesilaltay, et al. (2008). "Inhibition of intestinal absorption of cholesterol by ezetimibe or bile acids by SC-435 alters lipoprotein metabolism and extends the lifespan of SR-BI/apoE double knockout mice." Atherosclerosis **198**(1): 77-84.

Broennimann, C., E. F. Eikenberry, et al. (2006). "The PILATUS 1M detector." J Synchrotron Radiat **13**(Pt 2): 120-130.

Buchler, M., J. Konig, et al. (1996). "cDNA cloning of the hepatocyte canalicular isoform of the multidrug resistance protein, cMrp, reveals a novel conjugate export pump deficient in hyperbilirubinemic mutant rats." J Biol Chem **271**(25): 15091-15098.

Burger, S., B. Doring, et al. (2011). "Co-expression studies of the orphan carrier protein Slc10a4 and the vesicular carriers VAChT and VMAT2 in the rat central and peripheral nervous system." Neuroscience **193**: 109-121.

Byrne, J. A., S. S. Strautnieks, et al. (2002). "The human bile salt export pump: characterization of substrate specificity and identification of inhibitors." Gastroenterology **123**(5): 1649-1658.

Caffrey, M. and V. Cherezov (2009). "Crystallizing membrane proteins using lipidic mesophases." Nat Protoc **4**(5): 706-731.

Chen, L., X. Yao, et al. (2012). "Inhibition of apical sodium-dependent bile acid transporter as a novel treatment for diabetes." Am J Physiol Endocrinol Metab **302**(1): E68-76.

Cheng, A., B. Hummel, et al. (1998). "A simple mechanical mixer for small viscous lipid-containing samples." Chem Phys Lipids **95**(1): 11-21.

Cherezov, V., J. Clogston, et al. (2002). "Membrane protein crystallization in meso: lipid type-tailoring of the cubic phase." Biophys J **83**(6): 3393-3407.

Cherezov, V., J. Clogston, et al. (2006). "Room to move: crystallizing membrane proteins in swollen lipidic mesophases." J Mol Biol **357**(5): 1605-1618.

Cherezov, V., W. Liu, et al. (2008). "In meso crystal structure and docking simulations suggest an alternative proteoglycan binding site in the OpcA outer membrane adhesin." Proteins **71**(1): 24-34.

Cherezov, V., E. Yamashita, et al. (2006). "In meso structure of the cobalamin transporter, BtuB, at 1.95 A resolution." J Mol Biol **364**(4): 716-734.

Clarke, D. T. and G. Jones (2004). "CD12: a new high-flux beamline for ultraviolet and vacuum-ultraviolet circular dichroism on the SRS, Daresbury." J Synchrotron Radiat **11**(Pt 2): 142-149.

Craddock, A. L., M. W. Love, et al. (1998). "Expression and transport properties of the human ileal and renal sodium-dependent bile acid transporter." Am J Physiol **274**(1 Pt 1): G157-169.

Dahlback, H. and I. Holmberg (1990). "Oxidation of 5 beta-cholestane-3 alpha,7 alpha, 12 alpha-triol into 3 alpha,7 alpha,12 alpha-trihydroxy-5 beta-cholestanoic acid by cytochrome P-450(26) from rabbit liver mitochondria." Biochem Biophys Res Commun **167**(2): 391-395.

Davis, I. W., A. Leaver-Fay, et al. (2007). "MolProbity: all-atom contacts and structure validation for proteins and nucleic acids." Nucleic Acids Res **35**(Web Server issue): W375-383.

Dawson, P. A., M. Hubbert, et al. (2005). "The heteromeric organic solute transporter alpha-beta, Ostalpha-Ostbeta, is an ileal basolateral bile acid transporter." J Biol Chem **280**(8): 6960-6968.

Dore, A. S., K. Okrasa, et al. (2014). "Structure of class C GPCR metabotropic glutamate receptor 5 transmembrane domain." Nature **511**(7511): 557-562.

Drew, D., M. Lerch, et al. (2006). "Optimization of membrane protein overexpression and purification using GFP fusions." Nat Methods **3**(4): 303-313.

Duhr, S. and D. Braun (2006). "Why molecules move along a temperature gradient." Proc Natl Acad Sci U S A **103**(52): 19678-19682.

Emsley, P. and K. Cowtan (2004). "Coot: model-building tools for molecular graphics." Acta Crystallogr D Biol Crystallogr **60**(Pt 12 Pt 1): 2126-2132.

Eswar, N., B. Webb, et al. (2006). "Comparative protein structure modeling using Modeller." Curr Protoc Bioinformatics **Chapter 5**: Unit 5 6.

Falany, C. N., M. R. Johnson, et al. (1994). "Glycine and taurine conjugation of bile acids by a single enzyme. Molecular cloning and expression of human liver bile acid CoA:amino acid N-acyltransferase." J Biol Chem **269**(30): 19375-19379.

Feng, L., E. B. Campbell, et al. (2010). "Structure of a eukaryotic CLC transporter defines an intermediate state in the transport cycle." Science **330**(6004): 635-641.

Fernandes, C. F., J. R. Godoy, et al. (2007). "The novel putative bile acid transporter SLC10A5 is highly expressed in liver and kidney." Biochem Biophys Res Commun **361**(1): 26-32.

Forrest, L. R., R. Kramer, et al. (2011). "The structural basis of secondary active transport mechanisms." Biochim Biophys Acta **1807**(2): 167-188.

Freire, E. (2008). "Do enthalpy and entropy distinguish first in class from best in class?" Drug Discov Today **13**(19-20): 869-874.

Freyer, M. W. and E. A. Lewis (2008). "Isothermal titration calorimetry: experimental design, data analysis, and probing macromolecule/ligand binding and kinetic interactions." Methods Cell Biol **84**: 79-113.

Furster, C., J. Zhang, et al. (1996). "Purification of a 3beta-hydroxy-delta5-C27-steroid dehydrogenase from pig liver microsomes active in major and alternative pathways of bile acid biosynthesis." J Biol Chem **271**(34): 20903-20907.

Gerloff, T., B. Stieger, et al. (1998). "The sister of P-glycoprotein represents the canalicular bile salt export pump of mammalian liver." J Biol Chem **273**(16): 10046-10050.

Geter, D. R., W. O. Ward, et al. (2006). "Kidney toxicogenomics of chronic potassium bromate exposure in f344 male rats." Transl Oncogenomics **1**: 33-52.

Geyer, J., B. Doring, et al. (2007). "Cloning and functional characterization of human sodium-dependent organic anion transporter (SLC10A6)." J Biol Chem **282**(27): 19728-19741.

Geyer, J., C. F. Fernandes, et al. (2008). "Cloning and molecular characterization of the orphan carrier protein Slc10a4: expression in cholinergic neurons of the rat central nervous system." Neuroscience **152**(4): 990-1005.

Geyer, J., T. Wilke, et al. (2006). "The solute carrier family SLC10: more than a family of bile acid transporters regarding function and phylogenetic relationships." Naunyn Schmiedebergs Arch Pharmacol **372**(6): 413-431.

Gmelin, W., K. Zeth, et al. (2007). "The crystal structure of the L1 intermediate of halorhodopsin at 1.9 angstroms resolution." Photochem Photobiol **83**(2): 369-377.

Godoy, A. P., M. C. Miranda, et al. (2007). "[Analysis of molecular fingerprint and virulence factors of Helicobacter pylori strains]." Arq Gastroenterol **44**(2): 107-112.

Granier, S., A. Manglik, et al. (2012). "Structure of the delta-opioid receptor bound to naltrindole." Nature **485**(7398): 400-404.

Gregoriadis, G. (2007). Liposome technology. New York, Informa Healthcare.

Hagenbuch, B. and P. J. Meier (1994). "Molecular cloning, chromosomal localization, and functional characterization of a human liver Na+/bile acid cotransporter." J Clin Invest **93**(3): 1326-1331.

Hagenbuch, B. and P. J. Meier (2004). "Organic anion transporting polypeptides of the OATP/ SLC21 family: phylogenetic classification as OATP/ SLCO

superfamily, new nomenclature and molecular/functional properties." Pflugers Arch **447**(5): 653-665.

Hediger, M. A., M. J. Coady, et al. (1987). "Expression cloning and cDNA sequencing of the Na+/glucose co-transporter." Nature **330**(6146): 379-381.

Heubi, J. E., W. F. Balistreri, et al. (1982). "Primary bile acid malabsorption: defective in vitro ileal active bile acid transport." Gastroenterology **83**(4): 804-811.

Hofmann, A. F. (1999). "The continuing importance of bile acids in liver and intestinal disease." Arch Intern Med **159**(22): 2647-2658.

Hofmann, K. (1962). "Chemistry and function of polypeptide hormones." Annu Rev Biochem **31**: 213-246.

Hollenstein, K., J. Kean, et al. (2013). "Structure of class B GPCR corticotropin-releasing factor receptor 1." Nature **499**(7459): 438-443.

Hu, N. J., S. Iwata, et al. (2011). "Crystal structure of a bacterial homologue of the bile acid sodium symporter ASBT." Nature **478**(7369): 408-411.

Hylemon, P. B. and J. Harder (1998). "Biotransformation of monoterpenes, bile acids, and other isoprenoids in anaerobic ecosystems." FEMS Microbiol Rev **22**(5): 475-488.

Ito, K., H. Suzuki, et al. (2001). "Single amino acid substitution of rat MRP2 results in acquired transport activity for taurocholate." Am J Physiol Gastrointest Liver Physiol **281**(4): G1034-1043.

Jardetzky, O. (1966). "Simple allosteric model for membrane pumps." Nature **211**(5052): 969-970.

Jasti, J., H. Furukawa, et al. (2007). "Structure of acid-sensing ion channel 1 at 1.9 A resolution and low pH." Nature **449**(7160): 316-323.

Javitt, N. B. (2000). "Biologic role(s) of the 25(R),26-hydroxycholesterol metabolic pathway." Biochim Biophys Acta **1529**(1-3): 136-141.

Javorfi, T., R. Hussain, et al. (2010). "Measuring circular dichroism in a capillary cell using the b23 synchrotron radiation CD beamline at diamond light source." Chirality **22 Suppl 1**: E149-153.

Jelinek, D. F., S. Andersson, et al. (1990). "Cloning and regulation of cholesterol 7 alpha-hydroxylase, the rate-limiting enzyme in bile acid biosynthesis." J Biol Chem **265**(14): 8190-8197.

Jerabek-Willemsen, M., C. J. Wienken, et al. (2011). "Molecular interaction studies using microscale thermophoresis." Assay Drug Dev Technol **9**(4): 342-353.

Kabsch, W. (2010). "Xds." Acta Crystallogr D Biol Crystallogr **66**(Pt 2): 125-132.

Kawate, T. and E. Gouaux (2006). "Fluorescence-detection size-exclusion chromatography for precrystallization screening of integral membrane proteins." Structure **14**(4): 673-681.

Kawate, T., J. C. Michel, et al. (2009). "Crystal structure of the ATP-gated P2X(4) ion channel in the closed state." Nature **460**(7255): 592-598.

Kazmier, K., S. Sharma, et al. (2014). "Conformational dynamics of ligand-dependent alternating access in LeuT." Nat Struct Mol Biol **21**(5): 472-479.

Konig, J., Y. Cui, et al. (2000). "Localization and genomic organization of a new hepatocellular organic anion transporting polypeptide." J Biol Chem **275**(30): 23161-23168.

Krishnamurthy, H. and E. Gouaux (2012). "X-ray structures of LeuT in substrate-free outward-open and apo inward-open states." Nature **481**(7382): 469-474.

Kruse, A. C., J. Hu, et al. (2012). "Structure and dynamics of the M3 muscarinic acetylcholine receptor." Nature **482**(7386): 552-556.

Kullak-Ublick, G. A., B. Hagenbuch, et al. (1995). "Molecular and functional characterization of an organic anion transporting polypeptide cloned from human liver." Gastroenterology **109**(4): 1274-1282.

Kurata, H., S. Suzuki, et al. (2004). "A novel class of apical sodium-dependent bile acid transporter inhibitors: the amphiphilic 4-oxo-1-phenyl-1,4-dihydroquinoline derivatives." Bioorg Med Chem Lett **14**(5): 1183-1186.

Ladbury, J. E., G. Klebe, et al. (2010). "Adding calorimetric data to decision making in lead discovery: a hot tip." Nat Rev Drug Discov **9**(1): 23-27.

Lee, C., H. J. Kang, et al. (2013). "A two-domain elevator mechanism for sodium/proton antiport." Nature **501**(7468): 573-577.

Li, N., Z. Cui, et al. (2007). "Heterodimerization, trafficking and membrane topology of the two proteins, Ost alpha and Ost beta, that constitute the organic solute and steroid transporter." Biochem J **407**(3): 363-372.

Liu, H. T., H. W. He, et al. (2013). "Arylsulfonylamino-benzanilides as inhibitors of the apical sodium-dependent bile salt transporter (SLC10A2)." Molecules **18**(6): 6883-6897.

Liu, W., E. Chun, et al. (2012). "Structural basis for allosteric regulation of GPCRs by sodium ions." Science **337**(6091): 232-236.

Lockless, S. W., M. Zhou, et al. (2007). "Structural and thermodynamic properties of selective ion binding in a K+ channel." PLoS Biol **5**(5): e121.

Loo, D. D., B. A. Hirayama, et al. (2006). "Conformational dynamics of hSGLT1 during Na+/glucose cotransport." J Gen Physiol **128**(6): 701-720.

Maes, M., A. Rimon, et al. (2012). "Revealing the ligand binding site of NhaA Na+/H+ antiporter and its pH dependence." J Biol Chem **287**(45): 38150-38157.

Manglik, A., A. C. Kruse, et al. (2012). "Crystal structure of the micro-opioid receptor bound to a morphinan antagonist." Nature **485**(7398): 321-326.

McCoy, A. J., R. W. Grosse-Kunstleve, et al. (2007). "Phaser crystallographic software." J Appl Crystallogr **40**(Pt 4): 658-674.

Meier, P. J. (1995). "Molecular mechanisms of hepatic bile salt transport from sinusoidal blood into bile." Am J Physiol **269**(6 Pt 1): G801-812.

Miller, P. D., P. D. Delmas, et al. (2008). "Early responsiveness of women with osteoporosis to teriparatide after therapy with alendronate or risedronate." J Clin Endocrinol Metab **93**(10): 3785-3793.

Mitchell, P. (1957). "A general theory of membrane transport from studies of bacteria." Nature **180**(4577): 134-136.

Noe, J., B. Stieger, et al. (2002). "Functional expression of the canalicular bile salt export pump of human liver." Gastroenterology **123**(5): 1659-1666.

Oelkers, P., L. C. Kirby, et al. (1997). "Primary bile acid malabsorption caused by mutations in the ileal sodium-dependent bile acid transporter gene (SLC10A2)." J Clin Invest **99**(8): 1880-1887.

Parker, J. L. and S. Newstead (2014). "Molecular basis of nitrate uptake by the plant nitrate transporter NRT1.1." Nature **507**(7490): 68-72.

Perez, C., B. Faust, et al. (2014). "Substrate-bound outward-open state of the betaine transporter BetP provides insights into Na+ coupling." Nat Commun **5**: 4231.

Perez, C., C. Koshy, et al. (2011). "Substrate specificity and ion coupling in the Na+/betaine symporter BetP." EMBO J **30**(7): 1221-1229.

Perez, C., C. Koshy, et al. (2012). "Alternating-access mechanism in conformationally asymmetric trimers of the betaine transporter BetP." Nature **490**(7418): 126-130.

Picollo, A., Y. Xu, et al. (2012). "Synergistic substrate binding determines the stoichiometry of transport of a prokaryotic H(+)/Cl(-) exchanger." Nat Struct Mol Biol **19**(5): 525-531, S521.

Pikuleva, I. A., A. Babiker, et al. (1998). "Activities of recombinant human cytochrome P450c27 (CYP27) which produce intermediates of alternative bile acid biosynthetic pathways." J Biol Chem **273**(29): 18153-18160.

Rajarathnam, K. and J. Rosgen (2014). "Isothermal titration calorimetry of membrane proteins - progress and challenges." Biochim Biophys Acta **1838**(1 Pt A): 69-77.

Russell, D. W. (2003). "The enzymes, regulation, and genetics of bile acid synthesis." Annu Rev Biochem **72**: 137-174.

Sabit, H., S. S. Mallajosyula, et al. (2013). "Transmembrane domain II of the human bile acid transporter SLC10A2 coordinates sodium translocation." J Biol Chem **288**(45): 32394-32404.

Saeki, T., K. Sato, et al. (2013). "Importance of uncharged polar residues and proline in the proximal two-thirds (Pro107-Ser128) of the highly conserved region of mouse ileal Na+-dependent bile acid transporter, Slc10a2, in transport activity and cellular expression." BMC Physiol **13**: 4.

Sanchez-Weatherby, J., M. W. Bowler, et al. (2009). "Improving diffraction by humidity control: a novel device compatible with X-ray beamlines." Acta Crystallogr D Biol Crystallogr **65**(Pt 12): 1237-1246.

Schlegel, S., J. Lofblom, et al. (2012). "Optimizing membrane protein overexpression in the Escherichia coli strain Lemo21(DE3)." J Mol Biol **423**(4): 648-659.

Schobert, B., J. Cupp-Vickery, et al. (2002). "Crystallographic structure of the K intermediate of bacteriorhodopsin: conservation of free energy after photoisomerization of the retinal." J Mol Biol **321**(4): 715-726.

Schroeder, A., U. Eckhardt, et al. (1998). "Substrate specificity of the rat liver Na(+)-bile salt cotransporter in Xenopus laevis oocytes and in CHO cells." Am J Physiol **274**(2 Pt 1): G370-375.

Schwarz, M., A. C. Wright, et al. (2000). "The bile acid synthetic gene 3beta-hydroxy-Delta(5)-C(27)-steroid oxidoreductase is mutated in progressive intrahepatic cholestasis." J Clin Invest **106**(9): 1175-1184.

Seidel, S. A., C. J. Wienken, et al. (2012). "Label-free microscale thermophoresis discriminates sites and affinity of protein-ligand binding." Angew Chem Int Ed Engl **51**(42): 10656-10659.

Shaffer, P. L., A. Goehring, et al. (2009). "Structure and mechanism of a Na+-independent amino acid transporter." Science **325**(5943): 1010-1014.

Shiao, T., M. Iwahashi, et al. (2000). "Structural and functional characterization of liver cell-specific activity of the human sodium/taurocholate cotransporter." Genomics **69**(2): 203-213.

Shimamura, T., S. Weyand, et al. (2010). "Molecular basis of alternating access membrane transport by the sodium-hydantoin transporter Mhp1." Science **328**(5977): 470-473.

Sobolevsky, A. I., M. P. Rosconi, et al. (2009). "X-ray structure, symmetry and mechanism of an AMPA-subtype glutamate receptor." Nature **462**(7274): 745-756.

Solaas, K., A. Ulvestad, et al. (2000). "Subcellular organization of bile acid amidation in human liver: a key issue in regulating the biosynthesis of bile salts." J Lipid Res **41**(7): 1154-1162.

Sonoda, Y., S. Newstead, et al. (2011). "Benchmarking membrane protein detergent stability for improving throughput of high-resolution X-ray structures." Structure **19**(1): 17-25.

Srinivasan, V., A. J. Pierik, et al. (2014). "Crystal structures of nucleotide-free and glutathione-bound mitochondrial ABC transporter Atm1." Science **343**(6175): 1137-1140.

Striegel, A. R., L. M. Biela, et al. (2012). "Calcium binding by synaptotagmin's C2A domain is an essential element of the electrostatic switch that triggers synchronous synaptic transmission." J Neurosci **32**(4): 1253-1260.

Studier, F. W. (2005). "Protein production by auto-induction in high density shaking cultures." Protein Expr Purif **41**(1): 207-234.

Stumpfe, D., A. Bill, et al. (2010). "Targeting multifunctional proteins by virtual screening: structurally diverse cytohesin inhibitors with differentiated biological functions." ACS Chem Biol **5**(9): 839-849.

Sun, A. Q., N. Balasubramaniyan, et al. (2006). "Identification of functionally relevant residues of the rat ileal apical sodium-dependent bile acid cotransporter." J Biol Chem **281**(24): 16410-16418.

Sun, A. Q., R. Salkar, et al. (2003). "A 14-amino acid sequence with a beta-turn structure is required for apical membrane sorting of the rat ileal bile acid transporter." J Biol Chem **278**(6): 4000-4009.

Suzuki, S. and P. J. Henderson (2006). "The hydantoin transport protein from Microbacterium liquefaciens." J Bacteriol **188**(9): 3329-3336.

Tamai, I., J. Nezu, et al. (2000). "Molecular identification and characterization of novel members of the human organic anion transporter (OATP) family." Biochem Biophys Res Commun **273**(1): 251-260.

Tan, Q., Y. Zhu, et al. (2013). "Structure of the CCR5 chemokine receptor-HIV entry inhibitor maraviroc complex." Science **341**(6152): 1387-1390.

Tanford, C. (1982). "Simple model for the chemical potential change of a transported ion in active transport." Proc Natl Acad Sci U S A **79**(9): 2882-2884.

Tang, L., L. Bai, et al. (2010). "Crystal structure of the carnitine transporter and insights into the antiport mechanism." Nat Struct Mol Biol **17**(4): 492-496.

Tao, X., J. L. Avalos, et al. (2009). "Crystal structure of the eukaryotic strong inward-rectifier K+ channel Kir2.2 at 3.1 A resolution." Science **326**(5960): 1668-1674.

Tiefenbrunn, T., W. Liu, et al. (2011). "High resolution structure of the ba3 cytochrome c oxidase from Thermus thermophilus in a lipidic environment." PLoS One **6**(7): e22348.

Trauner, M. and J. L. Boyer (2003). "Bile salt transporters: molecular characterization, function, and regulation." Physiol Rev **83**(2): 633-671.

Wallin, E. and G. von Heijne (1998). "Genome-wide analysis of integral membrane proteins from eubacterial, archaean, and eukaryotic organisms." Protein Sci **7**(4): 1029-1038.

Wang, C., Y. Jiang, et al. (2013). "Structural basis for molecular recognition at serotonin receptors." Science **340**(6132): 610-614.

Wang, H., Z. Yan, et al. (2012). "Alteration in placental expression of bile acids transporters OATP1A2, OATP1B1, OATP1B3 in intrahepatic cholestasis of pregnancy." Arch Gynecol Obstet **285**(6): 1535-1540.

Waterhouse, A. M., J. B. Procter, et al. (2009). "Jalview Version 2--a multiple sequence alignment editor and analysis workbench." Bioinformatics **25**(9): 1189-1191.

Weinman, S. A. (1997). "Electrogenicity of Na(+)-coupled bile acid transporters." Yale J Biol Med **70**(4): 331-340.

Weinman, S. A., M. W. Carruth, et al. (1998). "Bile acid uptake via the human apical sodium-bile acid cotransporter is electrogenic." J Biol Chem **273**(52): 34691-34695.

Weissig, V. (2010). Liposomes : methods and protocols. New York, Humana Press.

West, K. L., T. Ramjiganesh, et al. (2002). "1-[4-[4[(4R,5R)-3,3-Dibutyl-7-(dimethylamino)-2,3,4,5-tetrahydro-4-hydroxy-1,1-di oxido-1-benzothiepin-5-yl]phenoxy]butyl]-4-aza-1-azoniabicyclo[2.2.2]octane methanesulfonate (SC-435), an ileal apical sodium-codependent bile acid transporter inhibitor alters hepatic cholesterol metabolism and lowers plasma low-density lipoprotein-cholesterol concentrations in guinea pigs." J Pharmacol Exp Ther **303**(1): 293-299.

Weyand, S., T. Shimamura, et al. (2008). "Structure and molecular mechanism of a nucleobase-cation-symport-1 family transporter." Science **322**(5902): 709-713.

White, J. A., P. J. McAlpine, et al. (1997). "Guidelines for human gene nomenclature (1997). HUGO Nomenclature Committee." Genomics **45**(2): 468-471.

Wien, F., A. J. Miles, et al. (2005). "VUV irradiation effects on proteins in high-flux synchrotron radiation circular dichroism spectroscopy." J Synchrotron Radiat **12**(Pt 4): 517-523.

Wienken, C. J., P. Baaske, et al. (2010). "Protein-binding assays in biological liquids using microscale thermophoresis." Nat Commun **1**: 100.

Wikvall, K. (1981). "Purification and properties of a 3 beta-hydroxy-delta 5-C27-steroid oxidoreductase from rabbit liver microsomes." J Biol Chem **256**(7): 3376-3380.

Winn, M. D., C. C. Ballard, et al. (2011). "Overview of the CCP4 suite and current developments." Acta Crystallogr D Biol Crystallogr **67**(Pt 4): 235-242.

Wohri, A. B., W. Y. Wahlgren, et al. (2009). "Lipidic sponge phase crystal structure of a photosynthetic reaction center reveals lipids on the protein surface." Biochemistry **48**(41): 9831-9838.

Wong, M. H., P. Oelkers, et al. (1995). "Identification of a mutation in the ileal sodium-dependent bile acid transporter gene that abolishes transport activity." J Biol Chem **270**(45): 27228-27234.

Wu, H., D. Wacker, et al. (2012). "Structure of the human kappa-opioid receptor in complex with JDTic." Nature **485**(7398): 327-332.

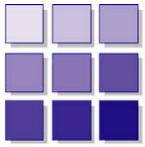
Yamashita, A., S. K. Singh, et al. (2005). "Crystal structure of a bacterial homologue of Na+/Cl--dependent neurotransmitter transporters." Nature **437**(7056): 215-223.

Zhang, C., Y. Srinivasan, et al. (2012). "High-resolution crystal structure of human protease-activated receptor 1." Nature **492**(7429): 387-392.

Zhou, X., E. J. Levin, et al. (2014). "Structural basis of the alternating-access mechanism in a bile acid transporter." Nature **505**(7484): 569-573.

Appendix1

Crystallisation screens: MemGold HT-96

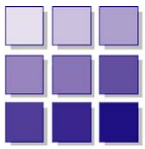


moleculardimensions.com



MemGold HT-96 Rows A - B MD1-41

Tube #	Salt	Buffer	pH	Precipitant
A1	None	0.08 M sodium citrate	5.2	2.2 M ammonium sulfate
A2	None	0.01 M Tris	8.0	1.2 M tri-sodium citrate
A3	None	0.015 M tricine	8.5	24 % w/v PEG 4000
A4	0.36 M sodium chloride/0.1% w/v sodium azide	0.015 M sodium phosphate	7.0	9.9 % w/v PEG 4000
A5	0.3 M sodium chloride	0.01 M Tris	8.0	27.5 % w/v PEG 4000
A6	None	0.225 M MES/bis-tris	6.6	6.6 % w/v PEG 6000
A7	0.1 M ammonium sulfate	0.1 M HEPES	7.5	12.0 % w/v PEG 4000/ 22 % v/v glycerol
A8	0.02 M calcium chloride/0.01 M magnesium sulfate/0.02 M sodium chloride	0.02 M MES	6.5	7.7 % w/v PEG 1500
A9	None	0.05 M HEPES	7.5	2.5 M ammonium sulfate
A10	None	0.0665 M HEPES	7.5	1.1 M tri-sodium citrate
A11	None	0.15 M potassium phosphate	6.5	3.3 M ammonium sulfate
A12	0.1 M magnesium acetate	0.1 M sodium citrate	5.8	14 % w/v PEG 5000 MME
B1	0.1 M sodium chloride	0.02 M sodium citrate	5.6	11 % w/v PEG 3350
B2	0.1 M sodium chloride	0.02 M sodium citrate	5.6	5.5 % w/v PEG 3350
B3	0.05 M calcium chloride/0.05 M barium chloride	0.1 M Tris	8.2	32 % v/v PEG 400
B4	0.05 M sodium chloride	0.1 M sodium phosphate	6.2	16 % w/v PEG 4000
B5*	0.1 M magnesium chloride	0.03 M Tris-hydrochloride	8.2	19 % w/v PEG 4000
B6	0.2 M sodium chloride	0.025 M HEPES	7.5	13 % w/v PEG 4000
B7	None	0.1 M HEPES	7.5	11 % w/v PEG 3350
B8	0.1 M sodium chloride	0.02 M KMES	6.7	6.6 % w/v PEG 4000
B9	0.1 M potassium chloride	0.02 M Tris	7.0	20 % w/v PEG 4000
B10	0.05 M magnesium chloride/0.1% w/v sodium azide	0.1 M sodium cacodylate	6.7	6.6 % w/v PEG 3350
B11*	0.2 M potassium chloride	0.1 M sodium citrate	5.5	37 % v/v pentaerythritol propoxylate (5/4 PO/OH)
B12	None	0.1 M Tris	8.0	5.5 % w/v PEG 4000

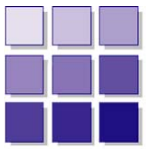


moleculardimensions.com



MemGold HT-96 Rows A - B MD1-41

Tube #	Salt	Buffer	pH	Precipitant
A1	None	0.08 M sodium citrate	5.2	2.2 M ammonium sulfate
A2	None	0.01 M Tris	8.0	1.2 M tri-sodium citrate
A3	None	0.015 M tricine	8.5	24 % w/v PEG 4000
A4	0.36 M sodium chloride/0.1% w/v sodium azide	0.015 M sodium phosphate	7.0	9.9 % w/v PEG 4000
A5	0.3 M sodium chloride	0.01 M Tris	8.0	27.5 % w/v PEG 4000
A6	None	0.225 M MES/bis-tris	6.6	6.6 % w/v PEG 6000
A7	0.1 M ammonium sulfate	0.1 M HEPES	7.5	12.0 % w/v PEG 4000/ 22 % v/v glycerol
A8	0.02 M calcium chloride/0.01 M magnesium sulfate/0.02 M sodium chloride	0.02 M MES	6.5	7.7 % w/v PEG 1500
A9	None	0.05 M HEPES	7.5	2.5 M ammonium sulfate
A10	None	0.0665 M HEPES	7.5	1.1 M tri-sodium citrate
A11	None	0.15 M potassium phosphate	6.5	3.3 M ammonium sulfate
A12	0.1 M magnesium acetate	0.1 M sodium citrate	5.8	14 % w/v PEG 5000 MME
B1	0.1 M sodium chloride	0.02 M sodium citrate	5.6	11 % w/v PEG 3350
B2	0.1 M sodium chloride	0.02 M sodium citrate	5.6	5.5 % w/v PEG 3350
B3	0.05 M calcium chloride/0.05 M barium chloride	0.1 M Tris	8.2	32 % v/v PEG 400
B4	0.05 M sodium chloride	0.1 M sodium phosphate	6.2	16 % w/v PEG 4000
B5*	0.1 M magnesium chloride	0.03 M Tris-hydrochloride	8.2	19 % w/v PEG 4000
B6	0.2 M sodium chloride	0.025 M HEPES	7.5	13 % w/v PEG 4000
B7	None	0.1 M HEPES	7.5	11 % w/v PEG 3350
B8	0.1 M sodium chloride	0.02 M KMES	6.7	6.6 % w/v PEG 4000
B9	0.1 M potassium chloride	0.02 M Tris	7.0	20 % w/v PEG 4000
B10	0.05 M magnesium chloride/0.1% w/v sodium azide	0.1 M sodium cacodylate	6.7	6.6 % w/v PEG 3350
B11*	0.2 M potassium chloride	0.1 M sodium citrate	5.5	37 % v/v pentaerythritol propoxylate (5/4 PO/OH)
B12	None	0.1 M Tris	8.0	5.5 % w/v PEG 4000

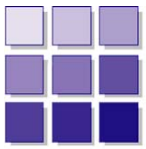


moleculardimensions.com



MemGold HT-96 Rows C- D MD1-41

Tube #	Salt	Buffer	pH	Precipitant
C1	0.1 M sodium chloride	0.02 M Tris	7.0	7.7 % w/v PEG 4000
C2	0.1 M magnesium chloride	0.1 M Tris	7.5	22 % v/v PEG 400
C3	0.04 M sodium chloride	0.04 M Tris	8.0	27 % v/v PEG 350 MME
C4	0.05 M sodium chloride/0.02 M magnesium chloride	0.1 M sodium citrate	6.0	22 % v/v PEG 400
C5	None	0.1 M sodium acetate	5.5	8.8 % w/v PEG 2000 MME
C6	None	0.4 M ammonium acetate	8.0	13 % w/v PEG 2000 MME
C7	None	0.02 M bis Tris	7.0	15 % w/v PEG 2000
C8	0.1 M sodium chloride/0.1 M magnesium chloride	0.02 M Tris	7.5	11 % w/v PEG 1500
C9	0.1 M sodium chloride/0.1 M magnesium chloride	0.1 M HEPES	8.0	11 % w/v PEG 1500
C10	0.2 M sodium acetate/0.2 M Potassium Chloride	0.1 M HEPES	7.0	22 % w/v PEG 3000
C11	0.02 M nickel sulfate	0.01 M HEPES	7.0	33 % v/v Jeffamine-M600
C12	0.15 M sodium chloride	0.1 M Tris	8.0	13 % w/v PEG 6000
D1	0.2 M calcium chloride	0.1 M HEPES	7.5	53 % v/v PEG 400
D2	0.05 M magnesium acetate	0.05 M sodium acetate	5.0	28 % v/v PEG 400
D3	None	0.05 M HEPES	7.5	22 % v/v PEG 4000
D4	0.2 M calcium chloride	0.1 M Tris hydrochloride	8.0	44 % v/v PEG 400
D5	0.05 M magnesium acetate	0.05 M sodium acetate	5.4	24 % v/v PEG 400
D6	0.2 M calcium chloride	0.1 M MES	6.5	26 % v/v PEG 350 MME
D7	0.1 M potassium chloride	0.1 M Tris	8.5	39 % v/v PEG 400
D8	0.05 M magnesium chloride	0.1 M glycine	9.0	22 % v/v PEG 400
D9	0.1 M ammonium sulfate	0.1 M glycine	3.8	28 % w/v tri-ethylene glycol
D10	0.15 M sodium formate	0.1 M HEPES	7.2	18 % w/v PEG 3350
D11	None	0.2 M sodium acetate	6.8	8.8 % w/v PEG 6000
D12	0.2 M potassium chloride	0.1 M MES	6.5	18 % w/v PEG 6000

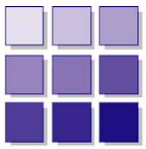


moleculardimensions.com



MemGold HT-96 **Rows E - F** **MD1-41**

Tube #	Salt	Buffer	pH	Precipitant
E1	0.22 M sodium citrate	0.1 M Tris	8.0	35 % v/v PEG 400
E2	None	0.1 M sodium acetate	4.5	17 % v/v PEG 400
E3	None	0.02 M Tris	8.5	1.0 M lithium sulfate/1.8 % w/v PEG 8000
E4	None	0.02 M Tris	7.5	22 % v/v PEG 550 MME
E5	0.05 M sodium chloride	0.02 M glycine	10.0	33 % w/v PEG 1000
E6	0.2 M magnesium chloride	0.1 M Tris	8.5	25 % w/v PEG 4000
E7	0.2 M magnesium chloride	0.1 M sodium cacodylate	6.5	31 % w/v PEG 2000
E8	None	0.64 M sodium acetate	4.6	18 % w/v PEG 3350
E9	0.1 M sodium chloride/0.1 M cadmium chloride	0.1 M Tris hydrochloride	8.0	33 % v/v PEG 400
E10	None	0.1 M Bicine	8.9	31 % w/v PEG 2000
E11	0.05 M sodium sulfate/0.05 M lithium sulfate	0.05 M Tris	8.5	35 % v/v PEG 400
E12	0.1 M sodium chloride	0.05 M glycine	9.5	33 % v/v PEG 300
F1	0.3 M magnesium nitrate	0.1 M Tris	8.0	23 % w/v PEG 2000
F2	0.12 M lithium sulfate	0.02 M Tris/0.1 M sodium citrate	7.5/ 5.0	20 % v/v PEG 300
F3	0.1 M sodium chloride	0.12 M Tris	9.4	20 % v/v PEG 400
F4	0.2 M sodium chloride	0.1 M HEPES	7.0	22 % v/v PEG 550 MME
F5	0.1 M sodium chloride/0.325 M sodium acetate	0.1 M Tris	8.0	21 % v/v PEG 400
F6	0.02 M sodium citrate	0.08 M sodium phosphate	6.2	18 % w/v PEG 2000
F7	0.02 M potassium nitrate	0.03 M potassium citrate	6.5	7.7 % w/v PEG 4000
F8	0.1 M sodium chloride/0.005 M magnesium chloride	0.1 M Tris	8.5	30 % w/v PEG 2000 MME
F9	0.2 M calcium chloride	0.1 M HEPES	7.0	33 % v/v PEG 400
F10	0.1 M calcium chloride	0.1 M Tris	6.5	13 % w/v PEG 2000 MME
F11	0.2 M ammonium sulfate/0.02 M sodium chloride	0.02 M sodium acetate	4.0	33 % v/v PEG 200
F12	0.07 M sodium chloride	0.05 M sodium citrate	4.5	22 % v/v PEG 400

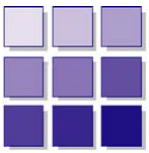


moleculardimensions.com



MemGold HT-96 Rows G - H MD1-41

Tube #	Salt	Buffer	pH	Precipitant
G1	0.2 M ammonium sulfate	0.1 M sodium acetate	4.6	28 % v/v PEG 550 MME
G2	None	0.05 M glycine	9.0	55 % v/v PEG 400
G3	0.1 M magnesium chloride/0.1M sodium chloride	0.1 M Tris	8.5	33 % v/v PEG 400
G4	0.1 M lithium sulfate/0.05 M di-sodium hydrogen phosphate	0.05 M citric acid	None	19 % w/v PEG 1000
G5	0.2 M magnesium chloride/ 0.1 M potassium chloride	0.025 M sodium citrate	4.0	33 % v/v PEG 400
G6	0.05 M zinc acetate	0.05 M MES	6.1	11 % w/v PEG 8000
G7	0.3 M magnesium nitrate	0.1 M Tris	8.0	22 % w/v PEG 8000
G8	0.1 M sodium chloride/4% v/v ethylene glycol	0.1 M MES	6.5	33 % v/v PEG 400
G9	0.05 M sodium chloride	0.1 M sodium citrate	5.5	26 % v/v PEG 400
G10	0.1 M lithium sulfate	0.1 M glycine	9.3	30 % v/v PEG 400
G11*	0.15 M potassium citrate/ 0.05 M lithium citrate	0.1 M sodium phosphate	-	22 % w/v PEG 6000
G12	0.001 M zinc sulphate	0.05 M HEPES	7.8	28 % v/v PEG 600
H1	0.1 M sodium chloride	0.1 M sodium phosphate	7.0	33 % v/v PEG 300
H2	0.1 M sodium chloride	0.05 M Bicine	9.0	33 % v/v PEG 300
H3	0.05 M zinc acetate/6% v/v ethylene glycol	0.1 M sodium cacodylate	6.0	6.6 % w/v PEG 8000
H4	0.2 M lithium sulfate	0.1 M sodium citrate	3.5	28 % v/v PEG 400
H5	0.1 M sodium chloride	0.1 M Tris	7.5	11 % w/v PEG 4000
H6*	0.05 M lithium sulfate	0.1 M tricine	7.4	7 % w/v PEG 3000
H7*	0.2 M calcium chloride	0.1 M MES	6.5	33% v/v PEG 400
H8*	1 M sodium chloride	0.1 M sodium citrate	6.0	28% w/v PEG 4000
H9*	None	0.1 M HEPES	7.5	11% w/v PEG 4000
H10*	0.002 M zinc sulfate	0.08 M HEPES	7.0	25 % v/v Jeffamine ED2001
H11*	0.001 M cadmium chloride/0.03 M magnesium chloride	0.1 M MES	6.5	30 % v/v PEG 400
H12*	None	0.1 M bis-tris-propane	7.0	3.0 M sodium chloride

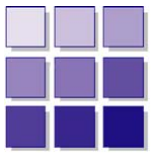


moleculardimensions.com



MemStart™ & MemSys™ HT-96 Rows A - D MD1-33

Tube #	Salt	Buffer	pH	Precipitant
A1	None	0.1 M sodium acetate	4.6	2 M ammonium sulfate
A2	None	0.1 M ADA	6.5	1 M ammonium sulfate
A3	None	None	-	2 M ammonium sulfate
A4	None	0.1 M Tris	8.5	2 M ammonium sulfate
A5	None	0.1 M Na HEPES	7.5	1.5 M lithium sulfate
A6	None	0.1 M sodium acetate	4.6	1 M magnesium sulfate
A7	None	0.1 M tri-sodium citrate	5.6	1 M magnesium sulfate
A8	0.1 M lithium sulfate	0.1 M ADA	6.5	1 M magnesium sulfate
A9	None	0.1 M ammonium dihydrogen phosphate	6.5	None
A10	0.1 M ammonium sulfate	0.5 M di-potassium hydrogen phosphate/ 0.5 M di-sodium hydrogen phosphate	7.5	None
A11	0.1M lithium sulfate	0.1 M sodium acetate	4.6	1 M ammonium dihydrogen phosphate
A12	None	0.1 M tri-sodium citrate	5.6	1 M ammonium dihydrogen phosphate
B1	None	0.1 M Tris	8.5	2 M ammonium dihydrogen phosphate
B2	None	None	4.6	2 M sodium formate
B3	None	None	-	4 M sodium formate
B4	None	0.1 M MES	6.5	1.4 M sodium acetate
B5	None	0.1 M Na HEPES	7.5	1.4 M tri-sodium citrate
B6	None	0.1 M Na HEPES	7.5	1 M potassium sodium tartrate
B7	None	0.1 M Na HEPES	7.5	2 % v/v PEG 400/ 2 M ammonium sulfate
B8	0.1M magnesium chloride	0.1 M sodium acetate	4.6	30 % v/v PEG 400
B9	0.1M sodium chloride	0.1 M tri-sodium citrate	5.6	30 % v/v PEG 400
B10	0.1M lithium sulfate	0.1 M tri-sodium citrate	5.6	30 % v/v PEG 400
B11	0.3 M lithium sulfate	0.1 M ADA	6.5	30 % v/v PEG 400
B12	0.1 M magnesium chloride	0.1 M Na HEPES	7.5	30 % v/v PEG 400
C1	0.1 M ammonium sulfate	0.1 M Na HEPES	7.5	30 % v/v PEG 400
C2	0.2 M tri-sodium citrate	0.1 M Tris	8.5	30 % v/v PEG 400
C3	0.1 M zinc acetate	0.1 M sodium acetate	4.6	12 % w/v PEG 4K
C4	0.2 M ammonium sulfate	0.1 M sodium acetate	4.6	12 % w/v PEG 4K
C5	None	0.1 M sodium acetate	4.6	12 % w/v PEG 4K
C6	0.1 M lithium sulfate	0.1 M tri-sodium citrate	5.6	12 % w/v PEG 4K
C7	0.1 M sodium chloride	0.1 M tri-sodium citrate	5.6	12 % w/v PEG 4K
C8	0.1 M lithium sulfate	0.1 M ADA	6.5	12 % w/v PEG 4K
C9	0.1 M sodium chloride	0.1 M Na HEPES	7.5	12 % w/v PEG 4K
C10	0.1 M ammonium sulfate	0.1 M Na HEPES	7.5	12 % w/v PEG 4K
C11	0.2 M magnesium chloride	0.1 M Tris	8.5	12 % w/v PEG 4K
C12	0.2 M lithium sulfate hydrate	0.1 M Tris	8.5	12 % w/v PEG 4K
D1	0.2 M ammonium sulfate	None	-	12 % w/v PEG 4K
D2	0.1 M sodium chloride	0.1 M sodium acetate	4.6	12 % w/v PEG 6K
D3	0.1 M magnesium chloride	0.1 M sodium acetate	4.6	12 % w/v PEG 6K
D4	0.1 M magnesium chloride	0.1 M ADA	6.5	12 % w/v PEG 6K
D5	0.1 M di-ammonium hydrogen phosphate	0.1 M Tris	8.5	12 % w/v PEG 6K
D6	1 M lithium sulfate	None	-	2 % w/v PEG 8K
D7	0.2 M sodium acetate	0.1 M MES	6.5	10 % w/v PEG 8K
D8	0.2 M zinc acetate	0.1 M MES	6.5	10 % w/v PEG 8K
D9	0.2 M calcium acetate	0.1 M MES	6.5	10 % w/v PEG 8K
D10	None	0.1 M Tris	8.5	10 % w/v PEG 8K
D11	0.2 M ammonium sulfate	None	-	10 % w/v PEG 8K
D12	0.5 M lithium sulfate	None	-	10 % w/v PEG 8K



moleculardimensions.com

Targeted Sparse Matrix



MemStart™ & MemSys™ HT-96 Rows E- H MD1-33

Tube #	Salt 1	Salt 2	Buffer	pH	Precipitant
E1	None	None	0.1 M Na citrate	5.5	2.5 M ammonium sulfate
E2	0.1 M sodium chloride	0.1 M lithium sulfate	0.1 M Na citrate	3.5	30 % v/v PEG 400
E3	0.1 M sodium chloride	0.1 M magnesium chloride	0.1 M Na citrate	4.5	30 % v/v PEG 400
E4	0.1 M sodium chloride	None	0.1 M Na citrate	5.5	30 % v/v PEG 400
E5	0.1 M sodium chloride	0.1 M lithium sulfate	0.1 M Na citrate	5.5	30 % v/v PEG 400
E6	0.1 M sodium chloride	0.1 M magnesium chloride	0.1 M Na citrate	5.5	30 % v/v PEG 400
E7	None	None	0.1 M MES	6.5	2.5 M ammonium sulfate
E8	None	None	0.1 M MES	6.5	30 % v/v PEG 400
E9	0.1 M sodium chloride	None	0.1 M MES	6.5	30 % v/v PEG 400
E10	0.1 M sodium chloride	0.1 M lithium sulfate	0.1 M MES	6.5	30 % v/v PEG 400
E11	0.1 M sodium chloride	0.1 M magnesium chloride	0.1 M MES	6.5	30 % v/v PEG 400
E12	None	None	0.1 M MOPS	7.0	30 % v/v PEG 400
F1	None	None	0.1 M Na HEPES	7.5	2.5 M ammonium sulfate
F2	0.1 M sodium chloride	None	0.1 M MOPS	7.0	30 % v/v PEG 400
F3	None	None	0.1 M Na HEPES	7.5	30 % v/v PEG 400
F4	0.1 M sodium chloride	None	0.1 M Na HEPES	7.5	30 % v/v PEG 400
F5	0.1 M sodium chloride	0.1 M lithium sulfate	0.1 M Na HEPES	7.5	30 % v/v PEG 400
F6	0.1 M sodium chloride	0.1 M magnesium chloride	0.1 M Na HEPES	7.5	30 % v/v PEG 400
F7	None	None	0.1 M Tris	8.5	1.5 M lithium sulfate
F8	0.1 M sodium chloride	None	0.1 M Tris	8.5	30 % v/v PEG 400
F9	0.1 M sodium chloride	0.1 M lithium sulfate	0.1 M Tris	8.5	30 % v/v PEG 400
F10	0.1 M sodium chloride	0.1 M magnesium chloride	0.1 M Tris	8.5	30 % v/v PEG 400
F11	0.1 M sodium chloride	0.1 M lithium sulfate	0.1 M CAPSO	9.5	30 % v/v PEG 400
F12	0.1 M sodium chloride	0.1 M magnesium chloride	0.1 M CAPSO	9.5	30 % v/v PEG 400
G1	None	None	0.1 M Na citrate	5.5	1.5 M sodium phosphate
G2	0.1 M sodium chloride	0.1 M magnesium chloride	0.1 M Na citrate	3.5	12 % w/v PEG 4K
G3	0.1 M sodium chloride	0.1 M lithium sulfate	0.1 M Na citrate	4.5	12 % w/v PEG 4K
G4	0.1 M sodium chloride	None	0.1 M Na citrate	5.5	12 % w/v PEG 4K
G5	0.1 M sodium chloride	0.1 M lithium sulfate	0.1 M Na citrate	5.5	12 % w/v PEG 4K
G6	0.1 M sodium chloride	0.1 M magnesium chloride	0.1 M Na citrate	5.5	12 % w/v PEG 4K
G7	None	None	0.1 M MES	6.5	1.5 M sodium phosphate
G8	None	None	0.1 M MES	6.5	12 % w/v PEG 4K
G9	0.1 M sodium chloride	None	0.1 M MES	6.5	12 % w/v PEG 4K
G10	0.1 M sodium chloride	0.1 M lithium sulfate	0.1 M MES	6.5	12 % w/v PEG 4K
G11	0.1 M sodium chloride	0.1 M magnesium chloride	0.1 M MES	6.5	12 % w/v PEG 4K
G12	None	None	0.1 M MOPS	7.0	12 % w/v PEG 4K
H1	None	None	0.1 M Na HEPES	7.5	1.5 M potassium phosphate
H2	0.1 M sodium chloride	None	0.1 M MOPS	7.0	12 % w/v PEG 4K
H3	None	None	0.1 M Na HEPES	7.5	12 % w/v PEG 4K
H4	0.1 M sodium chloride	None	0.1 M Na HEPES	7.5	12 % w/v PEG 4K
H5	0.1 M sodium chloride	0.1 M lithium sulfate	0.1 M Na HEPES	7.5	12 % w/v PEG 4K
H6	0.1 M sodium chloride	0.1 M magnesium chloride	0.1 M Na HEPES	7.5	12 % w/v PEG 4K
H7	None	None	0.1 M Tris	8.5	1.5 M potassium phosphate
H8	0.1 M sodium chloride	None	0.1 M Tris	8.5	12 % w/v PEG 4K
H9	0.1 M sodium chloride	0.1 M lithium sulfate	0.1 M Tris	8.5	12 % w/v PEG 4K
H10	0.1 M sodium chloride	0.1 M magnesium chloride	0.1 M Tris	8.5	12 % w/v PEG 4K
H11	0.1 M sodium chloride	0.1 M lithium sulfate	0.1 M CAPSO	9.5	12 % w/v PEG 4K
H12	0.1 M sodium chloride	0.1 M magnesium chloride	0.1 M CAPSO	9.5	12 % w/v PEG 4K

Abbreviations:
ADA; N-(2-Acetamido)iminodiacetic Acid, **CAPSO**; 3-(Cyclohexylamino)-2-hydroxy-1-propanesulfonic Acid Sodium Salt, **Na HEPES**; N-(2-hydroxyethyl)-piperazine-N'-2-ethanesulfonic acid, sodium salt **MES**; 2-(N-morpholino) ethanesulfonic acid, **MME**; Monomethylether, **MOPS;** 3-(N-Morpholino)-propanesulfonic acid, **PEG**; Polyethylene glycol (4K corresponds to the molecular weight, in thousands of Daltons, of PEG,) **Tris**; 2-Amino-2-(hydroxymethyl) propane-1,3-diol.

Note: The pH of each final reagent is checked and adjusted back to the stated pH of the buffer (±0.2 pH units) as appropriate.

Manufacturer's datasheets are available on request

Appendix2

$ASBT_{NM}$ DNA sequence; 948 bps

ATGAATATCCTCAGTAAAATCAGCAGCTTTATCGGAAAAACATTTTCCCTC

TGGGCCGCGCTCTTTGCCGCCGCCGCTTTTTTCGCGCCCGACACCTTCAAA

TGGGCGGGGCCTTATATTCCTTGGCTGTTGGGCATTATTATGTTCGGTATG

GGTTTGACGCTCAAACCTTCCGACTTCGATATTTTGTTCAAACATCCCAAA

GTCGTCATCATCGGCGTAATCGCACAATTCGCCATTATGCCGGCAACCGC

CTGGCTGCTGTCCAAACTGTTGAACCTGCCTGCCGAAATCGCGGTCGGCG

TGATTTTGGTCGGCTGCTGCCCGGGCGGTACGGCTTCCAATGTGATGACCT

ATCTGGCGCGTGGCAATGTGGCTTTGTCGGTTGCCGTTACGTCTGTTTCCA

CCCTGATTTCCCCATTGCTGACTCCCGCCATCTTCCTGATGCTTGCCGGCG

AAATGCTGGAAATCCAAGCGGCCGGTATGTTGATGTCCATCGTCAAAATG

GTTTTGCTCCCCATTGTTTTGGGTTTGATTGTCCATAAGGTTTTGGGCAGTA

AAACCGAAAAGCTGACCGATGCGCTGCCGCTGGTTTCCGTTGCCGCCATC

GTGCTGATTATCGGCGCGGTTGTTGGGGCAAGCAAAGGCAAGATTATGGA

AAGCGGCCTGCTGATTTTTGCGGTTGTCGTACTCCACAACGGCATCGGCTA

CCTGCTCGGCTTCTTTGCCGCCAAATGGACCGGCCTGCCTTATGATGCACA

AAAAACGCTGACCATCGAAGTCGGTATGCAAAACTCGGGCCTGGCCGCCG

CGCTTGCCGCCGCACACTTTGCCGCCGCGCCGGTCGTTGCCGTTCCGGGCG

CATTGTTCAGCGTGTGGCACAATATCTCCGGCTCGCTGCTGGCAACTTATT

GGGCGGCCAAAGCCGGTAAACATAAAAAACCCTAA